To my love Maria

Acknowledgements

I would like to acknowledge all those very helpful people who have assisted me in my work. These three years have been very important in my life and I will remember it always with great pleasure.

First of all I have to thank my love Maria that in these years has always helped and stand me, giving me the strength to achieve this important goal.

A special thank I have to say to my parents, my sister Rosa and my Grandmother Maria that have been very close to me: thanks a lot for your help and support during these years... thanks mum... thanks daddy.

I want to thank my uncles Pierino and Dina for your support during all my accademic experience.

Then, I have to thank my prof. and university tutor Marano who in these years has been able to follow me and give me the right advice in more than one moment.

I want to thank my friend Floriano who allowed me to make this PhD experience: thank you for this beautiful experience... thanks a lot for having constantly helped me and given many advise to me in these years.

I have to thank my "Master" Peppino, a real brother and a "big" friend: thanks for your help and your support during this great experience.

I want also to thank my friend Mauro... a real friend with which I have shared so many beautiful moments.

I would like to thank my friend Franco who has left us for working in Roma. Then, I have to greet all the other friends of the telecommunication laboratory... the "legendary" AntoFraGe, a real friend, Apollonia, Andrea,

with which I have shared the "enormous" spaces of our office, and all the guys of the laboratory.

I would like to thank my Grandfathers Luigi and Fiore, my Grandmother Rosa and my Great-aunt Teresa that have supported me during the bad periods from up there!

Finally, I would like to thank God for having made possible all this!

Fiore

Summary

In the last few years, Ultra-Wideband communication systems have been extensively studied in both the computer and communication communities. UWB technology is at present defined by the Federal Communications Commission (FCC) as any wireless transmission scheme that occupies a fractional bandwidth $\geq 20\%$, or more than 500 MHz of absolute bandwidth. The potential strength of the UWB-radio technique lies in its use satisfying desirable capabilities including: accurate position location and ranging, and lack of significant multi-path fading owing to fine delay resolution; multiple access owing to wide transmission bandwidths; communications becoming confused with background noise owing to low transmission power operation; possible easier material penetration owing to the low frequency components.

In this Phd Thesis, the UWB physical layer was intensively analyzed both in static scenario and dynamic scenario that is in presence of mobility user. A performance evaluation analysis was carried out in terms of BER and FER for different scenarios, data rates and noise power thresholds and some operative ranges were given. Moreover we performed a three variable polynomial regression analysis in order to obtained a closed formula for the average BER: a distance, noise and rate depending function was obtained. A mathematical treatment about an ideal MMSE receiver follows the regression analysis completing the second Chapter.

In this Phd work an approach to obtain an accurate high level channel model based on Discrete Time Markov Chain modeling, useful in every simulation context, was also provided. In particular, this model is based on the concept of error trace analysis and on the degradation level of given observation windows: the single packet is not analyzed, but an observation window is fixed and the degradation level of the link computing the Packet Error Rate (PER) relative to the specific window is evaluated. This new approach is more accurate than the classic Gilbert-Elliot model, the 3rd order Markov model and the Markov-based Trace Analysis (MTA) Model as a comparative analysis, based on the occurrence of correctly and wrong received packets, showed.

Finally, a new routing protocoll for the UWB network was proposed. The traditional approaches for Ad-hoc network are not valid for UWB systems because they do not take into account of interference between nodes, that is not a trivial problem in these networks. In this case, our main goal is to provide a new routing protocol, called Interference Aware-based Ad-hoc on Demand Distance Vector (IA-AODV), based on the concept of interference: the optimum route is chosen on the basis of the minimum perceived interference. Two distinct metrics are proposed: the first one based on the global interference perceived by a node (NI) and the other one based on the link interference (LI). To test the proposed protocol a ns-2 based simulator was used. The two proposed metrics were compared with the AODV protocol in terms of packet delivery ratio, end-to-end delay and normalized overhead.

Contents

Acknowledgements iii

Summary v

List of Figures xiii

List of Tables xv

Acronyms xvii

1 Ultra Wide Band (UWB) - Communication System 1
- 1.1 UWB History 1
- 1.2 UWB System 3
- 1.3 Advantages and disadvantages of UWB System 6
- 1.4 Comparison between UWB System and other wireless networks 6
- 1.5 Possible Application Fields 7
- 1.6 Typical Pulses employed in UWB System 8
- 1.7 DS-UWB Physical Layer 15
  - 1.7.1 Frame Structure 18
  - 1.7.2 Scrambler 19
  - 1.7.3 Convolutional Code 20
  - 1.7.4 Puncturing Operation 22
  - 1.7.5 Convolutional Interleaver 23
- 1.8 Multi-Band Orthogonal Frequency Division Multiplexing (MB-OFDM) Physical Layer 24
  - 1.8.1 Frame Structre 27
  - 1.8.2 OFDM Modulation 28
- 1.9 TH-PPM Physical Layer 31
- 1.10 Conclusions on Chapter 1 35

2 UWB Physical Layer Analysis 37
2.1 State of Art 38
2.2 UWB Channel Model 39
2.3 DS-UWB architecture 41
2.4 Performance Evaluation 42
2.4.1 BER Simulation Results 43
2.4.2 FER Simulation Results 44
2.5 Regression Analysis 48
2.5.1 BER Regression Analysis 50
2.6 Ideal MMSE Receiver Analysis 55
2.7 Dynamic Scenario: Mobility User 58
2.8 Conclusions on Chapter 2 60

3 A Markovian Approach to Model UWB Channel 65
3.1 State of Art 66
3.2 Degradation Level Based DTMC Channel Modeling 67
3.2.1 DTMC useful definitions 67
3.2.2 DL-DTMC model description 71
3.3 A Case Study: the UWB Channel Modeling 75
3.3.1 Examples of DL-DTMC modeling for UWB system 75
3.3.2 Artificial Trace Generation Algorithm 86
3.3.3 Trace Comparative Analysis 87
3.4 Conclusions on Chapter 3 99

4 IA-AODV routing protocol for UWB Networks 101
4.1 State of Art 102
4.2 Reference Scenario 103
4.3 IA-AODV Protocol 105
4.3.1 Analytical Formulation 105
4.3.2 Refresh Procedure 109
4.3.3 Route Discovery and Maintenance 111
4.4 Performance Evaluation 113
4.4.1 Analysis of α threshold 113
4.4.2 Simulation Results Analysis 114
4.5 Conclusions on Chapter 4 119

Conclusions 121

References 123

List of Publications 129

List of Figures

1.1 Fractional band comparison. 4
1.2 Bandwidth comparison. 4
1.3 FCC e ETSI spectral mask for indoor UWB system. 5
1.4 FCC e ETSI spectral mask for outdoor UWB system. 5
1.5 Comparison between UWB and 802.11b. 7
1.6 Spatial Capaciy Comparison. 7
1.7 Possible Application. 9
1.8 Rectangular Pulse in the Time Domain. 10
1.9 Rectangular Pulse in the Frequency Domain. 10
1.10 Gaussian Monocycle in the Time Domain. 11
1.11 Spectrum of a Gaussian Monocycle. 12
1.12 Doublet Monocycle in the Time Domain. 12
1.13 Spectrum of a Doublet Monocycle. 13
1.14 Rayleigh Monocycle in the Time Domain. 14
1.15 Spectrum of a Rayleigh Monocycle. 14
1.16 Low Band and High Band. 15
1.17 Chip Rate and Center Frequency for each piconet. 16
1.18 DS-UWB WPAN Scheme. 16
1.19 Typical Chip Duration. 17
1.20 Symbol composed by 12 UWB pulses. 17
1.21 Example of Data Rate computing. 17
1.22 Available Data Rates. 18
1.23 Frame Structure. 19
1.24 Scrambler Structure. 20
1.25 Convolutiona Encoder Structure with k=3, n=2, b=1. 21
1.26 Tree Diagram of a Convolutiona Encoder with k=3, n=2, b=1. . 21
1.27 Trellis Diagram of a Convolutiona Encoder with k=3, n=2, b=1. 22
1.28 State Automa of a Convolutiona Encoder with k=3, n=2, b=1. 22
1.29 Puncturing example. 23
1.30 Interleaving Scheme. 23
1.31 Structure of a Convolutional Interleaver. 24

1.32 Carrier Frequency for the Band Group. 25
1.33 OFDM Carrier Frequency. 25
1.34 Available OFDM Data Rate. 26
1.35 Available OFDM Data Rate. 27
1.36 Standard Preamble Structure. 28
1.37 Streaming-mode Preamble Structure. 28
1.38 QPSK Costellation. 29
1.39 TH-PPM Transmission Structure. 32
1.40 Rake Receiver Structure. 32
1.41 TH-PPM Receiver Structure. 33

2.1 a). Impulse response realization for CM1 scenario and for a distance between Tx-Rx of 5 meters. b) Average power decay profile for the same realization. 40
2.2 a). Impulse response realization for CM1 scenario and for a distance between Tx-Rx of 5 meters. b) Average power decay profile for the same realization. 41
2.3 Transmitter and receiver structure. 42
2.4 BER vs. distance Tx-Rx for CM1 scenario, noise power of -55dB. 43
2.5 BER vs. distance Tx-Rx for CM2 scenario, noise power of -55dB. 44
2.6 BER vs. distance Tx-Rx for CM1 scenario, noise power of -35dB. 45
2.7 BER vs. distance Tx-Rx for CM2 scenario, noise power of -35dB. 45
2.8 FER vs. distance for CM1 scenario with a frame size of 128 bytes. 46
2.9 FER vs. distance for CM1 scenario with a frame size of 1024 bytes. 47
2.10 FER vs. distance for CM2 scenario with a frame size of 128 bytes. 47
2.11 FER vs. distance for CM2 scenario with a frame size of 1024 bytes. 48
2.12 a) BER vs. distance and noise PSD for rate 28 Mbps, CM1 scenario. b) Relative error committed by regression analysis. . . . 52
2.13 a) BER vs. distance and noise PSD for rate 500 Mbps, CM1 scenario. b) Relative error committed by regression analysis. . . . 52
2.14 a) BER vs. distance and noise PSD for rate 55 Mbps, CM2 scenario. b) Relative error committed by regression analysis. . . . 54
2.15 a) BER vs. distance and noise PSD for rate 220 Mbps, CM2 scenario. b) Relative error committed by regression analysis. . . . 54
2.16 Chebyshev passband filter impulse response. 56
2.17 BER analytic and simulated vs. distance for CME scenario, rate 110 Mbps, PSD noise of -35 dB. 58
2.18 User moving pattern. 59
2.19 Average BER vs. maximum users speed for CM1 scenario, average SNR -30 dB 61

2.20 Average BER vs. maximum users speed for CM2 scenario, average SNR -30 dB 61

3.1 Number of states vs. Entropy order. 68
3.2 State transition probabilities vs. noise power level. 71
3.3 Relation between degradation level and state number. 72
3.4 Mean square values computed for each time interval for 28 Mbps data rate in CM4 scenario with a mean power noise of -30 dB. 76
3.5 Occurrences of correct packets in original trace and in the artificial traces for data rate 28 Mbps in CM4 scenario, mean power noise of -30 dB. 78
3.6 "0" state sojourn time distributions and its approximation exponential distribution for 28 Mbps data rate in CM4 scenario, mean noise power of -30 dB. 78
3.7 Conditional entropy vs. order of entropy for our approach and traditional approach for the rate 28 Mbps in the CM4 scenario, mean noise power of -30 dB. 79
3.8 Mean square values computed for each time interval for 55 Mbps data rate in CM1 scenario with a mean power noise of -30 dB. 79
3.9 "0" state sojourn time distributions and its approximation exponential distribution for 55 Mbps data rate in CM1 scenario, mean noise power of -30 dB. 80
3.10 Mean square values computed for each time interval for 110 Mbps data rate in CM2 scenario with a mean power noise of -45 dB. 81
3.11 "0" state sojourn time distributions and its approximation exponential distribution for 110 Mbps data rate in CM2 scenario, mean noise power of -45 dB. 82
3.12 Mean square values computed for each time interval for 220 Mbps data rate in CM4 scenario with a mean power noise of -35 dB. 82
3.13 "2" state sojourn time distributions and its approximation exponential distribution for 220 Mbps data rate in CM4 scenario, mean noise power of -35 dB. 83
3.14 "5" state sojourn time distributions and its approximation exponential distribution for 500 Mbps data rate in CM2 scenario, mean noise power of -50 dB. 84
3.15 "3" state sojourn time distributions and its approximation exponential distribution for 660 Mbps data rate in CM3 scenario, mean noise power of -45 dB. 85
3.16 "2" state sojourn time distributions and its approximation exponential distribution for 1000 Mbps data rate in CM2 scenario, mean noise power of -60 dB. 86

3.17 Correct packets distribution for artificial and experimental traces, first configuration. 87
3.18 Wrong packets distribution for artificial and experimental traces, first configuration. 88
3.19 Correct packets distribution for artificial and experimental traces, second configuration. 89
3.20 Wrong packets distribution for artificial and experimental traces, second configuration. 89
3.21 Correct packets distribution for artificial and experimental traces, third configuration. 90
3.22 Wrong packets distribution for artificial and experimental traces, third configuration. 91
3.23 Correct packets distribution for artificial and experimental traces, the fourth configuration. 92
3.24 Wrong packets distribution for artificial and experimental traces, the fourth configuration. 92
3.25 Correct packets distribution for artificial and experimental traces, the fifth configuration. 93
3.26 Wrong packets distribution for artificial and experimental traces, fifth configuration. 94
3.27 Correct packets distribution for artificial and experimental traces, sixth configuration. 95
3.28 Wrong packets distribution for artificial and experimental traces, sixth configuration. 95
3.29 Correct packets distribution for artificial and experimental traces, seventh configuration. 96
3.30 Wrong packets distribution for artificial and experimental traces, seventh configuration. 97
3.31 Correct packets distribution for artificial and experimental traces, eighth configuration. 97
3.32 Wrong packets distribution for artificial and experimental traces, eighth configuration. 98

4.1 a) RREQ packet structure. b) RREP packet structure. c) Routing table entry. 106
4.2 Interference Control on a generic link for the LI metric. 110
4.3 Procedures performed by a node at the reception of a RREP packet. 112
4.4 a) PDR vs. α, 4 maximum concurrent connections, 120 nodes. b) PDR vs. α, 8 maximum concurrent connections, 140 nodes. . 115
4.5 PDR vs. number node in presence of 12 maximum concurrent connections. 116
4.6 AED vs. number node in presence of 12 maximum concurrent connections 117

4.7 NRO vs. number node in presence of 12 maximum concurrent connections. 117
4.8 PDR vs. concurrent connection maximum number with 120 nodes. 118
4.9 AED vs. concurrent connection maximum number with 120 nodes. 119
4.10 NRO vs. concurrent connection maximum number with 120 nodes. 119

List of Tables

2.1 Channel Characteristics 39
2.2 Operative Range for DS-UWB (in meters) 48
2.3 Average applications operative range in m/s. 62

3.1 Error Trace Statistics for first configuration. 88
3.2 Error Trace Statistics for second configuration. 88
3.3 Error Trace Statistics for the third configuration. 91
3.4 Error Trace Statistics for fourth configuration. 93
3.5 Error Trace Statistics for fifth configuration. 94
3.6 Error Trace Statistics for sixth configuration. 94
3.7 Error Trace Statistics for seventh configuration. 96
3.8 Error Trace Statistics for eighth configuration. 98
3.9 Standard Errors for all configurations. 99

4.1 Simulation Parameters. 114

Acronyms

4BOK Quaternary Bi-Orthogonal Keying
AED Average End-To-End Delay
AODV Ad-hoc On Demand Distance Vector
ARP Automatic Retransmission Request
AWGN Average White Gaussian Noise
BAN Body Area Network
BER Bit Error Rate
BPSK Binary Phase Shift Keying
CDMA Code Division Multiple Access
DC Direct Component
DCC-MAC Dynamic Channel Coding - MAC
DFE Decision-Feedback Equalization
DL-DTMC Degradation Level - DTMC
DPDR Data Packet Delivery Ratio
DS Direct Sequence
DSR Dynamic Source Routing
DS-SS Direct Sequene - Spread Spectrum
DTMC Discrete-Time Markov Chain
ETSI European Telecommunications Standards Institute
FCC Federal Communications Commission
FCS Function of CheckSum
FDTD Finite-Difference Time-Domain
FEC Forward Error Correction
FER Frame Error Rate
G-E Gilbert-Elliot
GPS Global Positioning System
HCS Header Check Sequence
hMM Hierarchical Markov Model
IA-AODV Interference Aware-based Ad-hoc On Demand Distance Vector
IEEE Institute of Electrical and Electronic Engineers
ISI Inter-Symbol Interference

ITU International Telecommunications Union
LE Linear Equalization
LI Link Interference
LOS Line of Sight
LPI/D Low Probability of Interception and Detection
MAC Medium Access Control
MB-OFDM Multi-Band Orthogonal Frequency Division Multiplexing
MMSE Minimum Mean Square Error
MTA Markov-based Trace Analysis
NAVC Network Allocator Vector Count
NI Node Interference
NLMS Normalised Least Minimum Square
NLOS No-Line of Sight
NRO Normalized Routing Overhead
ns-2 Network Simulator 2
PAC Piconet Access Codes
PAN Personal Area Network
PDA Personal Digital Assistant
PER Packet Error Rate
PHY Physical
PLCP Physical Layer Convergence Procedure
PN Pseudo Noise
PNC piconet controller
PRG Pseudo-Random Generator
PSD Power Spectrum Density
QPSK Quadrature Phase Shift Keying
RREP Route REPly
RREQ Route REQuest
SF Spreading Factor
SNR Signal to Noise Ratio
TFC Time-Frequency Code
TH-PPM Time Hopping-Pulse Position Modulation
THS Time Hopping Sequences
UWB Ultra Wide Band
WPAN Wireless Personal Area Network

1

Ultra Wide Band (UWB) - Communication System

Since the US Federal Communications Commission (FCC) approved the limited use of UWB technology, communications systems that employ UWB signals have drawn considerable attention.

Ultra-wideband radio communicates with baseband signal pulses of very short duration (typically the duration is few nanoseconds). The "shape of the signal" has a frequency characteristic starting from near very low frequency (few Hz) to Gigahertz range; in particular an UWB system is defined by FCC as a communication system occupying a fractional bandwidth larger than 20% of center frequency or an absolute bandwidth larger than 500 MHz [1]. Moreover, UWB signals have very low power spectral densities values (typically few microW per MHz) and their energy is spreaded on a very large band, so they can coexist with incumbent systems in the same frequency range. These characteristics and the possibility of achieving sufficiently higher data rates without the need to increase transmitter power make UWB technology a viable candidate for short (lesser than 20 meters) and medium (lesser than 100 meters) range multiple access communications in dense multipath indoor and outdoor environments.

1.1 UWB History

The origins of the UWB technology goes back to 1962, when, to describe the characteristics of some Microwave networks in the in the time domain, it began to study also their impulse response [2],[3].

From 1962 onwards, thanks also to the progress of technology and in particular with the advent of sampler oscilloscope, there were many studies on the impulse response invariant time linear system: Harmuth at the Catholic University of America, Ross e Robbins at the Sperry Rand Corporation, Van Etten at the USAF's Rome Air Develepment Center and in Russia.

Between 1968 and 1984 Harmuth divulged the base schemes of the UWB transmitters and receivers. In 1972, Robbins made a receiver for short im-

pulses, while in 1973 Ross obtained the first patent related to UWB communications and following years the two scientists used this technology in several fields: from telecommunications to radar. In 1974 Morey planned a radar system based on UWB technology called "Geophisycal Survey System", which had a considerable success.

Between the 1960s and 1970s the development of this technology remained always related to progress of the great manufacturers of diagnostic tools in the time domain such as the Hewlett Packard and the Tektronix. Only from the 1970s, the development of UWB had not more technological obstacles thanks also to innovative components placed on the market by Tektronix.

In the meantime, the Russians also developed this technology independently of the Americans. In 1951 Zernov observed the differences between the methods of analysis based on continuous wave signals and methods based on Ultra Short impulses. In 1952, Kharcevitch showed as the methods of analysis in the the time domain involving Ultra Short impulses were simpler to develop than traditional methods employing continuous waves.

In 1957, Astanin developed a transmitter in X band of impulses from duration of 0.5 ns in order to study the waveguides, while in 1964, at the USSR Academy of Sciences, Kobzarev led tests on the propagation of UWB indoor impulses generated by high resolution radars. In contrast to the Americans, the attention of the Russians was initially focused on radar, and only afterwards their researches spread in other fields until obtaining the same results.

From 1980s, both in Russia and the United States, the basic concepts of this technology were now known, and the UWB began to be implemented in new areas such as the positioning and medical field but above all in the military field. In 1988 Taylor and Ross, together with Fountain designed and created a system of communication at a Low Probability of Interception and Detection (LPI/D) for the United States Government.

It is precisely in the military area of those years that was coined the term "Ultra Wide Band", before then, in fact, this technology had many names: baseband, impulse, carrier-free, non-sinusoidal, time-domain.

The first academic programs and the first scientific publications on the various aspects of this technology: modulations, spectrum, iterations with the human body, type of impetus, antennas, etc., were carried out in those years. Up to a few years ago, however, the UWB technology was not a great application in the commercial field, despite its simplicity circuit and the enormous potential that it seems to have.

Only in 2002, the FCC, has assigned a new license-free band (3.1-10.6 GHz) in which, even if with severe power limitations, the UWB can work. In Europe and Japan in 2003, European Telecommunications Standards Institute (ETSI) and other similar organizations have proposed the use of the UWB following essentially the US legislation.

Due to these technical advantages and to the recent commercial interests, Institute of Electrical and Electronic Engineers (IEEE) found two task groups, 802.15.3a [4] and 802.15.4a [5], in order to standardize a physical layer respec-

tively for High Rate and Low Rate UWB communications systems. IEEE 802.15.3a was an attempt to provide a higher speed UWB Physical (PHY) enhancement amendment to IEEE 802.15.3 for applications which involve imaging and multimedia.

The most important goal of IEEE 802.15.3a was the consolidation of 23 UWB PHY specifications into two proposals: Multi-Band Orthogonal Frequency Division Multiplexing (MB-OFDM) UWB [6], supported by the WiMedia Alliance [7], and Direct Sequence (DS)-UWB [8], supported by the UWB Forum [9]. Actually, the two different parts supporting standard proposals have not reached an accord, so the standardization process is in deadlock and both standards are going out on the market place. The presence on the market of UWB products with different standards and especially not interoperable will inevitably lead to higher prices. Another UWB High Rate physical layer initially proposed also to IEEE 802.15.3a task group is the Time Hopping-Pulse Position Modulation (TH-PPM). this proposal had not commercial appeal, however it is highly considered in the accademic field.

Instead, IEEE 802.15.4a provides a Wireless Personal Area Network (WPAN) Low Rate Alternative PHY. Actually two optional PHYs are considered: UWB Impulse Radio (operating in unlicensed UWB spectrum) and a Chirp Spread Spectrum (operating in unlicensed 2.4GHz spectrum) level. In this case the IEEE task group work successfully led to a standard publication with both physical layer supported [10].

1.2 UWB System

An UWB communication system can be defined as a communication system with a very large fractional bandwidth [11]. The fractional bandwidth is defined as the ratio of band B occupied by the signal and the center frequency fc of the same signal [12]:

$$BW = \frac{B}{f_c} = 2 \cdot \frac{f_H - f_L}{f_H - f_L} \tag{1.1}$$

where fH is the upper frequency of the 10 dB emission point and fL is the lower frequency of the 10 dB emission point. The center frequency of the transmitted signal is therefore defined as:

$$f_c = \frac{(f_H + f_L)}{2} \tag{1.2}$$

whereas the bandwidth is given by:

$$B = (f_H - f_L) \tag{1.3}$$

More precisely, an UWB system is defined by FCC as a communications system occupying a fractional bandwidth larger than 20% of center frequency or an absolute bandwidth larger than 500 MHz [1].

Comparing UWB fractional band with fractional band of the other systems, it can be seen, in Figure 1.1, as the traditional *narrowband* communication systems typically employ signals having a fractional band lesser than 1%; whereas, comparing the bandwidth (see Figure 1.2) it can be noted that the UWB systems occupy a band considerably greater than narrowband systems (B=30KHz) and classic Spread Spectrum system such as 802.11b networks (B=80MHz).

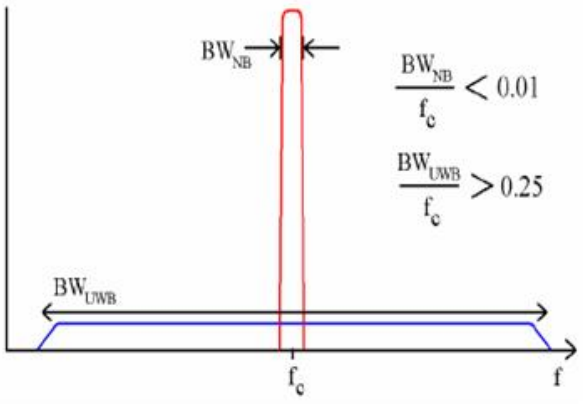

Fig. 1.1. Fractional band comparison.

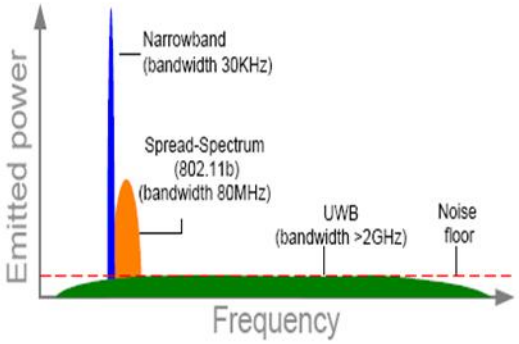

Fig. 1.2. Bandwidth comparison.

In the UWB systems, a so high bandwidth is obtained through the transmission of baseband Gaussian impulses and their derivative and second derivative of few nanoseconds duration, properly filtered to respect power emission and band limitation normative. In the USA, the FCC established that UWB

systems must transmitter in the 3.1-10.6 GHz licence-free band as regulated by "*Code of Federal Regulations*", *Title* 47, *Section* 15 [13]. The same law limits the Power Spectrum Density (PSD): The maximum power spectral density of the UWB is -41.3 dBm/MHz, which is extremely low. This results in small interference with other radio signals while maintaining excellent immunity to interference from these signals. Further limitations have been added under 2 GHz in order to avoid interference on critic applications such as Global Positioning System (GPS).

Other countries, such as those complied at the International Telecommunications Union (ITU) directives, allowed free-licence frequency following the FCC normatives: e.g. in Europe, the ETSI has standardized the UWB communication system in the same frequency range of the USA [14],[15]. In Figure 1.3 and Figure 1.4 are shown the FCC and ETSI mask respectevely for indoor and outdoor UWB system.

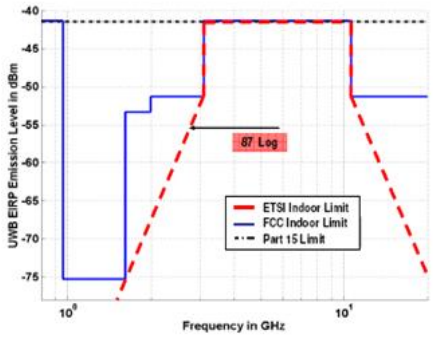

Fig. 1.3. FCC e ETSI spectral mask for indoor UWB system.

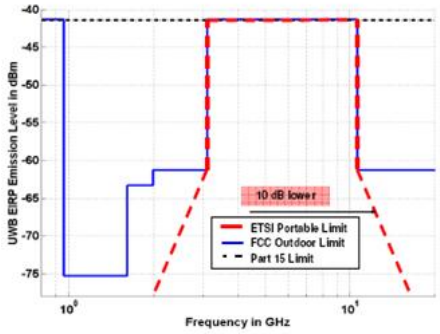

Fig. 1.4. FCC e ETSI spectral mask for outdoor UWB system.

1.3 Advantages and disadvantages of UWB System

UWB technology has considerable benefits due to its ultra band nature. Among these benefits, we must doubtless remember:

- capability to reach high data rates (up to 1.3 Gbps);
- lesser loss on paths and greater robustness against multipath fading. Given that the UWB signals occupy a wide spectrum of frequencies (from the lowest until the highest ones), they have a power loss sufficiently low when penetrate the material, this also means a fading very selective in frequency and a large number of multipath components resolvable;
- Availability of low-cost devices. The receiver structure can be, in fact, very simple thanks the absence of carrier frequency, and the techniques to generate impulses are mature because they are studied from more than 30 years;
- low-power transmission and low levels of interference. For short range operations, the average transmission power of nanosecond order impulses is very low. These features allow UWB systems to coexist with other narrowband radio systems, occupying the same band, without cause high interference. The UWB work in practice with emission levels comparable with the most common digital devices such as laptop computers and Personal Digital Assistant (PDA).

However, there are also many disadvantages related to this technology. These include the distortion, because of propagation delays of received waveform that makes difficult to explore different paths of received signal and the complexity of synchronization of very short pulses at the receiver side. UWB systems are, moreover, very sensible to interference due to multi access and this leads to a rapid decay of the overlapping of benefits with increasing the signals. add to that which, to increase the capacity of the channel and throughput and it is necessary to use modulation diagrams of high order.

1.4 Comparison between UWB System and other wireless networks

Its electromagnetic characteristics make UWB unique. The considerable structural differences and a physical level different lead to behavior and performance very different than traditional wireless systems.

In Figure 1.5 are summarized the main characteristics of the networks based on UWB and 802.11b standard. As already mentioned, the two standards have various differences: the carrier frequency in the occupied band, but especially both the operative range and the maximum data rates change considerably. In Figure 1.6, are compared the UWB systems and the conventional wireless systems in terms of space capacity, measured as the maximum

aggregate data rate of N devices active per unit of area, maximum range of transmission and average location error. For example, the notation "IEEE 802.11b (3x11Mbps)" means that there are three IEEE 802.11b devices communicating simultaneously with three different Access Points, each one with a data rate of 11 Mbps over a distance of 100 m.

Characteristics	UWB (802.15.3a)	802.11b
Fractional Band	> 25%	<1%
Bandwidth	~ 2Ghz	80MHz
Operative Frequency	3.1-10.6GHz	2.4GHz
Network Topology	WPAN	WLAN
Operative Range	~30m (for 28Mbps data rate)	150m indoor (up to 600m in outdoor scenario)
Data rate	Up to 1.3Gbps	Up to 11Mbps
Physical Layer	DS-SS,OFDM,TH-PPM	DS-SS,FH-SS,IR

Fig. 1.5. Comparison between UWB and 802.11b.

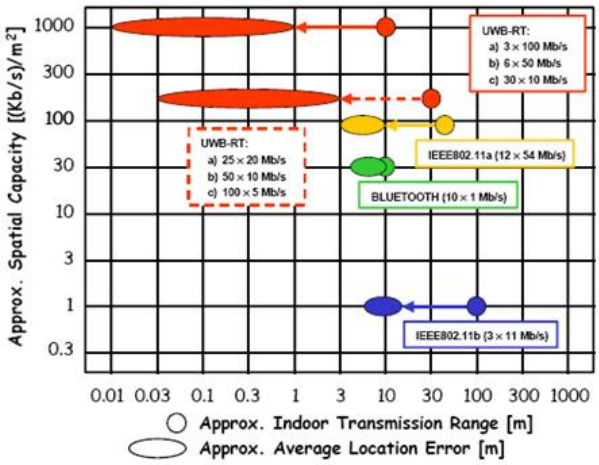

Fig. 1.6. Spatial Capaciy Comparison.

1.5 Possible Application Fields

The UWB systems are able to implement wireless platforms that allow many different mode of working such as data transmission, high precision positioning, radar sensor and various combination of them ([11],[12]). Therefore, a

large scale of new wireless applications are allowed by the UWB technology; in the following, we show some of the most important fields of application. An important class of application is thePersonal Area Network (PAN)s, where the data is transmitted over a distance of around 10 m or lesser. In particular, we must distinguish between high rate applications, such as digital TV and network computer, and low rate applications, including other electronic applications such as audio streaming. The Body Area Network (BAN) are a particular case of PANs, where the communication occurs between two devices that an user has on [16]. Another new use of the UWB is in the sensor networks. In this case, as the required data rate is low (generally 1 Kbps-1 Mbps), the operative range is greater than the WPAN case (around 100-300 m). these applications include the monitoring of residential and work environment, the monitoring of industry environment and the video surveillance of airports or other sensible build.

A bandwidth so large, also offers the possibility of positioning techniques with high precision and therefore of operations of geo-location [17]. For these applications, the first path of the impulse response plays a crucial role in contrast to the traditional models of channel, where, instead, other parameters such as the path loss and the delay spread are more important.

A further field of application is in the context of the communications of emergency, communications between fire stations and between other entities of the security force and within radio-tactical military systems [18]. These types of application range in most of the groups described above and in addition also include communications through the snow (e.g. communications of emergency after an avalanche) and through the rubble (for example the communications with the victims in response to an earthquake or to another natural disaster). Despite the high importance of these rescue missions, actually publications that deal with the modeling of the channel in these particular situations are not still made.

Another potential use is in peer-to-peer and of ad-hoc networks in outdoor environments. In this case, nodes distant are able to communicate by relying the signal on intermediate nodes.

In Figure 1.7, some of the possible scenarios described above are shown: achievements of WPANs in homes or offices, sensor networks for the surveillance or for the control of the safety devices, positioning or control of equipment in industrial environments, peer-to-peer networks in external ambient and achievements of WBANs.

1.6 Typical Pulses employed in UWB System

The UWB transmission schemes are based on baseband wave that can be employed with different techniques of modulation ([19],[20]). The transmitted signal is composed by a train of few nanoseconds duration pulses. Each of these pulses is typically called monocycle. The information is carried both by

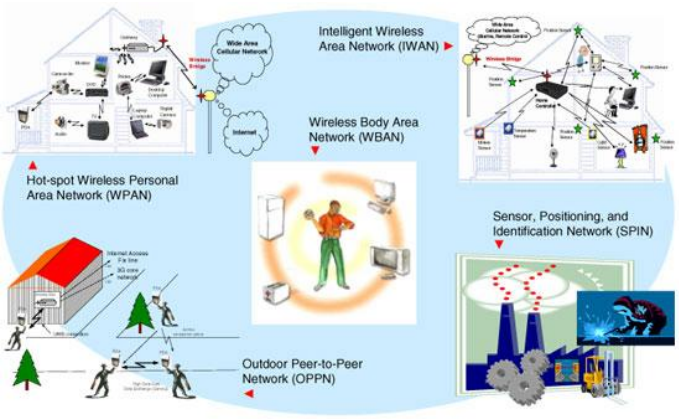

Fig. 1.7. Possible Application.

position and amplitude of the impulse. Typically, electromagnetic radiations from the spectrum very wide in the domain of frequencies correspond to very short pulses in the time domain. Therefore, the baseband pulses can have a spectrum spreads from zero to some GHz. The spectrum of UWB signals depends on specific type of pulses employed.

The typical pulses employed in literature are the Gaussian, Gaussian doublet and Rayleigh monocycles.

A rectangular pulse of amplitude T_P and unitary energy can be represent by:

$$p_R(t) = \sqrt{\frac{1}{T_P}} \left[U(t) - U(t - T_P)\right] \tag{1.4}$$

where with *U(•)* it is denoted the *unitary step*. In Figure 1.8 and Figure 1.9 are, respectively, shown a rectangular pulse of 1 ns duration and its spectrum.

However, the rectangular pulse has a large Direct Component (DC) that is not a desirable characteristic. Despite this problem, the rectangular pulses are frequently employed in the academic research for their simplicity. A generic Gaussian pulse can be expressed as:

$$p_g(t) = \frac{1}{\sqrt{2\pi\sigma}} \exp\left[-\frac{1}{2}\left(\frac{t-\mu}{\sigma}\right)^2\right], \tag{1.5}$$

where μ defined the pulse center, whereas σ determines the amplitude of the pulse. Some of most popular and employed *monocycles* derived from Gaussian pulse.

The Gaussian *monocycle*, for example, is the second derivative of Gaussian pulse and it can be analytically represented as:

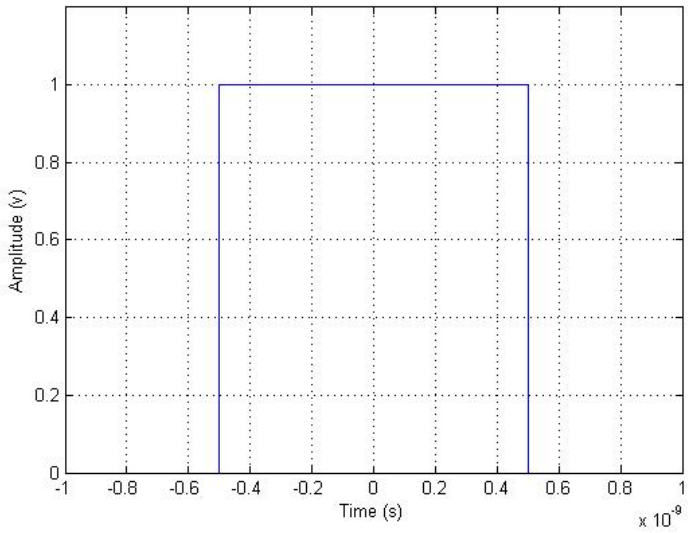

Fig. 1.8. Rectangular Pulse in the Time Domain.

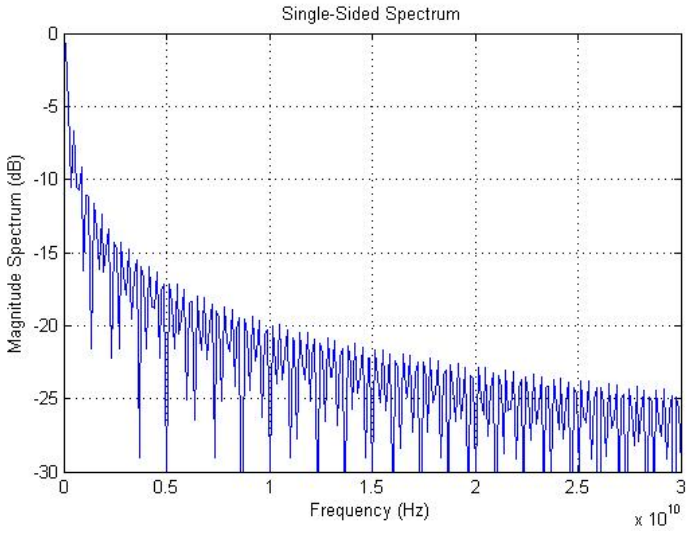

Fig. 1.9. Rectangular Pulse in the Frequency Domain.

$$p_G(t) = A_G \left[1 - \left(\frac{t-\mu}{\sigma}\right)^2\right] \exp\left[-\frac{1}{2}\left(\frac{t-\mu}{\sigma}\right)^2\right], \tag{1.6}$$

where σ parameters determines the amplitude of T_P of the impulse. The effective duration of wave, that contains the 99.99% of the total Energy of the monocycle, is $T_p = 7\sigma$ centered at $\mu = 3.5\sigma$. The factor A_G is introduced in order to normalize the total energy of the *monocycle*.

Instead, the spectrum of Gaussian monocycle is given by:

$$P_G(f) = A_G\sqrt{2\pi}\sigma\left(2\pi\sigma f\right)^2 \exp\left[-\frac{1}{2}\left(2\pi\sigma f\right)^2\right] \times \exp\left(-j2\pi f\mu\right) \tag{1.7}$$

In Figure 1.10 and Figure 1.11 are, respectively, shown a typical Gaussian *monocycle* and its spectrum.

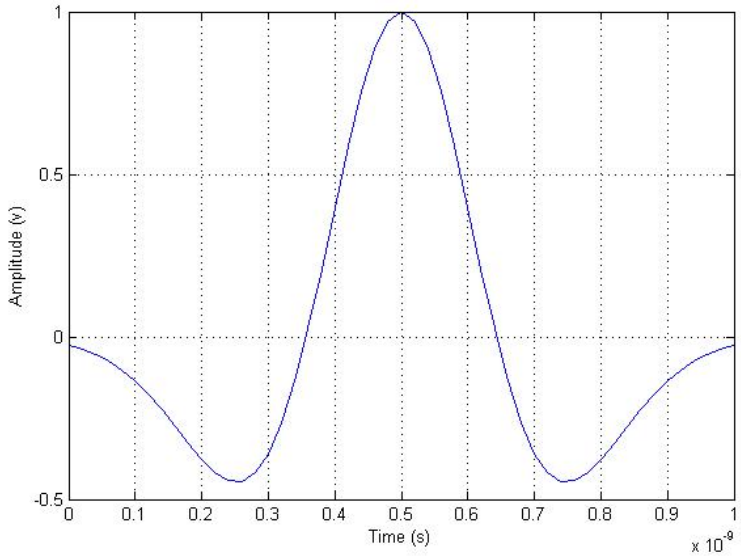

Fig. 1.10. Gaussian Monocycle in the Time Domain.

The *doublet* Gaussian *monocycle* instead, is a bipolar signal composed of two Gaussian pulses by opposed amplitude with a temporal gap of T_w among them.

The mathematical expression for the *monocycle* is:

$$p_{GD}(t) = A_{GD}\left\{\exp\left[-\frac{1}{2}\left(\frac{t-\mu}{\sigma}\right)^2\right] - \exp\left[-\frac{1}{2}\left(\frac{t-\mu-T_w}{\sigma}\right)^2\right]\right\}, \tag{1.8}$$

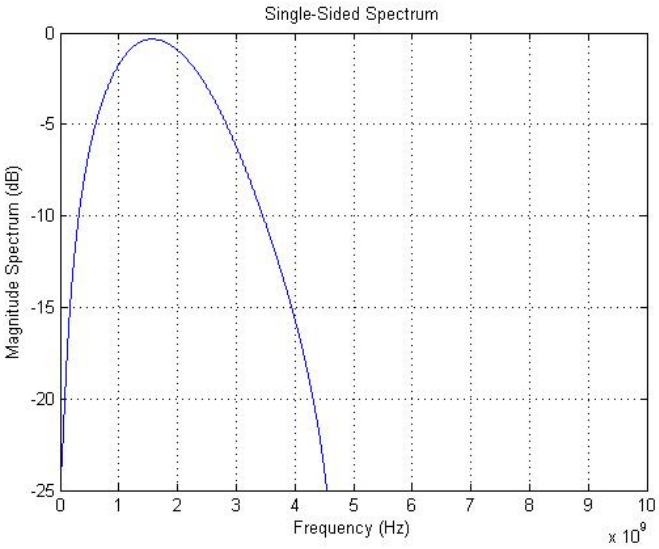

Fig. 1.11. Spectrum of a Gaussian Monocycle.

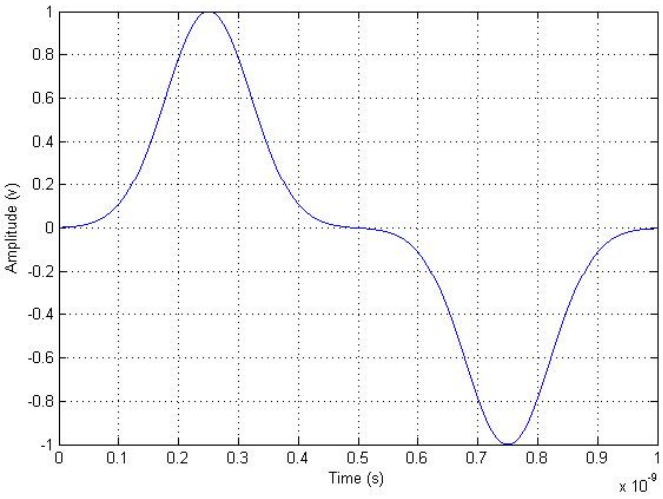

Fig. 1.12. Doublet Monocycle in the Time Domain.

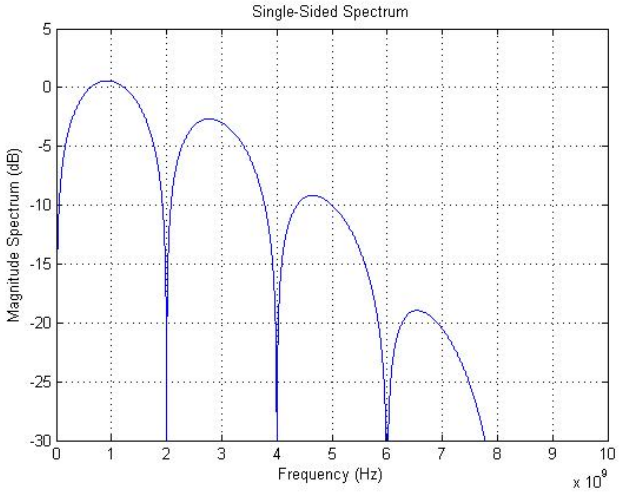

Fig. 1.13. Spectrum of a Doublet Monocycle.

that has a Fourier Transform given by:

$$P_{GD}(f) = 2A_{GD}\sqrt{2\pi}\sigma \sin(\pi f T_w) \exp\left[-\tfrac{1}{2}(2\pi f)^2\right] \times \exp\left\{-j\left[2\pi f\left(\mu + 0.5T_w\right) - 0.5\pi\right]\right\} \ . \tag{1.9}$$

The pulse amplitude is given by the parameters i μ, σ, and T_w. The pulse with an amplitude of T_P=*14*σ and T_w=*7*σ contains the 99.99% of total Energy of the *monocycle*

In Figure 1.12 and Figure 1.13 are shown the *doublet monocycle* in the time and frequency domain. The Rayleigh *monocycle* is originated from first derivative of Gaussian pulse and it can be expressed as:

$$p_R(t) = A_R\left[\frac{t-\mu}{\sigma^2}\right]\exp\left[-\frac{1}{2}\left(\frac{t-\mu}{\sigma}\right)^2\right] \tag{1.10}$$

The Fourier Transform is given by:

$$P_R(f) = A_R\sqrt{2\pi}\,(2\pi\sigma f)\exp\left[-\frac{1}{2}(2\pi\sigma f)^2\right] \times \exp\left[-j\left(2\pi f\mu + 0.5\pi\right)\right]. \tag{1.11}$$

The effective duration of wave, containing the 99.99% of total energy of the *monocycle*, is $T_p = 7\sigma$ centering at $\mu = 3.5\sigma$, that is the same of the previously described Gaussian *monocycle*.

In Figure 1.14 and in Figure 1.15 are, respectively, shown a representation of the Rayleigh *monocycle* both in time domain and frequency domain.

Differently by the rectangular impulse, *monocycles* described above has as an important feature: they not have the DC, this makes their irradiation still more efficient.

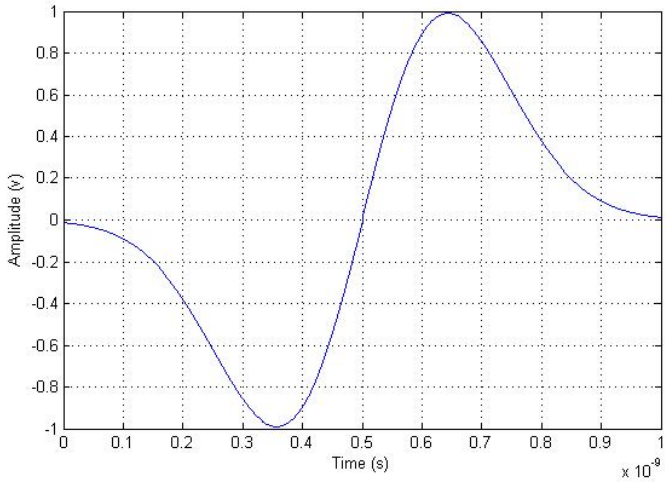

Fig. 1.14. Rayleigh Monocycle in the Time Domain.

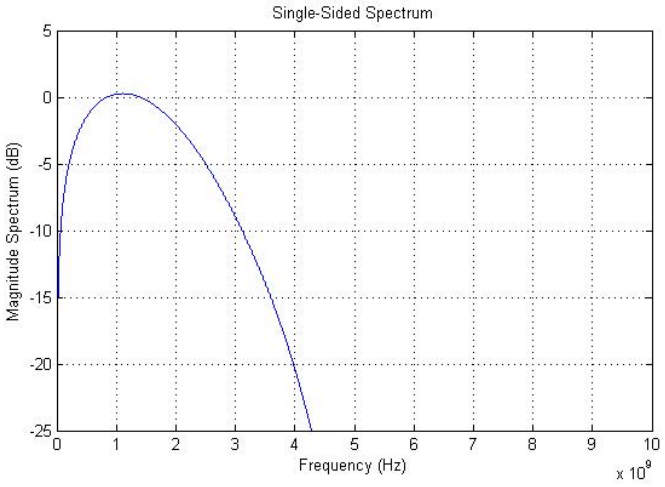

Fig. 1.15. Spectrum of a Rayleigh Monocycle.

1.7 DS-UWB Physical Layer

The DS-UWB tecnique provides a wireless PAN with data payload communication capabilities of 28, 55, 110, 220, 500, 660, 1000 and 1320 Mbps [9].

The Spread Spectrum system due their name to the fact that in this type of system the band is deliberately increased with respect to the minimum necessary. The most used is probably the transmission with Direct Sequene - Spread Spectrum (DS-SS). In this type of transmission, the signal occupies completely the band for the whole transmission time. In this system, to obtain the spread of the spectrum the signal is multiply by a binary or ternary sequence (called spreading sequence), that is unique for each user, allowing in this way a multiple access to the medium: de facto, it implements a Code Division Multiple Access (CDMA).

The proposed UWB system employs direct sequence spreading of Binary Phase Shift Keying (BPSK) or quaternary bi-orthogonal keying (4BOK) UWB pulses. DS-UWB supports two independent bands of operation: the *Low Band* occupying the spectrum from 3.1 GHz to 4.85 GHz and the *High Band* occupying the spectrum from 6.2 GHz to 9.7 GHz (see Figure 1.16).

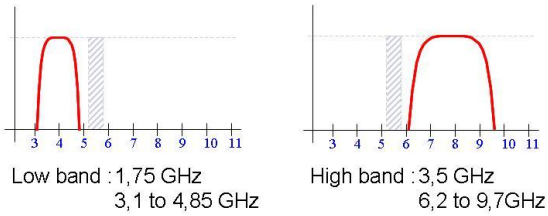

Fig. 1.16. Low Band and High Band.

Each band can support up to six piconet channels to have unique operating frequencies and acquisition codes. A compliant device should implement only support for piconets channels 1-4, which are in the low band. Support for piconets channels 5-12 is optional (see Figure 1.17).

The Piconet Access Codes (PAC)s for acquisition (corresponding to the piconet channel being used). The piconet controller (PNC) selects the operating PAC during piconet establishment [21] (see Figure 1.18). This code is employed by the new node in the PHY preamble together the Chip Rate and the Forward Error Correction (FEC) scheme to calculate the effective bit rate.

Three types of preamble are available:

- Short Preamble, that is 5 μs in length that requires a high SNR with low channel dispersion;
- Nominal Preamble: 15 μs in length that requires a nominal SNR and a nominal channel (it is the default choice);

Piconet Channel	Chip Rate	Center Frequency
1	1313 MHz	3939 MHz
2	1326 MHz	3978 MHz
3	1339 MHz	4017 MHz
4	1352 MHz	4056 MHz
5	1300 MHz	3900 MHz
6	1365 MHz	4094 MHz
7	2626 MHz	7878 MHz
8	2652 MHz	7956 MHz
9	2678 MHz	8034 MHz
10	2704 MHz	8112 MHz
11	2600 MHz	7800 MHz
12	2730 MHz	8190 MHz

Fig. 1.17. Chip Rate and Center Frequency for each piconet.

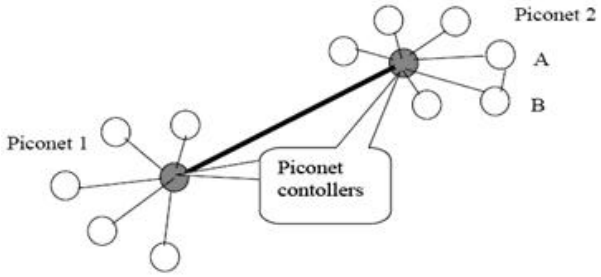

Fig. 1.18. DS-UWB WPAN Scheme.

- Long Preamble: 30 μs in length that is used for a poor SNR and highly dispersive channel.

The chip rate is simply the inverse of a pulse duration and it is related to the piconet channel and to the operative frequency. In Figure 1.19 the relationship between chip rate and frequency is shown. In addition to the acquisition code, the preamble is also used to recover the clock and carrier frequency and for receiving of training sequence. DS-UWB systems also employ error correction technique: in particular convolutional codes with code rate of or are used.

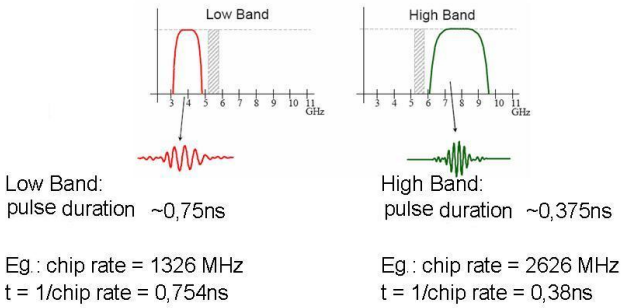

Fig. 1.19. Typical Chip Duration.

Each transmitted symbol is composed by a sequence of UWB pulses as shown in Figure 1.20.

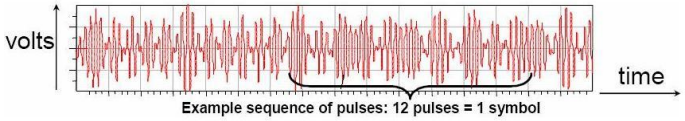

Fig. 1.20. Symbol composed by 12 UWB pulses.

The different data rates are supported through ternary spreading code sequences of length variable from 1 to 24 pulses (chips) [22]. Information about bit number per symbol, preading code length and employed FEC scheme are included in the PHY Header and through these information a device is able to compute the consequent data rate (see example in Figure 1.21).

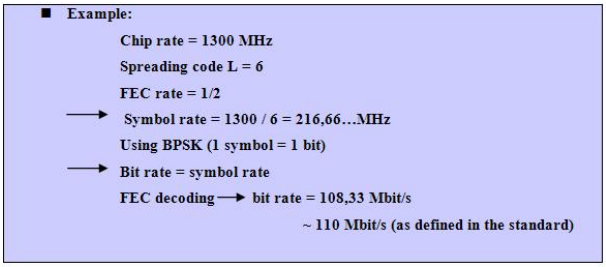

Fig. 1.21. Example of Data Rate computing.

Data Rate	FEC Rate	Code Length	Bits per Symbol	Symbol Rate
28 Mbps	½	L=24	1	$F_{chip}/24$
55 Mbps	½	L=12	1	$F_{chip}/12$
110 Mbps	½	L=6	1	$F_{chip}/6$
220 Mbps	½	L=3	1	$F_{chip}/3$
500 Mbps	¾	L=2	1	$F_{chip}/2$
660 Mbps	1	L=2	1	$F_{chip}/2$
1000 Mbps	¾	L=1	1	F_{chip}
1320 Mbps	1	L=1	1	F_{chip}

Low band - BPSK

Data Rate	FEC Rate	Code Length	Bits per Symbol	Symbol Rate
110 Mbps	½	L=12	2	$F_{chip}/12$
220 Mbps	½	L=6	2	$F_{chip}/6$
500 Mbps	¾	L=4	2	$F_{chip}/4$
660 Mbps	1	L=4	2	$F_{chip}/4$
1000 Mbps	¾	L=2	2	$F_{chip}/2$
1320 Mbps	1	L=2	2	$F_{chip}/2$

Low band - 4BOK

Data Rate	FEC Rate	Code Length	Bits per Symbol	Symbol Rate
55 Mbps	½	L=24	1	$F_{chip}/24$
110 Mbps	½	L=12	1	$F_{chip}/12$
220 Mbps	½	L=6	1	$F_{chip}/6$
500 Mbps	¾	L=4	1	$F_{chip}/4$
660 Mbps	1	L=4	1	$F_{chip}/4$
1000 Mbps	¾	L=2	1	$F_{chip}/2$
1320 Mbps	1	L=2	1	$F_{chip}/2$

High band - BPSK

Data Rate	FEC Rate	Code Length	Bits per Symbol	Symbol Rate
220 Mbps	½	L=12	2	$F_{chip}/12$
660 Mbps	¾	L=6	2	$F_{chip}/6$
1000 Mbps	¾	L=4	2	$F_{chip}/4$
1320 Mbps	1	L=4	2	$F_{chip}/4$

High band - 4BOK

Fig. 1.22. Available Data Rates.

In Figure 1.22 are listed the data rates available for the low band and the high band both BPSK modulation and Quaternary Bi-Orthogonal Keying (4BOK) modulation as function of code rate and spreading code length.

1.7.1 Frame Structure

The PHY frame format for all data rate modes is illustrated in Figure 1.23. The UWB PHY prepends the PHY header to the MAC header, calculates the Header Check Sequence (HCS), and appends this to the MAC header. If the size of the frame body plus Function of CheckSum (FCS), in bits, is not an integer multiple of the bits/symbol, then stuff bits are added following the FCS. The PHY preamble, is sent first in the packet, followed by the PHY and Medium Access Control (MAC) header, followed by Data field and finally the tail symbols.

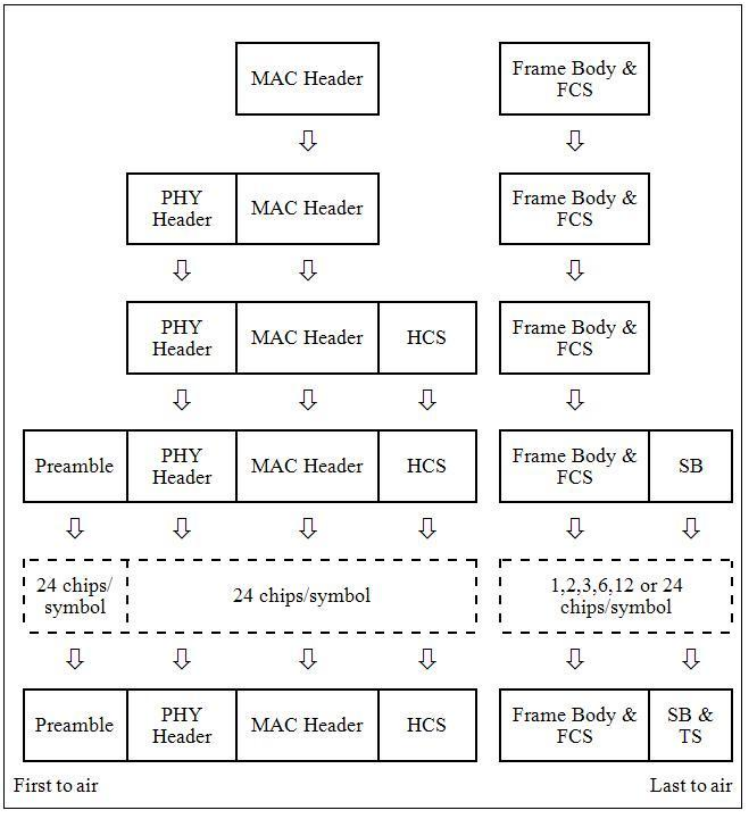

Fig. 1.23. Frame Structure.

1.7.2 Scrambler

The scrambler operation is employed to scramble the bits ensuring in this way an adequate number of bit transitions to support clock recovery. The scrambler shall be used only for the MAC header and frame body, whereas the PHY preamble and PHY header shall not be scrambled. The stream of downlink packets shall be scrambled by modulo-2 addition of the data with the output of the pseudo-random binary sequence generator, as shown in Figure 1.24.

The generator polynomial for the pseudo random binary sequence used by the scrambler is:

$$g(D) = 1 + D^{14} + D^{15} \tag{1.12}$$

where D is a single bit delay element. The polynomial forms not only a maximal length sequence, but also is a primitive polynomial. By the given

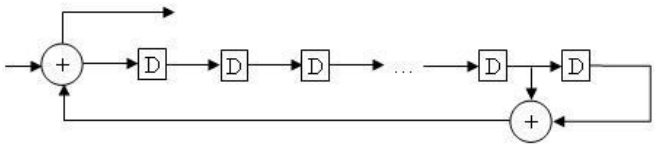

Fig. 1.24. Scrambler Structure.

generator polynomial, the corresponding pseudo random binary sequence, is generated as

$$x_n = x_{n-14} \oplus x_{n-15} \tag{1.13}$$

where $\oplus$ denotes modulo-2 addition. The initialization sequence is given by:

$$x_{init} = [x^i_{n-1} \cdot x^i_{n-2} \cdot x^i_{n-3} \cdot x^i_{n-4} \cdot ..... \cdot x^i_{n-12} \cdot x^i_{n-13} \cdot x^i_{n-14} \cdot x^i_{n-15}] \tag{1.14}$$

where x_i^{n-k} represents the binary initial value at the output of the k^{th} delay element. The scrambled data bits s_n are obtained as follows:

$$s_n = b_n \oplus x_n \tag{1.15}$$

where b_n represents the unscrambled data bits. On the receiver side, a de-scrambler, initialized with the same sequence x_{init} used in transmission, is required. The initialization sequence is typically recovered by information contained in the PHY header.

1.7.3 Convolutional Code

A Convolutional Encoder is a linear Finite State Machine composed by k step register and by n generator linear algebric functions [23]. The convolutional encoder is used to encode data so that the decoder can correct errors introduced due to noise in the channel. The input data, not necessarily binary data, are shifted b bits at the time in the register.

In Figure 1.25 is shown an example of encoder with *constraint length k=3*, *n=2* and *b=1*. The first three input bits 0,1 and 1 generate respectively the codes 00, 11 and 01. This example can be used to explain the general operation of all convolutional encoder. Another traditional and intuitive method to describe this technique is by *tree structure* (see Figure 1.26)

If the first input is zero, the coded symbol is shown on the top branch, while if the first bit is one then the coded symbol is that one on the bottom branch. In the same way, if the second bit is zero then it is needed to follow top branch of the tree, otherwise the bottom branch must be followed. Therefore, 32 distinct outputs are possible for the first five input bits. We can see

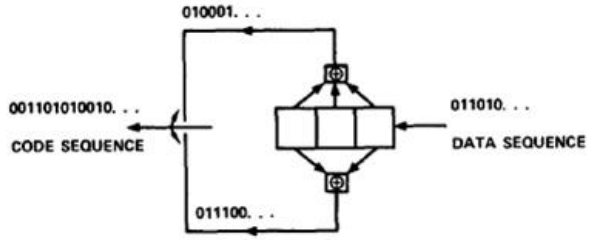

Fig. 1.25. Convolutiona Encoder Structure with k=3, n=2, b=1.

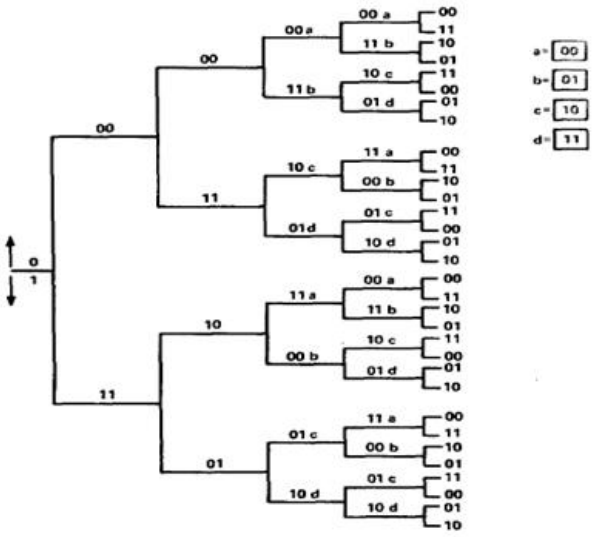

Fig. 1.26. Tree Diagram of a Convolutiona Encoder with k=3, n=2, b=1.

as the structure becomes completely repetitive after the first three branches, thus the constraint length k is the repetition period of the structure. The aforementioned described lead us to the diagram shown in Figure 1.27. This particular structure is called trellis diagram and it shows the cyclicity of the branch tree. In the figure, the branches generated by an input zero are depicted by a continuous line, while the branches generated by an imput one are depicted by a dotted line.

The totally repetitive structure of trellis diagram suggests a further reduction of the code representation in the state diagram shown in Figure 1.28.

The diagram states are labeled in accordance with trellis structure nodes, but being the states only related to the last two bits in input to the encoder, exactly these bits are used to describe it. An encoder with $b = 1$ bits in input, with a k stages register and n generator functions lead to a trellis structure with $2k - 1$ nodes and n code symbols per branch. The code rate is given by:

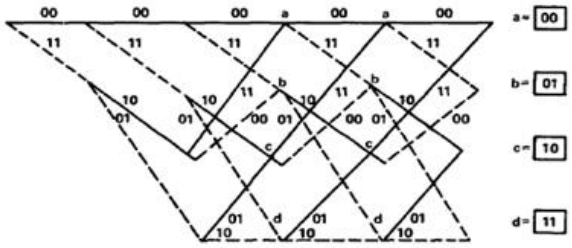

Fig. 1.27. Trellis Diagram of a Convolutiona Encoder with k=3, n=2, b=1.

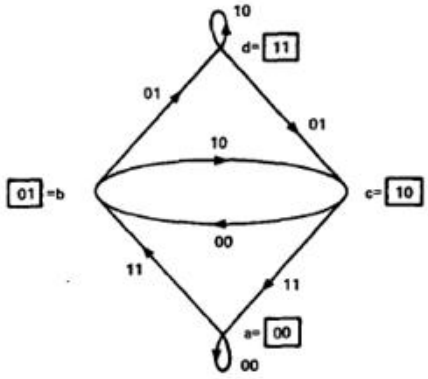

Fig. 1.28. State Automa of a Convolutiona Encoder with k=3, n=2, b=1.

$$R = \frac{1}{n} \tag{1.16}$$

The aforementioned described encoder has a code rate $R = 1/2$. The DS-UWB physical layer employs a convolutional encoder of rate 1/2 with a constraint length *k=6* or *k=4*.

1.7.4 Puncturing Operation

Puncturing is a procedure allows to increase the coding rate and so to increase the data rate [24],[25]. This technique consists of omitting some of the encoded bits in the transmitter (thus reducing the number of transmitted bits) and inserting a dummy "zero" metric into the convolutional decoder on the receive side in place of the omitted bits. This allows a 1/2 rate code to be transformed into a 3/4 rate code. Naturally, this allows to have higher data rates to the detriment of goodness of FEC (in fact lesser coded bits ara available to try the correction of possible errors). In Figure 1.29 a puncturing example implementing a code rate of 1/4 is shown.

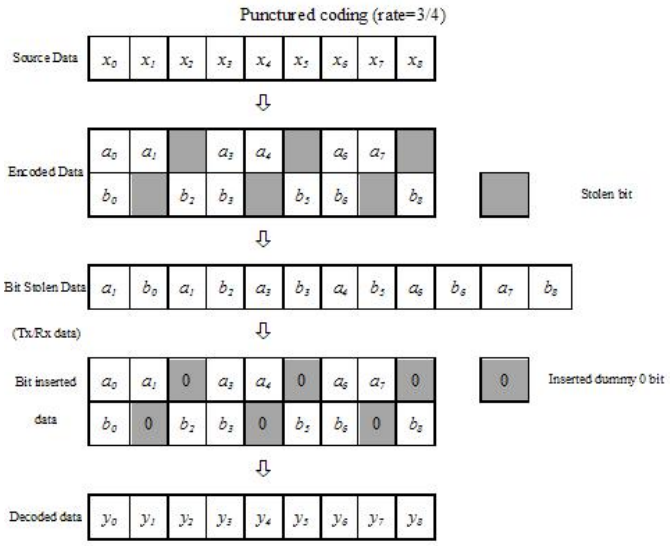

Fig. 1.29. Puncturing example.

1.7.5 Convolutional Interleaver

As the convolutional decoder is sensitive to burst errors, it is needed to use an interleaver block to disperse burst errors as shown in Figure 1.30.

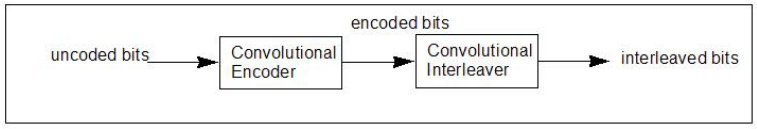

Fig. 1.30. Interleaving Scheme.

The interleaver performs a permutation of input bits so that the temporal order of the bits at the output of the interleaver is different from the temporal order at the interleaver input. In Figure 1.31 the structure of a convolutional interleaver is shown. The encoded bits are sequentially shifted in to the bank of N registers; each successive register provides J bits more storage than did the preceding. The $zero^{th}$ register provides no storage. With each new code bit the commutator switches to a new register, and the new code bit is shifted in while the oldest code bit in that register is shifted out. After the $(N-1)^{th}$ register, the commutator returns to the zeroth register and starts again. The deinterleaver performs the inverse operation. This is exactly the same except that the delays are reversed i.e. the first delay is $(N-1)\cdot J$ and the last delay is

0. The input and output commutators for both interleaving and deinterleaving must be synchronized.

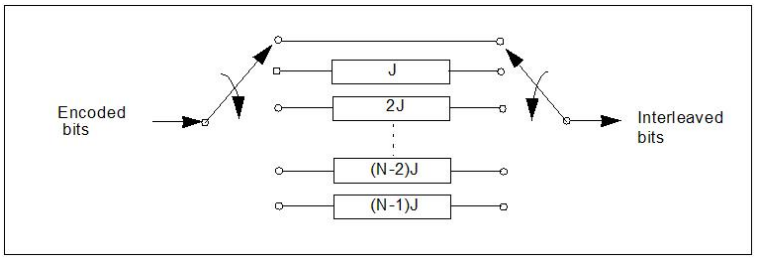

Fig. 1.31. Structure of a Convolutional Interleaver.

1.8 MB-OFDM Physical Layer

The MB-OFDM UWB physical layer provides a wireless PAN with data payload communication capabilities of 53.3, 55, 80, 106.67, 110, 160, 200, 320, and 480 Mbps [26]. The support of transmitting and receiving at data rates of 53.3, 106.67, 110, and 200 Mbps is mandatory. This system uses a total of 122 subcarriers that are modulated using Quadrature Phase Shift Keying (QPSK). A convolutional coding is used with a coding rate of 1/3, 11/32, 1/2, 5/8, and 3/4. The proposed UWB system also utilizes a Time-Frequency Code (TFC) to interleave coded data over 3 frequency bands (called a band group). Four such band groups with 3 bands each and one band group with 2 bands are defined. There are also 4 3-band TFCs and 2 2-band TFCs, which, when combined with the appropriate band groups provide the capability to define eighteen separate logical channels or independent piconets. Devices operating in band group $N \circ 1$ (the three lowest frequency bands) are denoted MODE 1 devices, it shall be mandatory for all devices to support MODE 1 operation, with support for the other band groups being optional (see Figure 1.32).

Instead, the relationship between carrier frequency and band number is given by:

$$Band\ Carrier\ Frequency = 2904 + 528 \times n_b \quad n_b = 1...14(MHz) \quad (1.17)$$

This definition provides a band numeration system for all channel having a spacing of 528 MHz in the frequency range from 3.1 GHz to 10.6 GHz (see Figure 1.33 for more details).

The transmitted signals can be described using a complex baseband signal notation as follows:

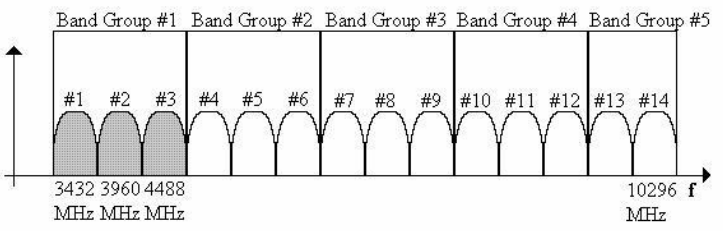

Fig. 1.32. Carrier Frequency for the Band Group.

Band Group	BAND_ID	Lower frequency	Center frequency	Upper frequency
1	1	3168 MHz	3432 MHz	3696 MHz
	2	3696 MHz	3960 MHz	4224 MHz
	3	4224 MHz	4488 MHz	4752 MHz
2	4	4752 MHz	5016 MHz	5280 MHz
	5	5280 MHz	5544 MHz	5808 MHz
	6	5808 MHz	6072 MHz	6336 MHz
3	7	6336 MHz	6600 MHz	6864 MHz
	8	6864 MHz	7128 MHz	7392 MHz
	9	7392 MHz	7656 MHz	7920 MHz
4	10	7920 MHz	8184 MHz	8448 MHz
	11	8448 MHz	8712 MHz	8976 MHz
	12	8976 MHz	9240 MHz	9504 MHz
5	13	9504 MHz	9768 MHz	10032 MHz
	14	10032 MHz	10296 MHz	10560 MHz

Fig. 1.33. OFDM Carrier Frequency.

$$r_{RF}(t) = Re[\sum_{k=0}^{N-1} r_k(t - kT_{SYM}) \cdot \exp(j2\pi f_k t)] \tag{1.18}$$

where $Re(\cdot)$ represents the real part of a complex variable, $r_k(t)$ is the complex baseband signal of the k^{th} OFDM symbol and is nonzero over the interval from 0 to T_{SYM}, N is the number of OFDM symbols, T_{SYM} is the symbol interval, and f_k is the center frequency for the k^{th} band. The exact structure of the k^{th} OFDM symbol depends on its location within the packet:

$$r_k(t) = \begin{cases} r_{preamble,k}(t) & 0 \leq k < N_{preamble} \\ r_{header,k-N_{preamble}}(t) & N_{preamble} \leq k < N_{header} \\ r_{data,k-N_{preamble}}(t) & N_{header} \leq k < N_{data} \end{cases} \tag{1.19}$$

All of the OFDM symbols $r_k(t)$ can be constructed using an inverse Fourier transform with a certain set of coefficient C_n, where the coefficients are defined as either data, pilots, or training symbols:

$$r_k(t) = \begin{cases} 0 & t \in [0, T_{CP}] \\ \sum_{n=-N_{ST}/2}^{N_{ST}/2} C_n \cdot e^{(j2\pi n \Delta_f)(t-T_{CP})} & t \in [T_{CP}, T_{FFT} + T_{CP}] \\ 0 & t \in [T_{FFT} + T_{CP}, T_{FFT} + T_{CP} + T_{GI}] \end{cases} \tag{1.20}$$

The parameters Δ_f and N_{ST} are defined as the subcarrier frequency spacing and the number of total subcarriers used, respectively. The resulting waveform has a duration of $T_{FFT} = 1/\Delta_f$. Shifting the time by T_{CP} creates the "circular prefix" which is used in OFDM to mitigate the effects of multipath. The parameter T_{GI} is the guard interval duration. In Figure 1.34 the available data rates for MODE 1 related to modulation, code rate, time spreading factor and bit number per OFDM symbol are listed .

Data Rate (Mbps)	Modulation	Coding rate (R)	Conjugate Symmetric Input to IFFT	Time Spreading Factor	Overall Spreading Gain	Coded bits per OFDM symbol (N_{CBPS})
53.3	QPSK	1/3	Yes	2	4	100
55	QPSK	11/32	Yes	2	4	100
80	QPSK	½	Yes	2	4	100
106.7	QPSK	1/3	No	2	2	200
110	QPSK	11/32	No	2	2	200
160	QPSK	½	No	2	2	200
200	QPSK	5/8	No	2	2	200
320	QPSK	½	No	1 (No spreading)	1	200
400	QPSK	5/8	No	1 (No spreading)	1	200
480	QPSK	¾	No	1 (No spreading)	1	200

Fig. 1.34. Available OFDM Data Rate.

1.8.1 Frame Structre

The OFDM frame is composed by Physical Layer Convergence Procedure (PLCP) preamble, PLCP header (PHY header, MAC header, header check sequence, tail bits, and pad bits), MAC frame body (frame payload plus FCS), tail bits, and pad bits. The PHY layer first pre-appends the PHY header plus the tail bits to the MAC header and then calculates the HCS over the combined headers and tail bits. The tail bits are added after the PHY header in order to return the convolutional encoder to the "zero state". The resulting HCS is appended to the end of the MAC header along with an additional set of tail bits. Pad bits are added to the end of the tail bits in order to align the data stream on the OFDM symbol interleaver boundaries. Tail bits are also added to the MAC frame body in order to return the convolutional encoder to the "zero state". Pad bits are added to the end of the tail bits in order to align the data stream on the OFDM symbol interleaver boundaries. The PLCP preamble is sent first, followed by the PLCP header, followed by an optional band extension sequence, followed by the frame payload, the FCS, the tail bits, and finally the pad bits. As shown in Figure 1.35, the PLCP header is always sent at an information data rate of 53.3 Mbps.

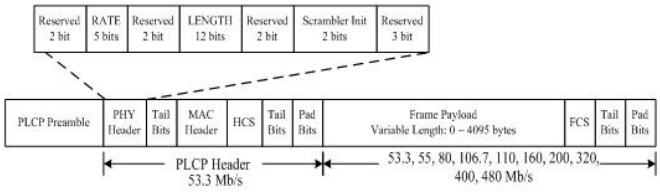

Fig. 1.35. Available OFDM Data Rate.

We have two type of PLCP preamble: standard PLCP preamble (see Figure 1.36) and the streaming-mode PLCP preamble (see Figure 1.37). A standard PLCP preamble shall be added prior to the PLCP header to aid receiver algorithms related to synchronization, carrier-offset recovery, and channel estimation. The standard PLCP preamble consists of three distinct portions: packet synchronization sequence,that shall be constructed by successively appending 21 periods of a time-domain sequence distinct for each piconet and whereto it is associated a particular time-frequency code; frame synchronization sequence, that shall be constructed by successively appending 3 periods of an 180 degree rotated version of the time-domain sequence and it is used to synchronize the receiver algorithm within the preamble; and the channel estimation sequence that shall be constructed by successively appending 6 periods of the OFDM training symbol in order to estimate frequency response of the channel.

The streaming-mode PLCP preamble is used for streaming mode transmission that is transmission in which continous stream of data packets are de-

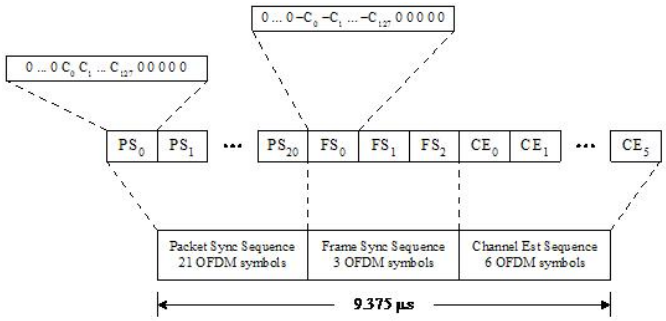

Fig. 1.36. Standard Preamble Structure.

livered. In the streaming packet mode, the first packet shall use the standard PLCP preamble, while the remaining packets shall use the streaming-mode PLCP preamble instead of the standard PLCP preamble. The streaming-mode PLCP preamble is composed by successively appending 9 periods of a time-domain sequence contrarily to standard PLCP preamble whose duration is 21 periods.

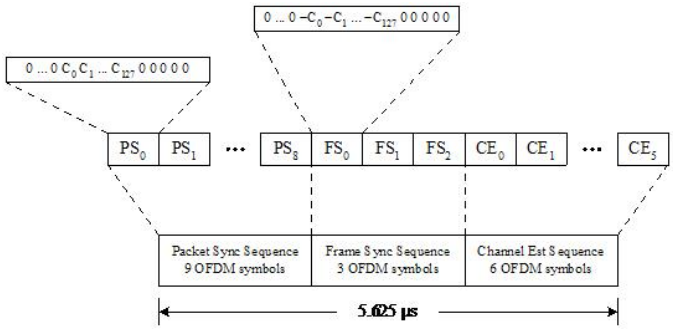

Fig. 1.37. Streaming-mode Preamble Structure.

1.8.2 OFDM Modulation

The OFDM subcarriers are modulated using QPSK modulation. The encoded and interleaved binary serial input data are divided into groups of 2 bits and converted into complex numbers representing QPSK constellation points. The conversion shall be performed according to the Gray-coded constellation mappings, shown in Figure 1.38.

The output values d are formed by multiplying the resulting $(I+jQ)$ value by a normalization factor of K_{MOD}. In particular, we have:

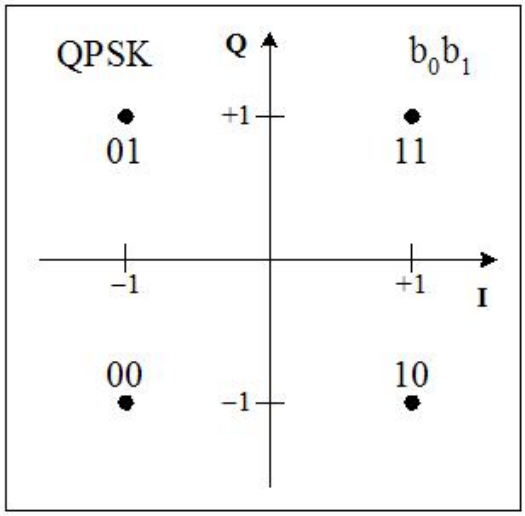

Fig. 1.38. QPSK Costellation.

$$d = (I + jQ) \times K_{MOD} \tag{1.21}$$

The normalization factor, K_{MOD}, depends on the base modulation mode and typically is set to $1/\sqrt{2}$. For information data rates of 50 and 80 Mbps, the stream of complex numbers is divided into groups of 50 complex numbers. We shall denote these complex numbers $c_{n,k}$, which corresponds to subcarrier n of OFDM symbol k, as follows:

$$\begin{aligned} c_{n,k} &= d_{n+50\times k} \qquad n = 0,\ 1, \ldots,\ 49, k = 0,\ 1,\ \ldots, N_{SYM} - 1 \\ c_{(n+50),k} &= d^*_{(49-n)+50\times k} \end{aligned} \tag{1.22}$$

where N_{SYM} denotes the number of OFDM symbols in the MAC frame body, tail bits, and pad bits. For information data rates of 110, 160, 200, 320 and 480 Mbps, the stream of complex numbers is divided into groups of 100 complex numbers given by:

$$c_{n,k} = d_{n+100\times k}\ n = 0,\ 1, \ldots,\ 99, k = 0,\ 1,\ \ldots, N_{SYM} - 1 \tag{1.23}$$

where N_{SYM} denotes the number of OFDM symbols in the MAC frame body, tail bits, and pad bits. An OFDM symbol $r_{data,k}(t)$ is defined as:

$$\begin{aligned} r_{data,k}(t) = \sum_{n=0}^{N_{SD}} [c_{n,k} \exp(j2\pi M(n)\Delta_F(t - T_{CP})) \\ + p_{\ \mathrm{mod}\ (k,127)} \sum_{n=-N_{ST}/2}^{N_{ST}/2} P_n \exp(j2\pi n\Delta_F(t - T_{CP}))] \end{aligned} \tag{1.24}$$

where N_{SD} is the number of data subcarriers, N_{ST} is the number of total subcarriers, and the function $M(n)$ defines a mapping from the indices 0 to 99 to the logical frequency offset indices -56 to 56, excluding the locations reserved for the pilot subcarriers, guard subcarriers and the DC subcarrier:

$$M(n) = \begin{cases} n-56 & n=0 \\ n-55 & 1 \le n \le 9 \\ n-54 & 10 \le n \le 18 \\ n-53 & 19 \le n \le 27 \\ n-52 & 28 \le n \le 36 \\ n-51 & 37 \le n \le 45 \\ n-50 & 46 \le n \le 49 \\ n-49 & 50 \le n \le 53 \\ n-48 & 54 \le n \le 62 \\ n-47 & 63 \le n \le 71 \\ n-46 & 72 \le n \le 80 \\ n-45 & 81 \le n \le 89 \\ n-44 & 90 \le n \le 98 \\ n-43 & n=99 \end{cases} \tag{1.25}$$

In each OFDM symbol, twelve of the subcarriers are dedicated to pilot signals in order to make coherent detection robust against frequency offsets and phase noise. The contribution due to the pilot subcarriers for the k^{th} OFDM symbol is given by the inverse Fourier Transform of the sequence P_n defined as

$$P_n = \begin{cases} \frac{1+j}{\sqrt{2}} & n = 15, 45 \\ \frac{-1-j}{\sqrt{2}} & n = 5, 25, 35, 55 \\ 0 & n = \pm 1, \pm 4, \pm 6, \pm 14, \pm 16, \pm 24, \pm 26, \pm 34, \pm 36, \pm 44, \pm 46, \pm 54, \pm 56 \end{cases} \tag{1.26}$$

For data rates lesser than 106.67 Mbps:

$$P_{n,k} = P^*_{-n,k}, \qquad n = -5, -15, -25, -35, -45, -55 \tag{1.27}$$

For 106.67 Mbps and all higher rate modes:

$$P_{n,k} = P_{-n,k}, \qquad n = -5, -15, -25, -35, -45, -55 \tag{1.28}$$

The polarity of the pilot subcarriers is controlled by pseudo-random sequence. In each OFDM symbol ten subcarriers are dedicated to guard subcarriers or guard tones. The guard subcarrier symbol definition for the nth subcarrier of the k-th symbol is given as follows:

$$P_{n,k} = p_{\,\mathrm{mod}\,(k+l,127)} \left(\frac{1+j}{\sqrt{2}} \right), \quad l = 0, 1, 2, 3, 4; \;\; n = 57 + l \tag{1.29}$$

For modes with data rates less than 106.67 Mbps:

$$P_{n,k} = P^*_{-n,k}, \qquad n = -57, ..., -61 \tag{1.30}$$

For 106.67 Mbps and all higher rate modes:

$$P_{n,k} = P_{-n,k}, \qquad n = -57, ..., -61 \tag{1.31}$$

where k=0 corresponds to the first OFDM symbol following the PLCP preamble.

1.9 TH-PPM Physical Layer

The TH-PPM physical layer provide a wireless PAN with data payload communication capabilities of 110, 200, 480 Mbps [27]. This model is based on a time hopping impulse radio transmission system proposed in the 2000 by Win e Scholtz [28]. The duration of the pulses determines essentially the bandwidth of the system. The delay of the pulse sequence (with respect to some arbitrary reference point) conveys the information of the symbol: smaller delay means that the information bit is +1, larger delay means -1 (or vice versa). In other words, the system uses Pulse pPosition Modulation (PPM). For the single-user case, it would be sufficient to transmit a single pulse per symbol, while in a multi access scenario it is needed to employ pulse sequence per symbol in order to avoid catastrophic collision. Each user have an univocal pulse sequence called Time Hopping (TH) code. For the restrictions imposed by the FCC, some modification are made to original model [23]:

- an innovative synchronization algorithm decreases the required length of the preamble for acquisition;
- the channel estimation procedure is accelerated by a multi-level approach that yields optimum Rake finger weights and equalizer weights;
- a linear combination of basis pulses allows to adapt the spectrum to the instantaneous interference situation;
- to decrease the problem of the equalizer length for large data rates, awe use multicode transmission for the 200 Mbps and 480 Mbps mode is used;
- the use of a rate 1/2 convolutional code is a good compromise between computational complexity for the decoding and coding gain at the desired value of Bit Error Rate (BER).

The data stream is first demultiplexed into substreams of approximately 110 Mbps each one (in the default mode, there is only one substream, while for the envisioned higher-rate modes, 2 and 4 substreams, respectively, are used) and then convolutionally encoded with a rate 1/2 coder. The resulting data streams are used to modulate the phase (BPSK) of a sequence of time-delayed pulses generated by a pulse generator. In addition, the phase of each pulse is also modulated by a pseudonoise sequence (see Figure 1.39).

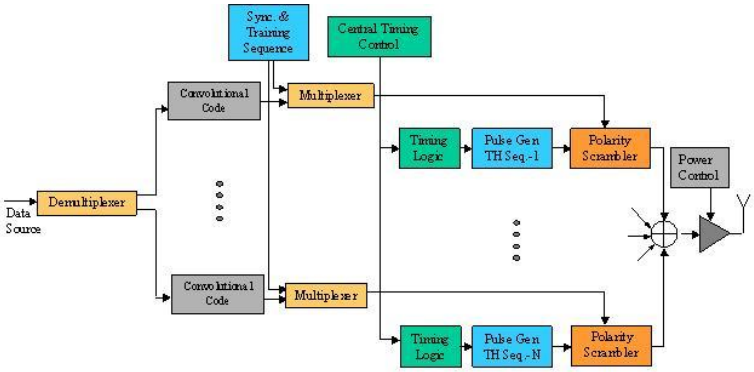

Fig. 1.39. TH-PPM Transmission Structure.

The timing of the pulses is determined by two facts: the pulse-hopping sequence, which determines the time within each frame that a pulse is generated and the required spacing of the pulses within each pulsegroup within a frame. By using a "polarity scrambling" of the pulses, the spectral crest factor of the transmitted signal, which increases the total power that can be transmitted while still fulfilling the FCC mask, was reduced. At the receiver, the acquisition part of the preamble is taken and used to determine the timing of the timing control part. Once this has been established, the "channel estimation part" of the preamble is used to determine the coefficients for the *Rake* receiver and the equalizer. A *Rake* receiver is composed by a set of corelators, each of them designed to reveiver a specific portion of signal due to multi path. After the despreading performed by corelators, the signals are combined using some specific technique such as "maximal ratio" [29]. For more details, see Figure 1.40.

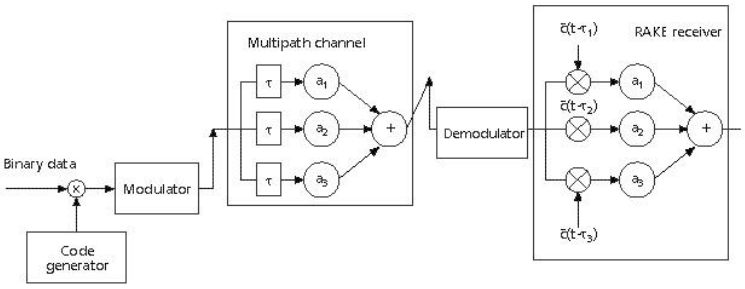

Fig. 1.40. Rake Receiver Structure.

The outputs of the various fingers of Rake receiver are combined and then delivered in a Minimum Mean Square Error (MMSE) equalizer. Finally, the data stream is decoded using a convolutional encoder as shown in Figure 1.41.

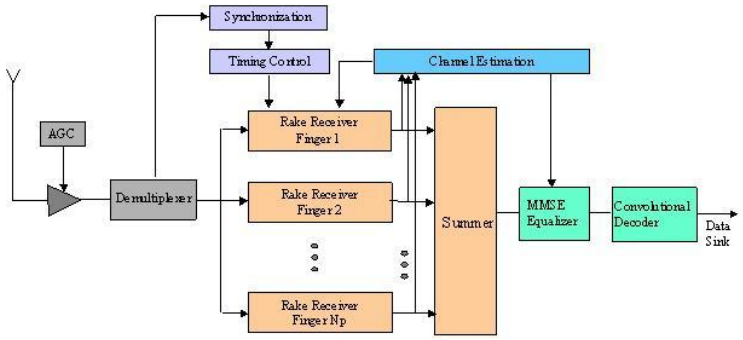

Fig. 1.41. TH-PPM Receiver Structure.

Typically, in the TH-PPM system, the transmitted signal can be represented by the following model

$$S_{tr}(t) = \sum_{j=-\infty}^{\infty} d_j \cdot b_{\lfloor j/N_f \rfloor} \cdot w_{tr}(t - jT_f - c_j^k T_c) = \sum_{k=-\infty}^{-\infty} b_k \cdot w_{seq}\,(t - kT_s) \tag{1.32}$$

where w_{tr} is the transmitted unit-energy pulse, T_f is the average pulse repetition time, N_f is the number of pulses representing one information symbol, and b is the information symbol transmitted. w_{seq} is the pulse sequence transmitted to represent one symbol. In order to allow the channel to be exploited by many users and avoid catastrophic collisions, a pseudo-random sequence c_j is assigned to each user. This sequence is called the time hopping sequence. The TH sequence provides an additional time shift of $c_j T_c$ seconds to the j^{th} pulse of the signal, where T_c is called the chip interval. To prevent pulses from overlapping, the chip interval must satisfy:

$$T_c \leq \frac{T_f}{N_c} \tag{1.33}$$

A "polarity scrambling" is performed multiplied each pulse by d_j , which are take values ± 1. This systems can be regarded as an random - code division multiple access radio signal (system with $T_f = T_c$ and a processing gain of N_f. Defining a sequence s_j as follows:

$$s_j = \begin{cases} d_{\lfloor j/N_c \rfloor} \;\; j - N_f \lfloor jN_c \rfloor = c_{\lfloor jN_c \rfloor} \\ 0 \quad otherwise \end{cases} \tag{1.34}$$

Then, assuming $T_f/T_c = N_c$, without loss of generality equation 1.34 can be expressed as:

$$S_{tr}(t) = \sum_{j=-\infty}^{\infty} s_j \cdot b^k_{\lfloor j/N_f N_c \rfloor} \cdot w_{tr}(t - jT_c) \tag{1.35}$$

For the acquisition and and channel estimation phase, there is no coding, so that $b^k_{j/N_f N_c} = 1 \ \ \forall j$. The basis pulse employed in the symbol transmission is a linear combination of delayed and attenuated pulses:

$$p(t) = \sum_{i=1}^{N_g} g(t - \tau_i) \tag{1.36}$$

where $g(t)$ is the fifth derivative of a Gaussian pulse:

$$g\left(t\right) = K_2 \left(-15\frac{t}{\sigma} + 10\frac{t^3}{\sigma^3} - \frac{t^5}{\sigma^5}\right) e^{-\frac{t^2}{2\sigma^2}} \tag{1.37}$$

where σ is chosen in order to respect the FCC normative:

$$\sigma = 5.28 \times 10^{-11} \tag{1.38}$$

The maximum number of pulses N_g is fixed to 4, but it could assume also a lesser value. Instead, the maximum admissible delay between pulse groups is fixed to:

$$max(\tau_i) = 0.5ns \tag{1.39}$$

This choice makes sure that the effective width of the transmitted pulse stays small. The linear combination of the Gaussian pulses into a basis pulse is done in order to additionally shape the spectrum, in order to optimally exploit the available power, as well as to suppress certain parts of the spectrum (both for compatibility reasons and for the suppression of interference in the matched-filter part of the receiver). Since transmitter and receiver should use the same shape of the basis pulses, they must communicate the choice of the delays and attenuations within the subgroup. It is the task of the receiver to compute the optimum pulse settings from the information in the training sequence. The information about delay and attenuation is then quantized into 8-bit information, so that a total of 64 bits have to be communicated from the receiver to the transmitter. This information is sent from the receiver to the transmitter in dedicated feedback packets, together with power control information. The information in those feedback packets has a stronger error protection than the regular data packets: namely, they use 16-bit CCITT parity check sequences in addition to the rate 1/2 convolutional coders.

1.10 Conclusions on Chapter 1

In this first chapter of my PhD Thesis, an overview on UWB system is given. The Chapter begins whit the description of UWB history: from the origin of this technology to nowadays when the increase of commercial interest leads to the standardization phase.

Then, the definition of UWB system is given: we described the characteristics that an UWB system should have in term of bandwidth and fractional band and the emission power limits.

Furthermore, we outlined the advantages and disadvantages of UWB technology and some of its many fields of application.

After, in the following of this chapter a mathematical description of the most important baseband impulses typically employed in the UWB transmission was given.

Finally, we describe the three main high rate alternative physical layer proposed for the UWB system.

In the first part, we explained the most impotant characteristics of DS-UWB system: from the frame structure to convolutional error correction technique employed to make more roboust the transmission. In particular, this physical layer will be better investigated in the Chapter 2 where a performance evaluation analysis and analytical treatment, based on MMSE receiver, are carried out. Furthermore, a higher level channel model for DS-UWB systems is presented in the Chapter 4.

The second part concerned the MB-OFDM physical layer: this treatment is a limited study presented simply to outline some difference between the DS-UWB and MB-OFDM standards.

We concluded with the TH-PPM standard: this is the basis of interfrence aware routing protocol that we will propose in the last chapter.

2

UWB Physical Layer Analysis

In this chapter of PhD Thesis, we discuss about UWB physical layer performance. A good analysis on physical layer does not prescind from channel model considerations. For this purpose, starting from UWB channel model presented in [30], we introduce, as proposed in [31], an explicit dependence on distance in the impulse response. The obtained channel model is then employed to evaluate the performance of UWB physical layer. In particular, we focused our attention on the DS-UWB physical layer: the system architecture has been implemented using a Matlab tool and simulation results are evaluated in terms of Bit Error Rate (BER) vs. transmitter-receiver distance and noise power spectral density and also in terms of Frame Error Rate (FER) carrying out our analysis varying the channel scenario and frame size. Despite the exhaustive performance evaluation analysis, we realized that the obtained results are not sufficient to cover any possible scenario: it could be specific cases in which a closed formula expressing the BER is needed. Therefore, carrying on my PhD experience, we focalized on the obtainment of a BER expression for different scenarios. For this purpose, as first step, a three-variables polynomial regression analysis is carried out on simulation results. In particular, we explained our analytic approach step by step and therefore two specific cases are shown in order to provide three variables functions of BER. However the approach based on the regression analysis shows some limitations: the BER function is only valid in the range covered by considered simulation results and it cannot be extended. This leads us to considered another mathematical approach: the performance evaluation of an ideal MMSE receiver is exploited to obtain a BER formula as function of distance, noise and data rates dependence. Finally, we concluded introducing dynamic scenarios: some considerations on mobility users are made and some simulation results are shown.

2.1 State of Art

General approaches for the channel modelling of UWB networks, taking into account multipath fading, shadowing and path loss have been considered in [30], [32] [33] and [11].

Since UWB systems do not fulfill the narrowband assumption, this principle obviously needs to be modified for UWB simulations. One possible approach [34] performs traditional ray tracing at different frequencies, and then combines the results. An alternative computes the impulse responses of the different rays (which depends on the interaction processes they go through) and adds up the contributions from the different rays [35], [36]. In [37] the authors used a combination of ray tracing with Finite-Difference Time-Domain (FDTD). In [38] and [39] the authors have independently suggested to combine deterministic components that are derived from ray tracing with a Rayleigh-distributed "clutter" that describes the contributions that stem from diffuse scattering and other propagation paths that are not covered by the ray tracing. In [32], the pathloss exponent was modelled as a random variable that changes from building to building. They found that the probability density function of this random variable can be well approximated by a Gaussian distribution, In [33], power attenuation of the paths was shown to follow a log-normal distribution, which is a function of the distance between the transmitter and receiver. In [33] and [30] the arrival of paths on each sampling time interval is not assumed, but they follow a cluster-based arrival rate. These characteristics are different from the classical IEEE 802.11 wireless networks channel models.

In the Saleh-Valenzuela (S-V) model, the paths arrival times are modelled through two Poisson distributions, where the first one is used to model the arrival time of the first path in each cluster, while the second one describes the arrival time of other paths in each cluster [33]. The path amplitudes follow a Rayleigh distribution law, with a double exponential decay model.

In [30], contrarily to [33], the authors propose a log-normal distribution to approximate the amplitudes of the power associated with the path components. However, in [30] and [33], the impulse response is not explicitly associated with the transmitter-receiver distance. Thus, following the model presented in [33], which is the formal model adopted by task group IEEE 802.15.3a during standard proposal evaluation phase, it is possible to account for the distance dependence modifying the first path time arrival and further attenuating other paths on the basis of the covered distance.

Concerning the received side we focalize our attention on the MMSE receiver [40]. In particular, in [41], the authors described the MMSE equalization:Linear Equalization (LE) and Decision-Feedback Equalization (DFE) are analyzed. LE and DFE are both suitable choices for DS-UWB system even if DFE is more performing for high date rate but equalization is also more complex in this case. In [41] and [31], the authors combine the RAKE receiver and the MMSE equalization to recover the transmitted signal, but in [42] and

is shown that the only MMSE receiver can be sufficient to recover the data. In order to reduce the receiver complexity, in our model we use only the MMSE receiver with a linear equalization.

In [31] a treatment on the performance of DS-UWB systems is already carried out, but respect to this work, we analyze DS-UWB under different multipath fading environment: in fact, in [31], the authors simply consider the fading scenario modelled with accordance to [30], where only four general indoor scenarios are proposed. Moreover, in our work, in addition to FER distance operative range, we provide also an accurate BER analysis for two different noise power thresholds.

2.2 UWB Channel Model

In our simulator, we utilise the UWB channel model provided by IEEE 802.15 channel modelling subcommittee [30]. This model is based on Saleh-Valenzuela approach [33], that distinguishes between cluster arrival time and ray arrival time modelled by two Poisson processes. The model proposed in [30] provides four different multipath fading scenario: CM1 (that describes a Line of Sight (LOS) scenario with a variable distance between transmitter and receiver), CM2 (that describe a No-Line of Sight (NLOS) scenario for short distance), CM3 (that depicts a NLOS scenario for medium distance between transmitter and receiver) and CM4 (that describes a very extreme NLOS scenario). The shadowing effect is also included in the model and is assumed to be common to all environments (in particular, it is modelled as a lognormal distribution with a log-standard deviation of 3 dB).

Table 2.1. Channel Characteristics

Scenario	**CM1**	**CM2**	**CM3**	**CM4**
Mean Excess Delay (nsec)	5.0	9.9	15.9	30.1
RMS delay spread (nsec)	5.0	8.0	15.0	25.0
Number of paths within 10 dB of peak	12.5	15.3	24.9	41.2
Number of pats with 80% of energy	20.8	33.9	64.7	123.3
Energy mean (dB)	-0.4	-0.5	0	0.3
Energy standard deviation (dB)	2.9	3.1	3.1	2.7

In Table 2.1 are summarized the mean characteristics of the channel model, further details can be found in [30]. In accordance with [31], a free path loss model is also employed. In particular, the path loss for the distance between transmitter and receiver $d \geq 1$ m is given by:

$$PL(d) = 20\log_{10}\left(\frac{4\cdot\pi\cdot d\cdot f_c}{c}\right) \ , \quad f_c = \sqrt{f_{\min}\cdot f_{\max}} \tag{2.1}$$

where f_c is the geometric center frequency, with f_{min} and f_{max} being the lower and the upper -10 dB cutoff frequencies of the power spectrum, and c is the light speed. As in [31], we incorporate the equation (2.1) in each channel realization in order to account the distance dependent. In particular, using (2.1), each path is attenuated by a factor depending on distance really covered: this distance is computed on the basis of needed time to reach the receiver under the assumption that the path speed is the light speed. Therefore, the resultant impulse response is given by:

$$\begin{aligned} &h(t,d) = \sum_{l=0}^{L}\sum_{k=0}^{K}\alpha_{k,l}(d_{k,l})\delta(t-T_l-\tau_{k,l}) \\ &k = 1...K\ ;\ l = 1...L \end{aligned} \tag{2.2}$$

where α_k is the multipath gain coefficient of the k^{-th} path in the l^{-th}, τ_l is the delay of l^{th} cluster, $\tau_{k,l}$ is the delay of the k_{th} path in the l_{th} cluster, X is the log-normal shadowing, L is the number of cluster and K is the number of rays. Furthermore, Average White Gaussian Noise (AWGN) effects, modelled as noise of parametric power, are added to the channel realizations. In 2.1 are plotted respectively a channel realization for the CM1 scenario and for a distance between transmitter and receiver of 5 meters (Figure 2.1a) and its average power decay profile (Figure 2.1b). In Figure 2.2 are shown the same curves for the CM2 scenario.

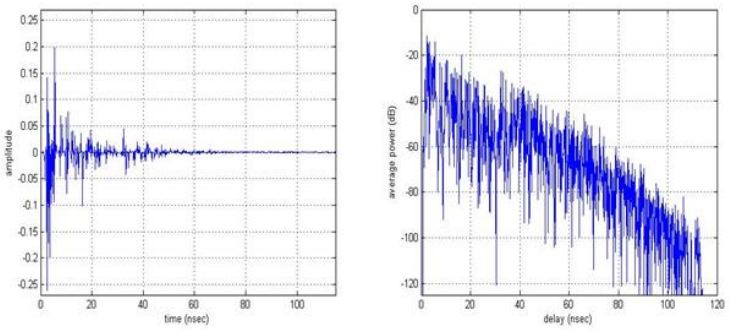

Fig. 2.1. a). Impulse response realization for CM1 scenario and for a distance between Tx-Rx of 5 meters. b) Average power decay profile for the same realization.

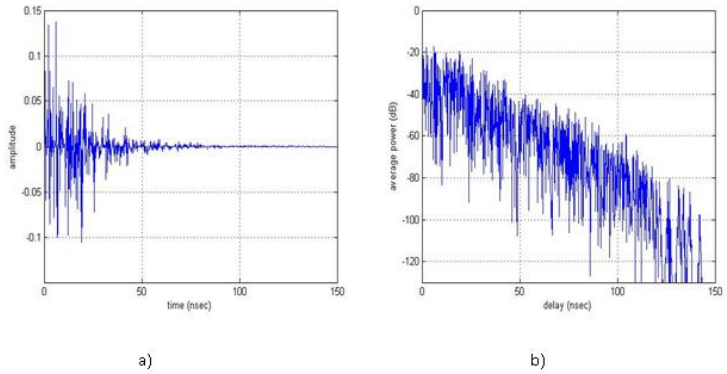

Fig. 2.2. a). Impulse response realization for CM1 scenario and for a distance between Tx-Rx of 5 meters. b) Average power decay profile for the same realization.

2.3 DS-UWB architecture

In this chapter, our reference scenario is a DS- UWB system in accordance with [9]. In Figure 2.3a, we show the transmitter structure of a DS-UWB system. As described in the standard [9], the data sequence is scrambled in order to ensure an adequate number of bit transitions to support clock recovery. After, a convolutional encoder is used to encode data so that the decoder can correct errors, due to noise, introduced in the channel. In particular, we use a convolutional encoder with a constraint length k=6 (that is an encoder in which the number of inputs in the encoder diagram is 6) that realizes a code rate of 1/2 Instead, the other code rates are obtained using the puncturing technique (some of the encoded bits are omitted in the transmission increasing in this way the coding rate). Therefore, the encoded data are interleaved with a convolutional interleaver in order to disperse burst errors to which the decoder is sensitive and then modulated using BPSK modulation. Each modulated bit is successively spreaded using a ternary Pseudo Noise (PN) spreading code to form the transmit sequence. The combination of the Spreading Factor (SF), (that is the length of the spreading code), the code rate and used modulation forms the current data rate (in Section 1.7 are shown the available data rates). In Figure 2.3b, is shown the receiver structure. The transmitted bits sequence is estimated using a MMSE receiver because it is able to gather multipath energy and reject intersymbol and interchip interferernce for these channels to a much greater extent than RAKE receivers with 4 and 8 arms [41]. The MMSE receiver consists of a bandpass filter and an adaptive filter. The bandpass filter suppresses noise and interference out of signal band to increase Signal to Noise Ratio (SNR). As in [41] is proved tha the only MMSE receiver can be sufficient to recover the data, in our model we use only the MMSE receiver with a linear equalization in order to reduce complexity. At each bit epoch, a

bit decision is made at the output of the correlator and it is then fed back to the adaptive filter. This receiver uses an adaptive algorithm called Normalised Least Minimum Square (NLMS) to upgrade weights vector *W*. The equation to calculate the weights is specified below:

$$W(i) = W(i-1) + \mu_m \; e(i) \frac{u^*(i)}{\varepsilon + u^H(i)u(i)} \tag{2.3}$$

In (2.3), μ_m is the step size, while ϵ is a small positive constant that has been added (to denominator) to overcome potential numerical instability in the update of the weights; *e(i)* is the error associated with the i-th estimated bit; *u(i)* represents the discrete input signal of the adaptive filter. After this operation, the estimated bits are demodulated and deinterleaved and successively are sent in a Viterbi decoder, that recoveries some of errors introduced by the channel. The decoded bits are finally descrambled in order to reconstruct the data sequence. In our simulations, we use a MMSE receiver with 16 taps per observation window and a step size of 0.5. Besides, we work in the piconet channel 1 of the lower band with a chip rate of 1313 MHz and, for every simulation campaign, we fixed the transmission power to -9 dBm in accordance with the FCC mask.

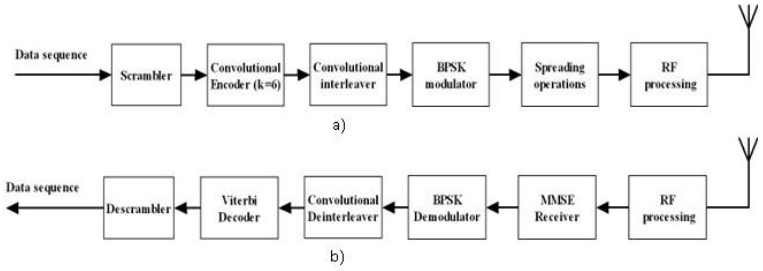

Fig. 2.3. Transmitter and receiver structure.

2.4 Performance Evaluation

Many simulation campaigns have been lead out in order to evaluate the performance of the DS-UWB physical layer for the UWB technology. DS-UWB system has been investigated in terms of BER for different noise power level and in terms of FER for various frame dimension (in this case for a fixed noise threshold) both for the CM1 and CM2 scenario described in [30]. In the following, BER simulation results and FER simulation results will be analyzed.

2.4.1 BER Simulation Results

Our simulation campaigns show how the UWB systems are very sensitive to the transmitter-receiver distance and to noise power. In particular, in Figure 2.4 the curves of average BER in a CM1 scenario are plotted with a noise power of -55 dB, for 28, 55, 110, 220, 500 Mbps data rates. In this case, the average BER for the lower data rate increases very slowly for distance lesser than 10 meters, while 220 and 500 Mbps data rates are more sensible to distance between transmitter and receiver and BER rises quickly already around 6 meters. This is due to the lower data rates capacity to reject Inter-Symbol Interference (ISI) better than higher rate because of longer spreading codes. In fact longer ternary spread sequence have more zero valued windows than shorter sequence in their autocorrelation function, so interferences due to multipath that are within these windows can be easily eliminated. In Figure 2.5, we show the average BER trend for the CM2 scenario for a noise power of -55dB. In this case, the performance degrades because CM2 describes an NLOS scenario, so the absence of a stronger direct component makes the impact of the ISI more damaging. We can see how only a 28 Mbps data rate allows communication for distances between transmitter and receiver higher than 10 meters, while the average BER of 55 and 110 is more influenced by distance respect the LOS scenario. For both previous cases, the background noise is not able to high influence the system performance, because it has a power level that is very lower than the one of the transmitted signal.

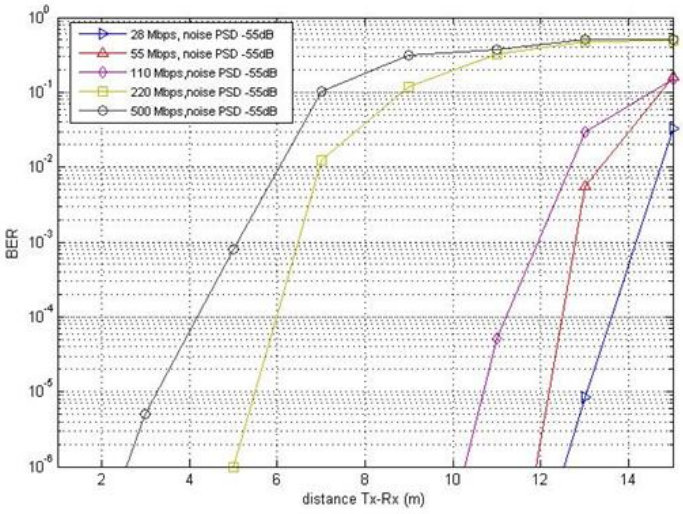

Fig. 2.4. BER vs. distance Tx-Rx for CM1 scenario, noise power of -55dB.

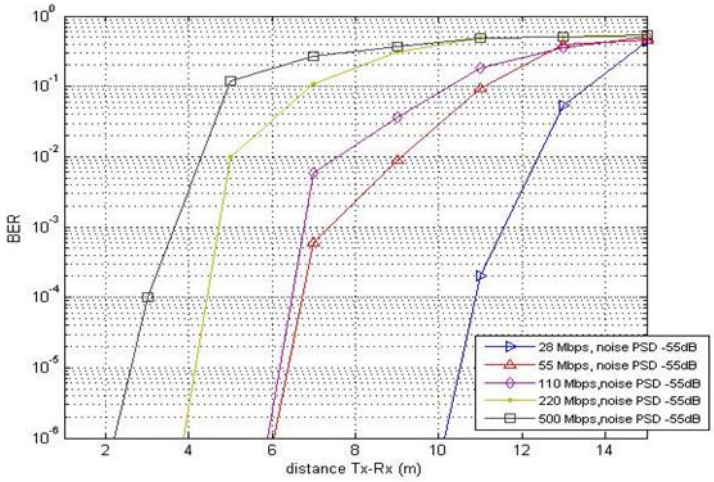

Fig. 2.5. BER vs. distance Tx-Rx for CM2 scenario, noise power of -55dB.

In Figure 2.6 the average BER course vs. the distance between transmitter and receiver is depicted for the previous data rates and for CM1 scenario in the presence of a noise power of -35 dB. If we increase the noise up to -35dB, we can observe how the performances of 28 and 55 Mbps data rates worsen very quickly, because the presence of noise adds to the negative effects of the ISI: In fact, we can see how the BER rises quickly for distance lesser than 10 meters also for the lower data rates as 28 and 55 Mbps. In Figure 2.7 the average BER trend for the CM2 scenario and in presence of high noise power level are plotted. Also for the CM2 scenario, the presence of a higher noise level (noise power of -35 dB) reduces the performance of the system and so the supported operative range (e.g. the operative range of 28 Mbps data rate is reduced to only 5 meters, while 110 Mbps falls to only 2 meters).

2.4.2 FER Simulation Results

Our simulation campaigns show as the UWB systems are also sensitive to the frame size, so an increase of frame length can influences the system performances reducing the operative range in some case. In the following we show and analyse the results for CM1 and CM2 scenario with a frame length of 128 and 1024 bytes and a PSD noise of -55 dB.

In Figure 2.8 and Figure 2.9 the curves of average FER in a CM1 scenario for 28, 55, 110, 220, 500 Mbps data rates and for two different frame size (128 bytes in Figure 2.8 and 1024 bytes in Figure 2.9) are plotted. Typically, the FER, as demonstrated in [43], is a function of the BER distribution but it is also a function of the frame size, therefore if the frame size is made to

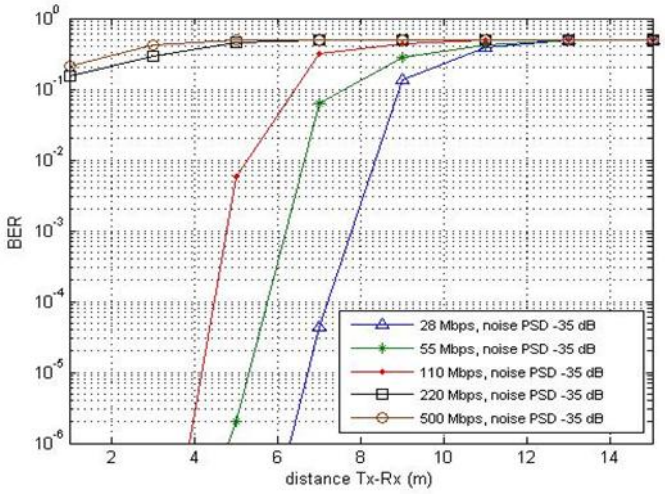

Fig. 2.6. BER vs. distance Tx-Rx for CM1 scenario, noise power of -35dB.

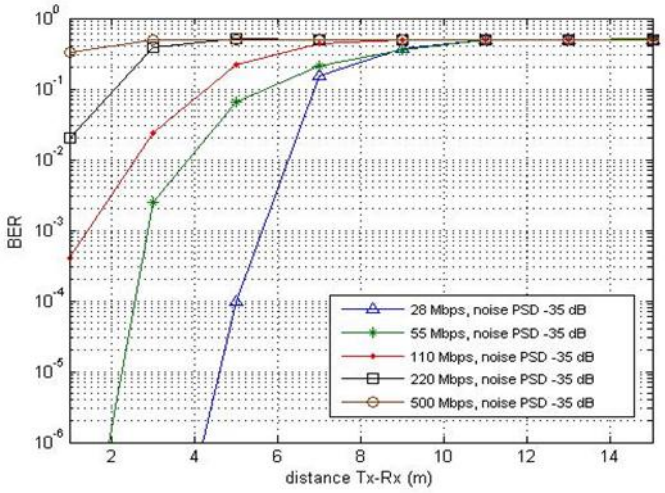

Fig. 2.7. BER vs. distance Tx-Rx for CM2 scenario, noise power of -35dB.

go towards one (degenerate case) the FER converges towards the BER, vice versa at an increase of the frame size the FER tends to one. This trend is also confirmed for the DS-UWB systems, in fact we can see as the FER for 1024 bytes frame size is greater than FER obtained for 128 bytes. This aspect is very important for a UWB system because an increase of FER can reduce the operative range of a certain data rate (we remember that the operative range is the distance for which $FER < 0.08$ with 90% probability, as defined in the proposed standard [9]). In particular, we can see as the operative range of 110 Mbps decrease from 11.6 meters, obtained for a frame size of 128 bytes, to 9.4 meters obtained for 1024 bytes. Instead, we observe that lower data rates (28 and 55 Mbps) are less sensitive to frame dimension and so the operative range rather decreases.

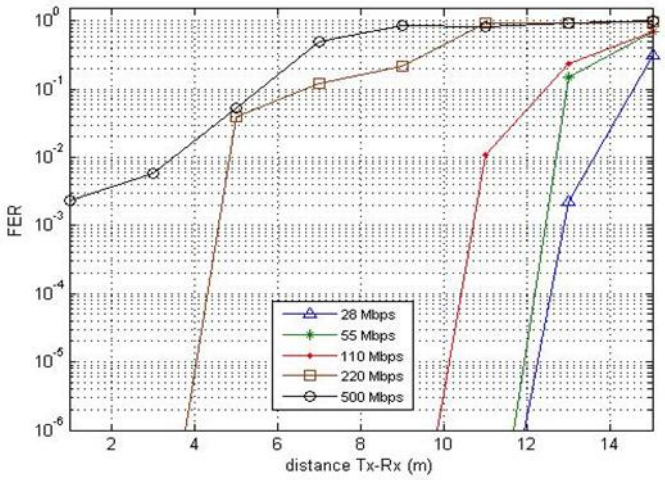

Fig. 2.8. FER vs. distance for CM1 scenario with a frame size of 128 bytes.

Figure 2.10 and Figure 2.11 show the curves of average FER in a CM2 scenario for 28, 55, 110, 220, 500 Mbps data rates and for 128 bytes frame size (in Figure 2.10) and for 1024 bytes frame (in Figure 2.11). In this case, the increase of frame dimension also affects lower data rates: e.g. we can observe the 28 Mbps operative range reduce up to 9.5 meters for a dimension of 1024 bytes, whereas for 55 Mbps we observe an operative range reduction of about 2 meters (from 7.7 meters for a frame size of 128 bytes to 6 meters obtained for a frame of 1024 bytes). In Table 2.2, we summarize the operative range for all data rate in the CM1 and CM2 scenarios with a frame size of 128 bytes and of 1024 bytes.

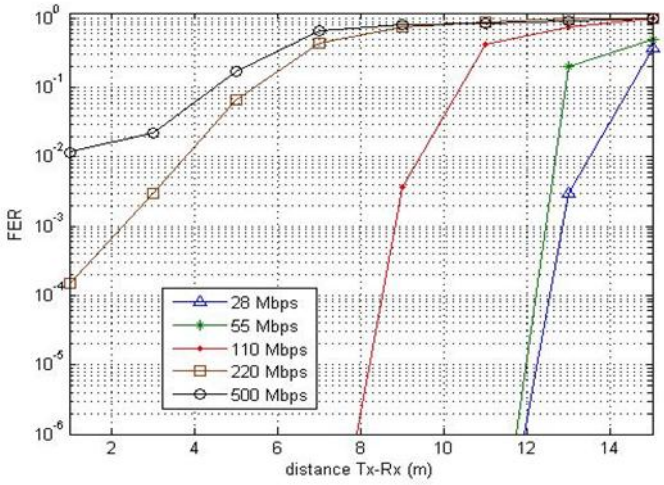

Fig. 2.9. FER vs. distance for CM1 scenario with a frame size of 1024 bytes.

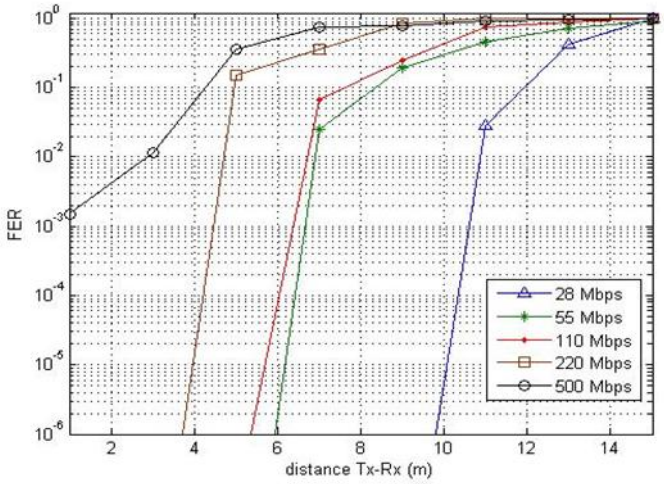

Fig. 2.10. FER vs. distance for CM2 scenario with a frame size of 128 bytes.

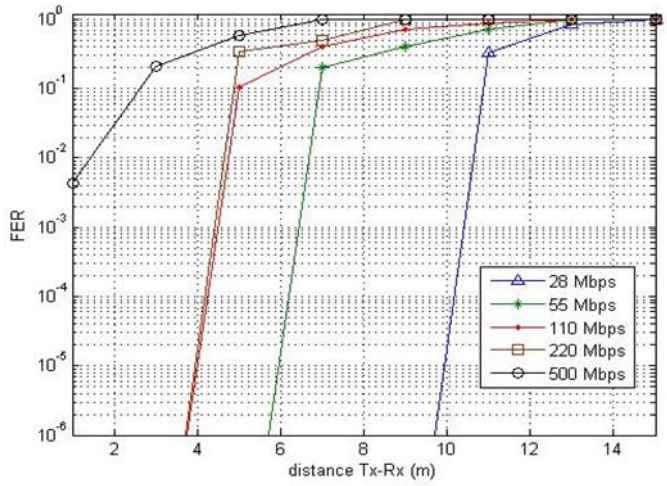

Fig. 2.11. FER vs. distance for CM2 scenario with a frame size of 1024 bytes.

Table 2.2. Operative Range for DS-UWB (in meters)

Data Rate	**CM1 (128 B)**	**CM1 (1024 B)**	**CM2 (128 B)**	**CM2 (1024 B)**
28 Mbps	13.5	13.4	11.3	9.5
55 Mbps	12.1	11.8	7.7	6
110 Mbps	11.6	9.4	7	4.5
220 Mbps	6.5	5.1	4.2	3.5
500 Mbps	5.1	3.7	3.4	1.8

2.5 Regression Analysis

The goal of our regression analysis is to obtain, starting by simulation results, three variables functions describing BER trends. For this purpose, we use Mathworks' Matlab tool, further details on regression technique can be found in [44]. Since the BER assumes very low values for lower level of noise (in particular for CM1 scenario), we carried out the regression analysis on the BER logarithm reducing, in this way, the percentage of committed error. If we denote with $F(\cdot)$ our unknown function and with x, y and z the three variables expressing the FER or BER dependence on the same three transmission parameters, then the general equation of the logarithm of $F(\cdot)$, for a fixed value of y and z, can be expressed with a n_{th} order polynomial regression:

$$\log_{10}[F(x)] = (a_n x^n + \ldots + a_3 x^3 + a_2 x^2 + a_1 x + a_0) \tag{2.4}$$

where $a_i = f(y)$ with i=0,1,... n.

Therefore the $F(\cdot)$ function can be represented in the following way:

$$F(d) = 10^{\left(\begin{bmatrix} a_0 & a_1 & \dots & a_n \end{bmatrix} \cdot \begin{bmatrix} 1 \\ x \\ \vdots \\ x^n \end{bmatrix} \right)} = 10^{\langle a \rangle \cdot \langle x \rangle_n^T} \tag{2.5}$$

where the notation $\langle \cdot \rangle$ is used to represent a row vector and $\langle \cdot \rangle^T$is the transpose operator applied to the vector. In (2.5) $\langle x \rangle_n^T$ is a $(n+1) \times 1$vector.

Considering another polynomial regression analysis on the a_i coefficients for different y values, the polynomial expression of the a_i terms can be represented as follows:

$$a_i\,(y) = b_{m,i} y^m + \ldots + b_{2,i} y^2 + b_{1,i} y + b_{0,i} \tag{2.6}$$

with *i=0,. . . ,n.*

Therefore the coefficients of the y variable can be expressed in the following way:

$$\langle a\,(y) \rangle = \begin{bmatrix} b_{0,0} & b_{0,1} & \ldots & b_{0,m} \\ b_{1,0} & \ldots & \ldots & \ldots \\ \ldots & \ldots & \ldots & \ldots \\ b_{n,0} & \ldots & \ldots & b_{n,m} \end{bmatrix} \cdot \begin{bmatrix} 1 \\ y \\ \vdots \\ y^m \end{bmatrix} = B \cdot \langle y \rangle_m^T \tag{2.7}$$

where $\langle y \rangle_m^T$ represent a $(m+1) \times 1$ vector.

A third regression is finally carried out on each coefficient of B, introducing in this way also the dependence on variable z.

Therefore the coefficients of matrix B can be expressed as:

$$b_{i,j}\,(z) = c_{m',(i,j)} z^{m'} + \ldots + c_{2,(i,j)} z^2 + c_{1,(i,j)} z + c_{0,(i,j)} \tag{2.8}$$

Substituting (2.8) in (2.7) for each coefficient, we obtain the following formula:

$$\langle a\,(y,z) \rangle = \begin{bmatrix} b_{0,0}(z) & b_{0,1}(z) & \ldots & b_{0,m}(z) \\ b_{1,0}(z) & \ldots & \ldots & \ldots \\ \ldots & \ldots & \ldots & \ldots \\ b_{n,0}(z) & \ldots & \ldots & b_{n,m}(z) \end{bmatrix} \cdot \begin{bmatrix} 1 \\ y \\ \vdots \\ y^m \end{bmatrix} = B(z) \cdot \langle y \rangle_m^T \tag{2.9}$$

In (2.8) and (2.9), the polynomials $b_{i,j}(z)$ and the degrees m, m' and n depend on considered scenario (CM1, CM2, CM3 or CM4). Substituting (2.9) within (2.5), the following equation can be obtained:

$$F\,(x,y,z) = 10^{\left([B(z) \cdot \langle y \rangle_m^T] \langle x \rangle_n^T \right)} \tag{2.10}$$

where the $F = f(x, y, z)$.

Equation (2.10) is a general formula useful for all scenarios. The goodness of a regression analysis can be confirmed by two distinct indexes: the *determination coefficient* R^2 and the *relative error percentage* [44]. R^2 can take on any value between 0 and 1, with a value closer to 1 indicating that a greater proportion of variance is accounted for by the model (e.g. R^2 value of 0.8234 means that the fit explains 82.34% of the total variation in the data about the average). The *determination coefficient* R^2 is given by:

$$R^2 = 1 - \frac{SSE}{SST} \tag{2.11}$$

where the *Sum of Squares due to Error* (SSE) and the *Sum of Squares about the Mean* (SST) are respectively defined as:

$$\begin{aligned} SSE &= \|y - \hat{y}\|^2 \\ SST &= \|y - \bar{y}\|^2 \end{aligned} \tag{2.12}$$

In the previous formulas, the operator $\|\cdot\|$ represents the *Euclideal Norm*, y is the ordinate simulated data point vector, $\hat{y}$ is the resulting fit data point vector, while $\bar{y}$ is the mean value of vector y.

The *relative error percentage* is instead defined as:

$$e_{rel} = \left| \frac{y - \hat{y}}{y} \right| \times 100 \tag{2.13}$$

In this case, the polynomial approximation is considered good if the relative error is less than 8% for each data point.

In the following $F(x, y, z)$ function will be explicated for the BER and FER respectively.

2.5.1 BER Regression Analysis

The goal of BER regression analysis is to obtain an expression for the average BER as a function of the distance d (in meters), the noise PSD p (in dB) and data rate r (in Mbps). Since the BER assumes very low values for lower level of noise (in particular for CM1 scenario), we carried out the regression analysis on the BER logarithm reducing, in this way, the percentage of error. Considering the equation previous treatment, the following equation can be obtained for the BER:

$$\begin{aligned} &BER(d, p, r) = 10^{\left(\left[B(r)\cdot\langle p\rangle_m^T\right]\langle d\rangle_n^T\right)}; \\ &1m \le d \le 15m; \;\; -55dB \le p \le -15dB; \\ &r \in \left[\, 28Mbps, \quad 55Mbps, 110Mbps, 220Mbps, 500Mbps \,\right]; \end{aligned} \tag{2.14}$$

where the $BER = f(d, p, r)$. Equation 2.14 is a general formula useful for all scenarios. In the following some examples of these functions for a fixed data rate and scenario are shown.

Specifically, for the CM1 scenario, the terms of matrix B are polynomials of degree 4:

$$\begin{aligned}
&b_{0,0}(r) = 0;\\
&b_{0,1}(r) = 5.83 \cdot 10^{-8} r^4 - 5.14 \cdot 10^{-5} r^3 + 1.34 \cdot 10^{-2} r^2 - 1.21\ r + 27.1;\\
&b_{0,2}(r) = 4.96 \cdot 10^{-9} r^4 - 4.37 \cdot 10^{-6} r^3 + 1.14 \cdot 10^{-3} r^2 - 0.103\ r + 2.31;\\
&b_{0,3}(r) = 7.63 \cdot 10^{-11} r^4 - 6.72 \cdot 10^{-8} r^3 + 1.76 \cdot 10^{-5} r^2 - 1.59 \cdot 10^{-5} r + 3.67 \cdot 10^{-2};\\
&\vdots
\end{aligned} \tag{2.15}$$

The goodness of this fit is confirmed by the observed value of the *determination coefficient* R^2 over the polynomial function [11]: in fact, the minimum observed value of R^2 is 0.9986 for r =500 Mbps. Another parameter that confirms the accuracy of regression is the relative error: in this case the maximum value observed on all rates is 6.12% still for r =500 Mbps. If we fix the value of r to 28 Mbps in (2.14), we obtain the following elements for $\boldsymbol{B}$:

$$B(28) = B_1 = \begin{bmatrix}
0 & 2.7576 & 2.3623 \cdot 10^{-1} & 4.4983 \cdot 10^{-3}\\
0 & -2.6200 & -2.2252 \cdot 10^{-1} & -3.7242 \cdot 10^{-3}\\
0 & 7.2367 \cdot 10^{-1} & 6.1369 \cdot 10^{-2} & 9.9730 \cdot 10^{-4}\\
0 & -8.5716 \cdot 10^{-2} & -7.2641 \cdot 10^{-3} & -1.1693 \cdot 10^{-4}\\
0 & 4.6446 \cdot 10^{-3} & 3.9324 \cdot 10^{-4} & 6.3065 \cdot 10^{-6}\\
0 & -9.4918 \cdot 10^{-5} & -8.0273 \cdot 10^{-6} & -1.2853 \cdot 10^{-7}
\end{bmatrix} \tag{2.16}$$

which, substituted in (2.14), leads to:

$$\begin{aligned}
&BER(d,p,28) = 10^{\left(\left[B_1 \cdot \langle p \rangle_3^T\right] \cdot \langle d \rangle_5^T\right)}\ ,\\
&1m\ <\ d\ \leq\ 15m\ \ ,\\
&-55\ dB\ \leq\ p\ \leq\ -15\ dB
\end{aligned} \tag{2.17}$$

In Figure 2.12a the BER curve plotted using (2.17) is shown. The observed value of R^2 is in this case 0.9987. The relative error committed by regression analysis is plotted in Figure 2.12b (in this case the maximum relative error is 5.7%).

Instead for data rate 500 Mbps the coefficients of matrix $\boldsymbol{B}$ are:

$$B(500) = B_2 = \begin{bmatrix}
0 & 2.9904 \cdot 10^{-1} & 2.6754 \cdot 10^{-2} & 5.4362 \cdot 10^{-4}\\
0 & -7.3799 \cdot 10^{-2} & -7.2802 \cdot 10^{-3} & -1.5727 \cdot 10^{-4}\\
0 & 4.9434 \cdot 10^{-3} & 5.2725 \cdot 10^{-4} & 1.3152 \cdot 10^{-5}\\
0 & 3.1564 \cdot 10^{-4} & 2.3988 \cdot 10^{-5} & 1.9991 \cdot 10^{-7}\\
0 & -4.7717 \cdot 10^{-5} & -4.2297 \cdot 10^{-6} & -7.0111 \cdot 10^{-8}\\
0 & 1.4224 \cdot 10^{-6} & 1.2916 \cdot 10^{-7} & 2.2932 \cdot 10^{-9}
\end{bmatrix} \tag{2.18}$$

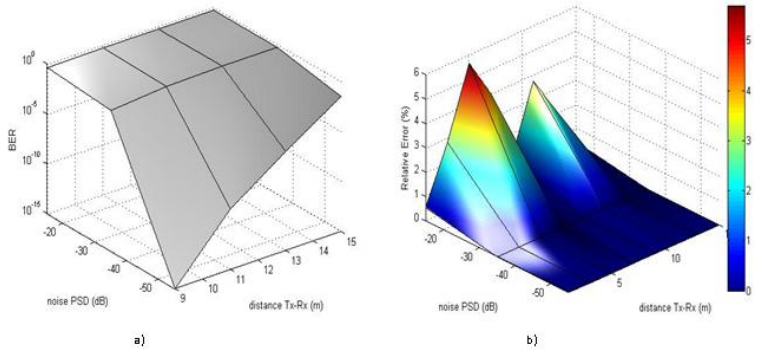

Fig. 2.12. a) BER vs. distance and noise PSD for rate 28 Mbps, CM1 scenario. b) Relative error committed by regression analysis.

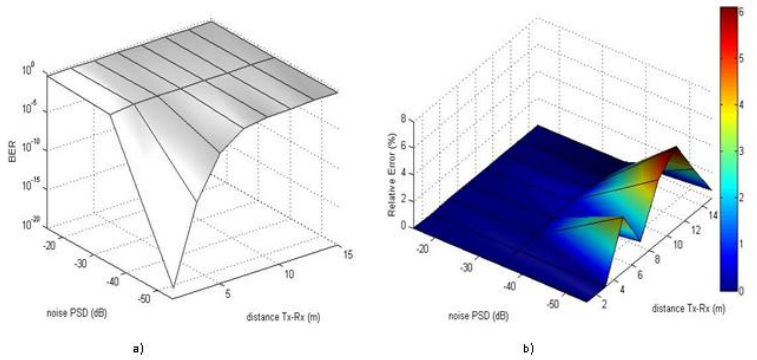

Fig. 2.13. a) BER vs. distance and noise PSD for rate 500 Mbps, CM1 scenario. b) Relative error committed by regression analysis.

which, substituted in (2.14), leads to:

$$\begin{array}{l} BER(d,p,500) = 10^{\left(\left[B_2 \cdot \langle p \rangle_3^T\right] \cdot \langle d \rangle_5^T\right)} \\ 1m \ < \ d \ \leq \ 15m \quad , \\ -55 \ dB \ \leq p \ \leq \ -15 \ dB \end{array} \tag{2.19}$$

In Figure 2.13a we can see the BER trend, obtained by (2.19) for data rate 500 Mbps in a CM1 scenario. In this case, the *determination coefficient* R^2 over the polynomial function is 0.9986 as affirmed previously, while the relative error committed by regression approximation is plotted in Figure 2.13b, with a maximum relative error of 6.12%.

For the CM2 scenario, the terms of matrix B are even polynomials of degree 4:

$$
\begin{aligned}
&b_{0,0}(r) = 0;\\
&b_{0,1}(r) = \text{-}2.89 \cdot 10^{\text{-}8} r^4 + 2.62 \cdot 10^{\text{-}5} r^3 \text{ -}7.26 \cdot 10^{\text{-}2} r^2 + 73.1\ r \text{ -}20.7;\\
&b_{0,2}(r) = \text{-}2.50 \cdot 10^{\text{-}9} r^4 + 2.28 \cdot 10^{\text{-}6} r^3 \text{ -} 6.34 \cdot 10^{\text{-}4} r^2 + 6.41\ r \cdot 10^{\text{-}2} \text{-}1.81;\\
&b_{0,3}(r) = \text{-}3.83 \cdot 10^{\text{-}11} r^4 + 3.51 \cdot 10^{\text{-}8} r^3 \text{ -} 9.90 \cdot 10^{\text{-}6} r^2 + 1.01 \cdot 10^{\text{-}3} r \text{-}2.80 \cdot 10^{\text{-}2};\\
&\vdots
\end{aligned}
\tag{2.20}
$$

In this case the minimum observed value of R^2 is 0.9966 for the data rate r =220 Mbps. The goodness of this regression is also confirmed by the relative error observed: in fact the maximum value observed on all rates is 6.8922% still for r =220 Mbps.

If we fix the value of r to 55 Mbps in (2.20), we obtain the following elements for $\boldsymbol{B}$:

$$
B(55) = B_3 = \begin{bmatrix}
0 & 1.6372 & 1.5491 \cdot 10^{\text{-}1} & 3.2931 \cdot 10^{\text{-}3}\\
0 & \text{-}8.1729 \cdot 10^{\text{-}1} & \text{-}7.6972 \cdot 10^{\text{-}2} & \text{-}1.6096 \cdot 10^{\text{-}3}\\
0 & 1.6529 \cdot 10^{\text{-}1} & 1.5315 \cdot 10^{\text{-}2} & 3.1553 \cdot 10^{\text{-}4}\\
0 & \text{-}1.6371 \cdot 10^{\text{-}2} & \text{-}1.4947 \cdot 10^{\text{-}3} & \text{-}3.0432 \cdot 10^{\text{-}5}\\
0 & 7.9158 \cdot 10^{\text{-}4} & 7.1285 \cdot 10^{\text{-}5} & 1.4369 \cdot 10^{\text{-}6}\\
0 & \text{-}1.4952 \cdot 10^{\text{-}5} & \text{-}1.3292 \cdot 10^{\text{-}6} & \text{-}2.6554 \cdot 10^{\text{-}8}
\end{bmatrix}
\tag{2.21}
$$

which, substituted in 2.14, leads to:

$$
\begin{aligned}
&BER(d,p,55) = 10^{\left(\left[B_3 \cdot \langle p \rangle_3^T\right] \cdot \langle d \rangle_5^T\right)}\\
&1m \ < \ d \ \leq \ 15m\,,\\
&-55\ dB \ \leq \ p \ \leq \ -15\ dB
\end{aligned}
\tag{2.22}
$$

Figure 2.14a shows the BER course plotted using (2.22). We can see in Figure 2.14b how the polynomial approximation provided by (2.22) is very good (the maximum relative error committed is only 4.3591%). This trend is also confirmed by the observed value of R^2 that is 0.9993.

For data rate 220 Mbps, still in the CM2 scenario, the coefficients of matrix $\boldsymbol{B}$ take the following values:

$$
B(220) = B_4 = \begin{bmatrix}
0 & 6.5071 \cdot 10^{\text{-}2} & 5.8497 \cdot 10^{\text{-}3} & 1.8940 \cdot 10^{\text{-}4}\\
0 & 3.1655 \cdot 10^{\text{-}2} & 1.7761 \cdot 10^{\text{-}3} & \text{-}2.1415 \cdot 10^{\text{-}5}\\
0 & \text{-}1.3985 \cdot 10^{\text{-}2} & \text{-}1.0170 \cdot 10^{\text{-}3} & \text{-}5.9758 \cdot 10^{\text{-}6}\\
0 & 2.0065 \cdot 10^{\text{-}3} & 1.5368 \cdot 10^{\text{-}4} & 1.3760 \cdot 10^{\text{-}6}\\
0 & \text{-}1.2314 \cdot 10^{\text{-}4} & \text{-}9.6223 \cdot 10^{\text{-}6} & \text{-}9.7543 \cdot 10^{\text{-}8}\\
0 & 2.7661 \cdot 10^{\text{-}6} & 2.1830 \cdot 10^{\text{-}7} & 2.3434 \cdot 10^{\text{-}9}
\end{bmatrix}
\tag{2.23}
$$

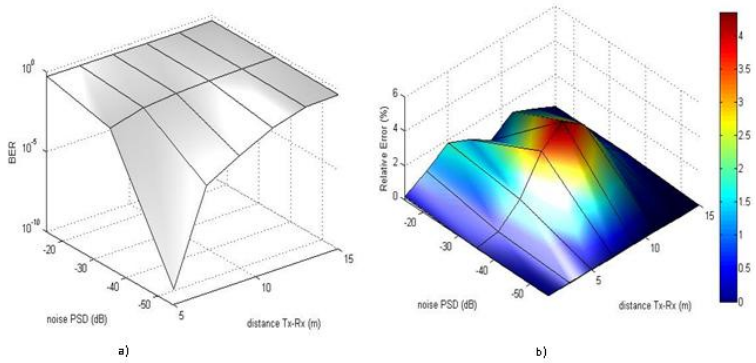

Fig. 2.14. a) BER vs. distance and noise PSD for rate 55 Mbps, CM2 scenario. b) Relative error committed by regression analysis.

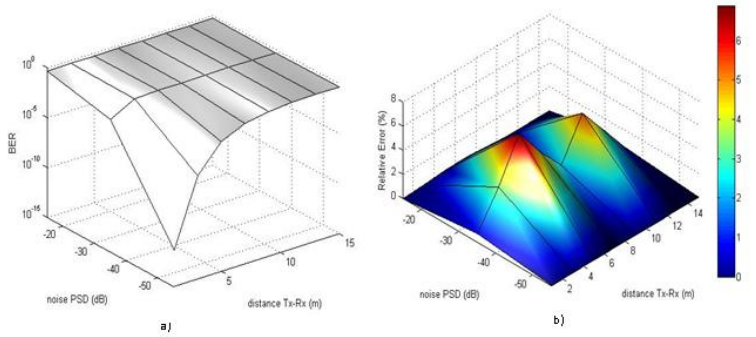

Fig. 2.15. a) BER vs. distance and noise PSD for rate 220 Mbps, CM2 scenario. b) Relative error committed by regression analysis.

If we substitute the previous matrix in (2.14), we obtain the following expression:

$$\begin{array}{l} BER(d,p,220) = 10^{\left(\left[B_4 \cdot \langle p \rangle_3^T\right] \cdot \langle d \rangle_5^T\right)} \\ 1m \ < \ d \ \leq \ 15m \quad , \\ -55\ dB \ \leq p \ \leq \ -15\ dB \end{array} \tag{2.24}$$

In Figure 2.15a we can see BER trend, obtained by (2.24) for data rate 220 Mbps in a CM2 scenario.

In this case, the *determination coefficient* R^2 over the polynomial function is 0.9966, while the relative error committed by the regression approximation, plotted in Figure 2.15b, has a maximum value of 6.8922%.

2.6 Ideal MMSE Receiver Analysis

The regression analysis allows us to obtain a closed formula for the BER, but it has a great limitation: it is valid only in the range in which it has been computed. For this purpose, an alternative way to obtained an expression for the BER is needed. In this section we give an analytic treatment of an ideal MMSE receiver that leads to obtain a closed formula for the BER.

In DS-UWB system, the k_{th} user's transmitted signal can be expressed as:

$$x_k^{\{v\}}(t) = \sum_{i=1}^{M} b(i) \cdot s_k^{\{v\}}(t) \tag{2.25}$$

where M is the packet length, the symbol $\{\cdot\}$ means that the signal $x_k(t)$ is also a function of the data rate v while $b(i)$ is the bipolar representation of bits BPSK modulated by a signature waveform $s_k^{\{v\}}(t)$, so -1 or +1 can be assumed depending on the signaling bits. $s_k^{\{v\}}(t)$ consists of a train of pulses, known as Gaussian UWB monocycles, which are modulated by signature spreading sequence of user k, and depends on the data rate v (in fact, spreading sequence length is related to transmission rate and so to the pulses number, composing $s_k^{\{v\}}(t)$, changes on the basis of v).

If k-th user's signal is transmitted through a multipath channel, characterized by the impulse response $h(t, d)$ defined by (2.2), the relative received signal can be expressed as:

$$y_k^{\{v,d\}}(t) = x_k^{\{v\}}(t) \otimes h(t, d) \tag{2.26}$$

where $\otimes$ is the convolution operator and $\{v, d\}$ denotes that $y_k(t)$ depends also on distance and rate.

The total received signal is then:

$$r^{\{v,d\}}(t) = y_k^{\{v,d\}}(t) + n(t) \tag{2.27}$$

where $n(t)$ is zero-mean AWGN.

The MMSE receiver is composed of a pass-band filter, for noise and out-of-band interferences suppressions, and an adaptive filter, which acts as a correlator [41].

The observation window of the adaptive filter represents the time in which it "examines" the received signal samples, in order to take a decision on the current bit value. Assuming that T is the duration of observation windows, then the i-th window for the i-th bit decision is:

$$(t_0 + (i-1)T_b \ , \ t_0 + (i-1)T_b + T)$$

where T_b is the symbol period.

Without loss of generality, we assume that there is only one transmitting user, that we denote with k, and that there is no interference due to a multiple

channel access. In addition, we can suppose that $T = T_b$, because the i-th observation window contains the most of the energy of the i-th bit and the effects on the next incoming bits are negligible.

If user k, placed at some distance d from receiver, transmits with a data rate v a single positive bit through the channel, it is received as:

$$z_k^{\{v,d\}}(t) = s_k^{\{v\}}(t) \otimes h(t,d) \otimes h_b(t) \tag{2.28}$$

where $h_b(t)$ is the impulse response of the pass-band filter (Figure 2.16).

The number of signal samples in each observation window is given by:

$$N_b = \frac{T_b}{T_s} = \frac{N \cdot L}{T_s}$$

where T_s is the sampling time, N the number of samples with which each impulse is discretized and L is the length of used spreading sequence (that is to say the number of pulses for each symbol).

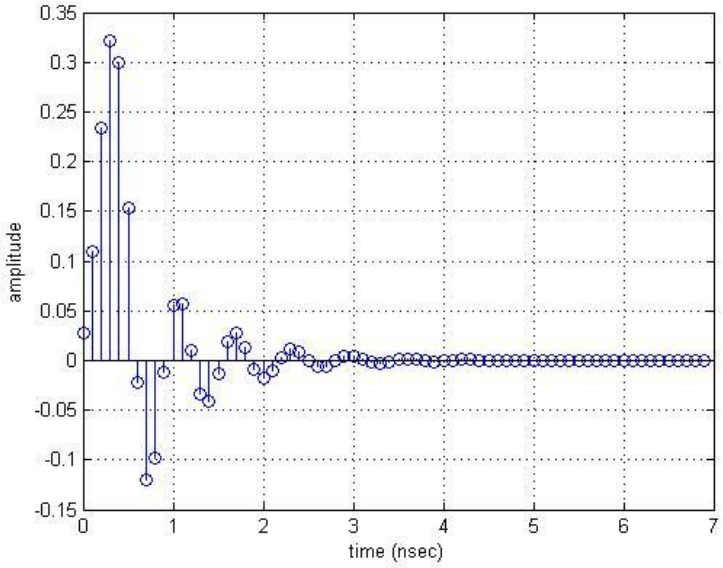

Fig. 2.16. Chebyshev passband filter impulse response.

Referring to [41], we define:

$$\begin{aligned} &j_0 \triangleq \tfrac{t_0}{T_s}\,, \quad \tilde{z}_k^{\{v,d\}}(j) \triangleq z_k^{\{v,d\}}(jT_s)\,, \quad \tilde{r}^{\{v,d\}}(j) \triangleq r_b^{\{v,d\}}(jT_s)\,, \\ &\tilde{n}(j) \triangleq n_b(jT_s) \qquad\qquad j = 1\,,\ 2\,,\ \ldots \end{aligned} \tag{2.29}$$

where t, and therefore j, is set so that i-th observation window contains most of the energy from the bit of user k, the symbols with a "tilde" denote the discrete-time version of the continuous-time signals while $r_b(\cdot)$ and $n_b(\cdot)$ are the bandpass filtered versions of $r(\cdot)$ and $n(\cdot)$

Let us denote the taps vector of the adaptive filter and the received signal in the i-th observation window with:

$$\mathbf{w} \triangleq [w(1) \;\; w(2) \;\; \dots w\,(N_b)]^T \tag{2.30}$$

$$u^{\{v,d\}}(i) \triangleq \left[\tilde{r}^{\{v,d\}}\,(j_0+(i-1)N_b+1) \;\; \dots \;\; \tilde{r}^{\{v,d\}}\,(j_0+(i-1)N_b+N_b)\right]^T \tag{2.31}$$

From (2.28) and (2.29) can be written:

$$u^{\{v,d\}}(i) = b_k(i)\cdot \bar{z}_k^{\{v,d\}}(i) + \bar{n}(i) \tag{2.32}$$

where

$$\bar{n}(i) \triangleq [\tilde{n}\,(j_0+(i-1)N_b+1) \;\; \dots \;\; \tilde{n}\,(j_0+(i-1)N_b+N_b)]^T \tag{2.33}$$

$$\bar{z}_k^{\{v,d\}}(i) \triangleq \left[\tilde{z}_k^{\{v,d\}}\,(j_0+(i-1)N_b+1) \;\; \dots \;\; \tilde{z}_k^{\{v,d\}}\,(j_0+(i-1)N_b+N_b)\right]^T \tag{2.34}$$

According with [41], the optimal tap vector to detect user k's i-th bit is:

$$\tilde{\mathbf{w}} = \left[\bar{z}_k^{\{v,d\}}(i) \;\cdot \bar{z}_k^{\{v,d\}H}(i) + R\right]^{-1} \cdot \bar{z}_k^{\{v,d\}}(i) \tag{2.35}$$

where H denotes the conjugate transpose and R is the covariance matrix of $\bar{n}(i)$:

$$\mathbf{R} \triangleq E\left\{\bar{n}(i)\cdot \bar{n}^H(i)\right\} \tag{2.36}$$

The i-th output of the MMSE filter can be written as:

$$\beta(i) = \tilde{\mathbf{w}}^H u(i) = \tilde{\mathbf{w}}^H \bar{z}_k(i) b_k(i) + e_g(i) \tag{2.37}$$

where $e_g(i)$ is the residual Gaussian noise after pass-band filtering.

Since the pass-band and MMSE filtering are linear operations and $n(t)$ has zero-mean, therefore $e_g(i)$ is a linear combination of $n(t)$ and it is also a approximately zero-mean Gaussian variable. So, the BER can be written as:

$$Pe\,(v,d,2\sigma^2) = Q\left(\sqrt{\frac{\tilde{\mathbf{w}}^H \bar{z}_k^{\{v,d\}}(i)}{\sigma_g^{2\,\{\sigma^2\}}}}\right) \tag{2.38}$$

where σ_g^2 is the variance of $e_g(i)$ and is given by:

$$\sigma_g^2 = \sigma^2 \sum_j |h_{bw}(j)|^2 \tag{2.39}$$

where $2\sigma^2$ is the PSD of the AWGN while $h_{bw}(j)$ is:

$$h_{bw}(j) \stackrel{\Delta}{=} h_b(j) \otimes \tilde{w}(j) \tag{2.40}$$

Equation (2.38) expresses the BER for a DS-UWB system utilizing an ideal MMSE receiver and subject to multipath fading for a given transmission rate, a given distance between transmitter and receiver and a given power level of the background noise. FEC techniques after the MMSE receiver have not been accounted such as in this mathematical formulation. The expression (2.37) gives a lower bound for real MMSE performance (see examples shown in Figure 2.17 for the rate 110 Mbps in the CM2 scenario and with a PSD of -35 dB).

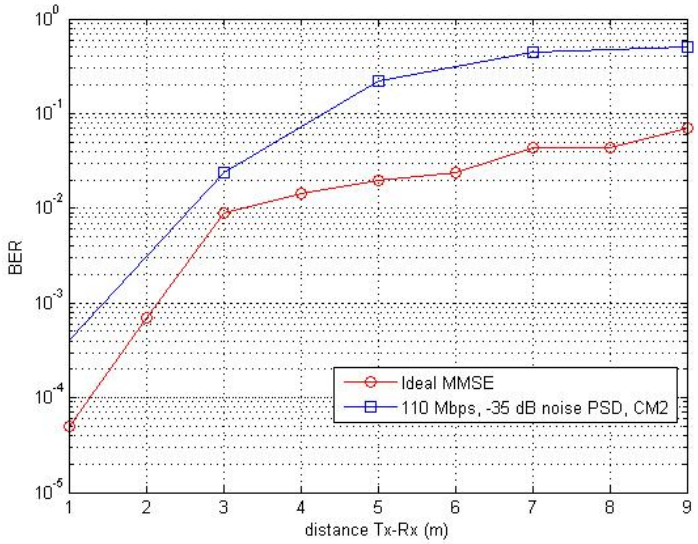

Fig. 2.17. BER analytic and simulated vs. distance for CME scenario, rate 110 Mbps, PSD noise of -35 dB.

2.7 Dynamic Scenario: Mobility User

All previous analysis is based on a static scenario that is the user mobility is not taken into account. The purpose of this brief treatment is to draw

some considerations on the UWB mobility scenario. In order to investigate the effects of users motion in 2-D indoor environments on future networks, we need to model mobility. For this purpose, we use an analytical mobility model in 2-D indoor environments based on model proposed in ([45],[46],[47]). The goal of this work is to analyze the impact of mobility on system performance: in particular we want to underline the effect of impulse response variability on the average BER, so other effects, as Doppler effect, are neglected: we will treat these aspect in our future works. As described in ([45],[46],[47]), we define the following parameters:

- V, motion speed;
- V_{MAX}, maximum speed of the users (in the following we refer it simply as user speed);
- X, distance between two turning points of moving users;
- T, duration of each transmission.

To model mobility, we make the following assumptions:users move on square-shaped building floor (the side floor is set to 10 meters); T is set to 300 seconds for each transmission; speed is uniformly distributed with $[0, V_{MAX}]$ (however a user moves with the speed of V during a transmission); We suppose that a line of sight between receiver and transmitter always exists in each region of the floor for the LOS scenarios, while this is never present for the NLOS scenarios; users move straight line until they change directions, i.e., turn right, left, or back, and then continue to move straight line again (Figure 2.18); when users arrive at the outer wall, they go back to the incoming direction without delay (the point at the outer wall is not regarded as a turning point);direction changes occur according to a Poisson process (that is X is a Poisson process), and the direction selection ratio at the turning point has a probability of 0.4, 0.2, and 0.4 to the left, back, and right, respectively; X is distributed with a mean distance between turning points of 10 m; we suppose that transmitter is fixed in the center of floor and receivers move around it. Further details on this model can be found in ([45],[46],[47]).

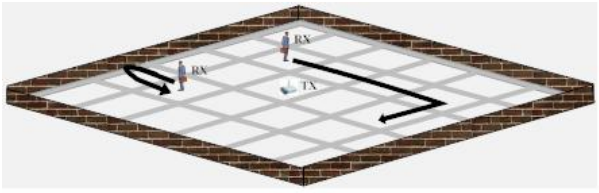

Fig. 2.18. User moving pattern.

Many simulation campaigns have been lead out in order to evaluate the performance of the DS-UWB physical layer for the UWB technology. In the

following simulation results will be analyzed in terms of average BER. In particular, we will show BER limits vs. user speed, that is the speed up to which the BER is less than a specific threshold depending on considered applications (in this paper we analyze voice, data, audio and video applications). Besides, all BER limits operative range must not be intended as absolute numbers, but as average values extracted by a lot of simulations. Furthermore, we show only results for lower (28 and 55 Mbps) and medium (110, 220 and 500 Mbps) data rate in the CM1 and CM2 scenarios. We give the average operative ranges in terms of user speed for four application types under two different scenarios: CM1 (LOS) and CM2 (NLOS). In our analysis, for the BER simulation results assume a target voice BER of 10^{-2}, a target data BER of 10^{-4} (that is the maximum BER bound for application as file transfer), a target audio BER of 10^{-3} (e.g. high resolution audio applications) and a target video BER of 10^{-6}. The channel model employed in this campaign of simulation is has been already described in the Section 2.2. Furthermore, in all our simulations, we add a minimum amount of AWGN in order to provide a medium SNR of 30 dB (we consider this high value because our purpose is only to investigate the effect of multipath fading in presence of mobility). In Figure 2.19 the curves of average BER vs. maximum users speed in a CM1 scenario for 28, 55, 110, 220, 500 Mbps data rates are plotted. We can observe as, only the lower data rates (28 Mbps, 55 Mbps and 110 Mbps) are less sensible to user speed contrarily to other data rates (220 Mbps and 500 Mbps) that are more influenced by mobility. This trend depends on ISI. The mobility further degrades the performance because it varies the impulse response and so it makes the adaptation of receiver to channel condition very difficult.

In Figure 2.20, we show the curve of medium data rate (110, 220 and 500 Mbps) and low data rate (28 and 55 Mbps) under a NLOS multipath scenarios (CM2). Also in this case, it emerges that the lower data rate are lees sensible to the user mobility, even if the absence of a direct component worsens the overall performance. In terms of application oriented average operative range, we can observe as, for example, voice can be supported at 28 Mbps data rate up to a speed of 2.47 m/s in CM1 scenario and up to 2.45 m/s in CM2 scenario, whereas if the data rate is risen to 500, voice applications can be supported respectively up to 0.9 and 0.8 m/s in CM1 and CM2. Other applications operative range are summarized in Table 2.3. We underline that 500 Mbps data rate in the NLOS scenario (CM2) can support only voice applications, so it is not applicable for the others applications.

2.8 Conclusions on Chapter 2

In this Chapter, we analyzed the performance of the DS-UWB physical layer in terms of BER and FER. Simulation results show how the performance, in terms of BER and FER, of the UWB channel, for a high data rate in the case of lower signal-to-noise ratio (noise PSD $\geq -35dB$) degrades for increasing

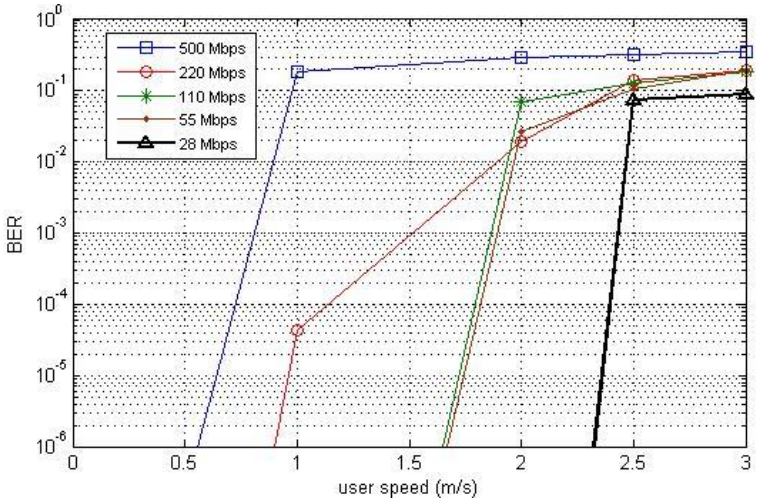

Fig. 2.19. Average BER vs. maximum users speed for CM1 scenario, average SNR -30 dB

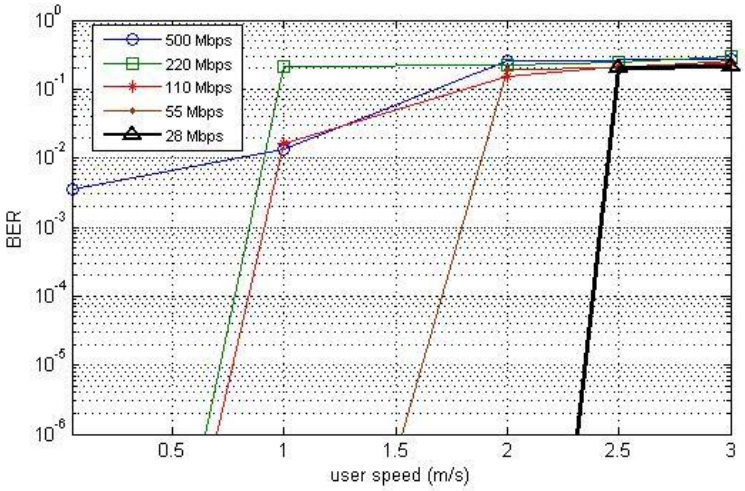

Fig. 2.20. Average BER vs. maximum users speed for CM2 scenario, average SNR -30 dB

Table 2.3. Average applications operative range in m/s.

Voice Applications			**Data Applications**		
Data Rate	**CM1**	**CM2**	**Data Rate**	**CM1**	**CM2**
28 Mbps	**2.47**	**2.45**	**28 Mbps**	**2.4**	**2.38**
55 Mbps	**1.96**	**1.87**	**55 Mbps**	**1.81**	**1.7**
110 Mbps	**1.94**	**1**	**110 Mbps**	**1.8**	**0.84**
220 Mbps	**1.89**	**0.9**	**220 Mbps**	**1.13**	**0.78**
500 Mbps	**0.9**	**0.8**	**500 Mbps**	**0.72**	**NA**
Audio Applications			**Video Applications**		
Data Rate	**CM1**	**CM2**	**Data Rate**	**CM1**	**CM2**
28 Mbps	**2.43**	**2.42**	**28 Mbps**	**2.32**	**2.3**
55 Mbps	**1.89**	**1.8**	**55 Mbps**	**1.67**	**1.55**
110 Mbps	**1.87**	**0.91**	**110 Mbps**	**1.65**	**0.7**
220 Mbps	**1.5**	**0.84**	**220 Mbps**	**0.9**	**0.65**
500 Mbps	**0.8**	**NA**	**500 Mbps**	**0.55**	**NA**

distance (1-15m). In particular, 28Mbps and 55Mbps rates are slightly influenced by transmitter-receiver distance, especially for the CM1 scenario with low noise power level. This is due to the low sensitivity to the inter-symbol interference. On the other hand, higher data rates (mostly rate $\geq 220Mbps$) are more sensitive to the transmitter-receiver distance and they can be supported for a shorter distance (in particular this distance decreases for the CM2 scenario and with very high noise power level). Another contribution is to provide BER analytic expressions for each scenario expressing it as a function of the data rate, noise PSD and distance between transmitter and receiver. In this way, we provide a good tool, usable for future applications, which allows the BER to be obtained directly, solving a three-variables polynomial. Moreover, we provide an analysis on the performance of an ideal MMSE receiver: this treatment allows us to obtained a closed formula for the BER. Finally, we analyze the user mobility in the UWB network: we give BER average limits vs. user speed for the most common user applications (that is voice, data, audio and video applications) in order to provide valid operative range use-

ful to design UWB network taking into account the mobility effects on the applications performance.

3

A Markovian Approach to Model UWB Channel

The classic channel modeling approach models the phenomena of wireless channel through an impulse response and so it can work only at the physical level and is, therefore, not suitable for work at the packet level. This is not a trivial problem, especially if one also wants to investigate the higher levels of ISO/OSI architecture: in fact, in this case, a model describing the trend of wrong packets in time and not the signal corruption at the physical layer is needed. For this purpose, in this work an approach based on Discrete-Time Markov Chain (DTMC) [48],[49] is proposed in order to model the wireless channel. We call this new approach Degradation Level - DTMC (DL-DTMC). In accordance with [50], it can be observed that channel characterization can be captured by a packet error trace, but in contrast to [50] in this analysis the concept of degradation level is introduced: the single packet is not analyzed, but a time window is fixed and the degradation level of the link computing the Packet Error Rate (PER) relative to the specific time window is evaluated. This approach increases the number of states with respect to the simple Gilbert-Elliot (G-E) model [49], but here it is shown that it improves the accuracy of the model: in particular it will be shown that it is convenient to add new states (also increasing the time window duration) to the DTMC until the utility of the last added state is null. Furthermore, a procedure, to obtain a specific model for a given wireless system, data rate, scenario (that LOS, or NLOS) and average noise power level starting from data collected by simulation is described. Starting from the consideration on physical layer and channel dynamics given in the previous chapter, we applied this approach to the UWB system. Many works have already treated UWB channel modeling, however, to the best of our knowledge, all the proposed channel models work at the physical level investigating only some aspects of channel interaction. The degradation level approach is more accurate than the classic G-E model, the 3rd order Markov model and the Markov-based Trace Analysis (MTA) Model as a comparative analysis, based on the occurrence of correctly and wrongly received packets, showed.

3.1 State of Art

Many works have already treated channel modeling using a statistical approach based on the Markov Chain. In [50], the authors proved that trace exhibits stationarity proprieties for small temporal windows and so they propose subdividing the trace in an error free period and lossy period, where this latter process is again modeled as a kth order Markov Chain. Their algorithm, based on the error frame analysis is called MTA. MTA is adequate to capture statistics such as the distribution of wrong packets in the trace, but it is unable to capture 2nd order statistics such as PER or the autocorrelation function of frame error level. This problem is solved in [51]: the authors propose a new model, a simple ON-OFF model, based on a two-state semi-Markov approach in which a particular geometric distribution is employed to capture both first and second order statistics. This approach gives a better performance than MTA, however, it is much more complex. In [52] the authors revised and enhanced the model proposed in [51]: they confirmed the two-state semi-Markov approach but suggested employing a logarithmic distribution for the holding time of each state instead of the geometric distribution. Another important approach is the gap model proposed in [53], in which the authors proved that, under specific conditions, the packet errors can be modeled only as a Markov chain without constant transition probabilities. Instead in [54] the Bipartite model was proposed, which offers a better approximation of error distribution with respect to the above-mentioned approaches but is more complex owing to the many parameters which have to be estimated in order to set the model. In [55], the authors showed that a simple two-state Markov Chain is sufficient to model the packet loss in 802.11b link, in contrast to the GSM system for which more complex models are needed owing to the error characteristics. However, in [55] it is also shown that bit error modeling requires more accuracy and so they proposed a Hierarchical Markov Model (hMM) for these statistics. These latter considerations led us to consider as reference for this analysis the G-E model (that is a simple two-state model) described in [49] and the error analysis presented in [50]. In particular, in accordance with [50], it is observed that channel characterization can be captured by a packet error trace, but in contrast to [50] in this analysis the authors introduce the concept of degradation level: the single packet is not analyzed, but a time window is fixed and the degradation level of that set of packets is evaluated. In [50], as previously mentioned, the authors propose the MTA algorithm: they extend the Bad state into more states if the stationarity property is not satisfied, subdividing the original trace into two segments. They start from the assumption that a time-variant wireless channel, such as GSM channel, does not make the trace stationary and so a decomposition of the original trace is needed to better describe channel behavior. In a non-stationary regime, the MTA algorithm provides a better performance with respect to the traditional G-E and n-th order Markov model, however, no considerations are given on stationary regime: in these conditions the complexity increases due to MTA cannot be

justified, because the MTA and traditional model could have a comparable performance. Instead, this analysis is carried out under stationarity conditions and the number of states is related to the dimensions of the observation window and, in particular, their number is greater if the channel conditions are not perfect or fully degraded (in a fully degraded channel or in a perfect channel typically two states are sufficient to describe channel dynamics). Finally, we underline the main contributions of our proposal:

- We propose a new DTMC channel modeling that is based on the concept of degradation level: a window time is fixed and transition probabilities are computed in accordance with it. Further details can be found in Section 3.2;
- We propose an algorithm to obtain the optimum DL-DTMC model for a given transmission configuration and, furthermore, we give an algorithm to compute an artificial trace starting from the transition probabilities matrix (see, respectively, Section 3.2 and Subsection 3.4.1);
- We compare our model with other models well-known in literature (Gilbert-Elliot model, 3rd order Markov and MTA models) and we show experimentally that our model offers the best performance and is less complex (see Section 3.4 for further details);
- In this paper, we apply our model to a UWB system, but the DL-DTMC approach is a general model that can be extended to other wireless systems such as IEEE 802.11 or IEEE 802.16;
- "To the best of our knowledge, the UWB channel models presented in literature can work only at the bit level, while our model is based on a DTMC approach and therefore works at the packet level (see the "'State of Art"' section and the following section).

3.2 Degradation Level Based DTMC Channel Modeling

In the following, some definitions useful to describe DL-DTMC channel modeling will be given. Afterwards the concept of degradation level and the DL-DTMC channel model will be explained in detail.

3.2.1 DTMC useful definitions

A DTMC is defined as a discrete-time stochastic process assuming discrete values such as process evolution starting from the observation time depending only on the current state [48],[49]. Furthermore, we recall that the transition probability $p_{i,j}$ measures the constant trend to leave the state i and the $\mathbf{P}$ matrix is the collection of these probabilities. Before proceeding with this analysis some useful definitions must be given:

1. Transition probabilities are time-invariant (stationarity property);

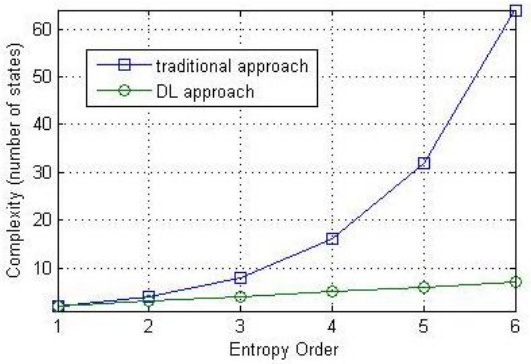

Fig. 3.1. Number of states vs. Entropy order.

2. State $j$is immediately reachable from state i (denoted with $i \rightarrow j$) if $p_{i,j} \neq 0$;
3. A state i is transient if it can immediately reach some state$j$,from which it is impossible to return to state i, in one step that is: $\exists j \in S \ such \ that \ i \rightarrow j \ \ and \ \ not j \rightarrow i$; where S is the state set;
4. *Conditional Entropy* is a measure of the amount of information of an element of the trace knowing the previous history. The lower the conditional entropy the more an observer can predict the state of a variable, knowing the state of the previous variable. The amount of past history necessary to predict the next element of the trace depends on *Entropy Order*: an *i-th entropy order* of "0" indicates that knowing the last i elements of the chain totally predicts the next element on the chain. As described in [50], a higher order of conditional entropy means a more accurate prediction of the next element. On the other hand, a decrease in conditional entropy (and so an increase in entropy order) corresponds to an increase in complexity of the Markov Chain measured in the number of states: in fact, for the traditional Markovian approach an entropy of order i gives a complexity of 2^i states. This means that an exponential law relates the entropy order and the number of states in the traditional approaches such as ([49],[50]). Instead, in this approach the entropy order and the number of states (and so the complexity of the Markov Chain) are related by a linear law because two sequences of length i are considered different if they have a different number of wrong packets: the different position of a wrong packet in the two sequences does not make them distinct. In light of this, in this model an entropy of the *i-th* order gives a complexity of $(i+1)$ states. In particular in Figure 3.1, it is shown how in this model the number of states is a linear function of the entropy order, in contrast to the traditional model in which an exponential law relates the entropy or-

der and number of states. In accordance with [50], the conditional entropy is given by:

$$H_C(i) = -\sum_{\mathbf{x}} \left(p(\mathbf{x}) \cdot \sum_{y \in \{0,1\}} p(y|\,\mathbf{x}) \cdot \log_2 \left(p(y|\,\mathbf{x}) \right) \right) \tag{3.1}$$

where $\mathbf{x}$ is one of 2^i possible sequences of length i or, following this approach, $\mathbf{x}$ is one of $(i+1)$ sequences of length i (recalling that in the degradation level approach two sequences are different if they are a different number of "1"), $p(\mathbf{x})$ is the probability of having the specific sequence $\mathbf{x}$ in the trace, $p(y|\,\mathbf{x})$ is the conditional probability of having the sequence $\mathbf{x}$ followed by y.

5. The standard error [44] is used as a measure of error between two vectors of samples x and y, and defined as:

$$e_{st} = \sqrt{\left(\frac{X+Y}{n_x + n_y - 2} \right) \cdot \left(\frac{1}{n_x} + \frac{1}{n_y} \right)} \tag{3.2}$$

where n_x and n_y are, respectively, the dimension of vectors x and y,whereas X and Y are given by:

$$X = \sum_i^{n_x} x_i^2 - \left[\left(\sum_i^{n_x} x_i \right)^2 \Big/ n_x \right]; \quad Y = \sum_i^{n_x} y_i^2 - \left[\left(\sum_i^{n_y} y_i \right)^2 \Big/ n_y \right] \tag{3.3}$$

6. The mean state sojourn times must follow an exponential law.
7. The stationarity property of the trace is verified through the Reverse Arrangements Test [44]. The test is composed of the following steps:
   - divide the trace in N equal time intervals where the data in each interval may be considered independent (we choose an interval composed of 200 packets, however the result of the stationarity test is relatively affected by this choice);
   - the mean square for each interval is computed in order to obtain a time sequence such as:

$$\overline{z_1^2}, \overline{z_2^2}, \overline{z_3^2}, \ldots, \overline{z_N^2}$$

   - the previous sequence is analyzed for the presence of underlying trends using the Reverse Arrangements Test. The total number of reverse arrangements is defined as:

$$A = \sum_{i=1}^{N-1} A_i \tag{3.4}$$

where A_i is given by:

$$A_i = \sum_{j=i+1}^{N} f_{i,j} \tag{3.5}$$

with $f_{i,j}$ defined as follows.

$$f_{i,j} = \begin{cases} 1 \;\; if\, \overline{z_i^2} > \overline{z_j^2} \\ 0 \; otherwise \end{cases} \tag{3.6}$$

- The trace satisfies the stationarity property if the variable A is a random variable and hence, the hypothesis that A is a random variable at a certain percentage level of significance (in this work, a confidence interval of 5% is used), can be accepted if A falls in an interval extrapolated from the table shown in [44].

Therefore, it can be affirmed that a generic stochastic process is a DTMC if it satisfies the stationarity property (that is, transition probabilities are time-invariant), the mean state sojourn times are exponentially distributed and the number of states is finite [49], [50]. Finally, it is observed that the transition probabilities are related to the specific wireless transmission system, to the scenario, to the specific data rate and mostly to the noise level of the channel: it means that their values can vary in a wide range of probabilities (if one considers a simple example of a two-state model the transition probabilities vary from 0 to 1 or vice versa in accordance with the perfect channel degenerate case and totally degraded channel degenerate case). The scenario in which the average PER is zero can be ascribed to the best degenerate case, that is, the trace is composed only of the "Good" state. In this particular case, the process sojourns always in the "Good" state (correctly received packet) and the probability that the process is in the state "0" at the time t_n if at the time t_{n-1} it was in the state "0" is 1. Other probabilities are listed in the following:

$$\mathbf{P}_{best} = \begin{bmatrix} 1 & 0 \\ 1 & 0 \end{bmatrix} \tag{3.7}$$

The dual degenerate case is the worst case, corresponding to the scenario in which the average PER tends to 1. Furthermore, the process always sojourns in the "Bad" state (wrongly received packet), so the probability that the process is in state "1" at the time t_n if at the time t_{n-1} it was in state "1" is 1. In particular, the following values of $\boldsymbol{P}$ are obtained:

$$\mathbf{P}_{wrong} = \begin{bmatrix} 0 & 1 \\ 0 & 1 \end{bmatrix} \tag{3.8}$$

In general, it is observed that the state transition probabilities can be expressed as a function of the noise assuming values between 0 and 1 or vice versa. This trend can be better observed in Figure 3.2, where $p_{0,0}$ and $p_{1,1}$

probabilities are plotted as a function of different thresholds of noise power. Therefore, it is useful to apply the degradation level concept to error trace analysis only in the middle region included in the two degenerate cases (that is, in a specific interval of noise power level) because in these conditions more states are needed to better describe the channel dynamics, whereas in the other cases only two states are sufficient.

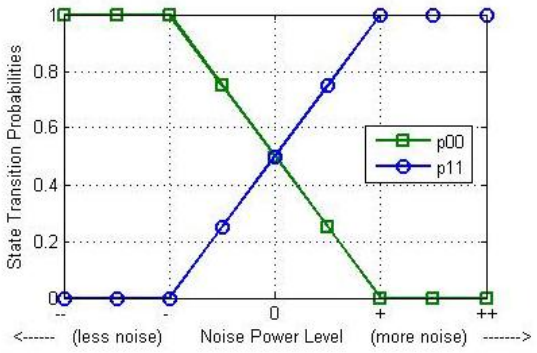

Fig. 3.2. State transition probabilities vs. noise power level.

3.2.2 DL-DTMC model description

Now, we can explain the concept of Degradation Level. In accordance with [50], it is observed that wireless channel characterization can be captured by a packet error trace, where, in this scenario, a packet is a sequence of bits. In this work, a packet is correctly received if no wrong bits are detected and consequently a packet is not correct if one or more bits are erroneously received in the sequence. Thus, the trace is a sequence containing information about whether a particular packet was transmitted correctly. In [50], the authors considered only two states, the *Bad* state and the *Good* state, even if they extend the Bad state into more states if the stationarity property is not satisfied. In contrast to [50], in this analysis the concept of degradation level is introduced: the single packet is not analyzed, but a time window is fixed (consisting in a given number of packets) and the degradation level of the link computing the PER relative to the specific window is evaluated. Repeating this operation recursively for all traces, a new trace can be created (called '*windowed trace*') in which each state represents a specific level of degradation. It should be stressed how the size of time window, denoted with w, influences the transition probabilities and so the Markov Chain evolution (we recall that if w is set to 1 then DL-DTMC model degenerates into the G-E model).

Another important step is to determine the degradation level number, that is the states number, and so the degradation thresholds PER associated with the states: on the basis of these thresholds, the association of the current observed time window to a specific state can be established (e.g. considering a lower degradation level with a threshold PER of 10%, if in the current window a relative PER less than 10% is computed then this window is associated to a lower degradation state). In this work, our approach is to set the states number $|S|$ to w+1: in this way, discrete values of relative PER can be obtained. This simple approach is very efficient because it allows the degradation level to be tied (and so the state representing a specific degradation of the wireless channel) directly to the number of wrong packets in the considered observation window. This concept can be expressed by following expression:

$$\frac{i \ \ wrong \ packet}{w} \ \rightarrow \ PER_{REL} = \frac{i}{w} \ \rightarrow \ \text{we are in the "}i\text{"}\, state \tag{3.9}$$

In order to better explain this proposed model, Figure 3.3 shows the association between the degradation level of an observation window and the state number. For example, the "0" state (that is, the no degradation state) is characterized by a null relative PER meaning that in the observed window no packets are wrongly received. Instead the "w" state is characterized by a relative PER of 100% because in the observed window all packets are wrongly received.

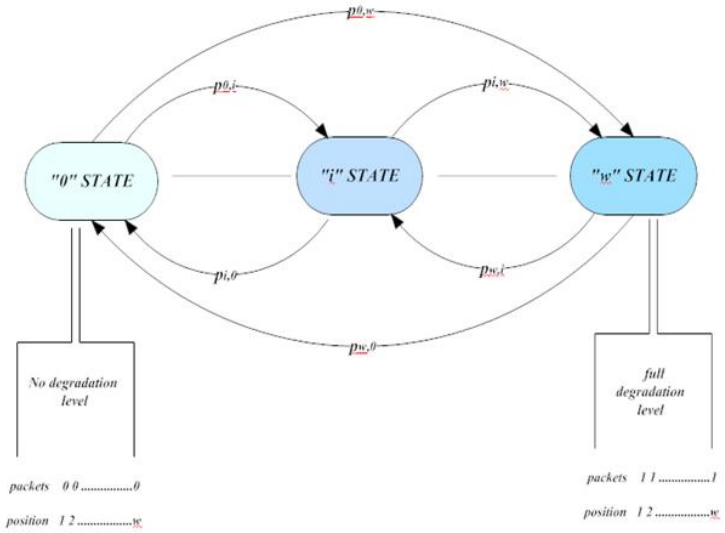

Fig. 3.3. Relation between degradation level and state number.

Moreover, the choice of the window size and the number of states related to it are also an important issue. For this purpose, the concept of *State Utility* (SU) was introduced. For a generic state i, we define a probability vector as follows:

$$\mathbf{V} = [\, v_1 \; v_2 \,] \tag{3.10}$$

where v_1 is the probability to have the i state in the trace (that is the probability to have the sequence of packets corresponding to i state in the trace). In particular, v_1 can be obtained as:

$$v_1 = \frac{O_i}{N_{sequence}} \tag{3.11}$$

where O_i is the number of occurrences of i state, whereas $N_{sequence}$ is the total number of sequences in the trace. Instead, $v_2$is the probability of having a sequence different from i state in the trace:

$$v_2 = \sum_{\substack{j=1 \\ j \neq i}}^{n} p_j = \sum_{\substack{j=1 \\ j \neq i}}^{n} \frac{O_j}{N_{sequence}} = 1 - v_1 \tag{3.12}$$

where n is the number of states. This probability is equal to the sum of probabilities of having the "j" state in the trace for each state $j{\neq}i$. Furthermore, from the definition of $\boldsymbol{V}$, we also have $v_2 = 1 - v_1$ (we recall that $\boldsymbol{V}$ is a stochastic vector). The SU is defined as the *Entropy* $H(v)$ of stochastic vector $\boldsymbol{V}$. The *Entropy* is a measure of uncertainty that is also the potential information which can be extrapolated from an experiment: thus it is zero if the event is completely predictable (it is known a priori) and is maximized when the next event is totally random [44]. This concept can be expressed in this way:

$$\begin{aligned} SU_i = H(v) = h(v) &= -\sum_{k=1}^{|\mathbf{V}|} [v_k \cdot \log_2 (v_k)] = \\ &= -v_1 \cdot \log_2 (v_1) - v_2 \cdot \log_2 (v_2) = \\ &= -v_1 \cdot \log_2 (v_1) - (1 - v_1) \cdot \log_2 (1 - v_1) \end{aligned} \tag{3.13}$$

where SU_i is the utility of $i$state.Moreover, it is assumed that $0 \cdot \log 0 = 0$ (in fact we have $\lim_{x \to 0} (x \cdot \log x) = 0$). SU is also an *Entropy* function: it is a symmetric and concave function assuming a value between 0 and 1 where the minimum values correspond to the deterministic or degenerate probabilities and the maximum value to the uniform probability. It is useful to add a state to the Markov Chain if the SU is greater than zero for all states of the new model obtained with the addition of a new state. In fact, if SU_i=0 then either the probability of having a sequence corresponding to the "i" state is null and "i" is never reachable (that is for the state i the transient property is verified

for each considered states $j \in S$) or this probability is 1 and then the sequence is always present; but this last case also means that all remaining states are never reachable. In both cases the addition of the new state is useless because it leads to transient states or, in terms of *Entropy*, it does not "produce" further potential information useful for the channel prediction (it also means that the new added state does not improve the model).

However, the addition of new states increases the complexity of the model, so it may be necessary to stop the modeling before SU is equal to zero for a state of the chain. For this purpose, similarly to [56], we also introduce an estimator $\hat{k}(\cdot)$ of the DL-DTMC order k defined as follows:

$$\hat{k}\left(\mathbf{x}\right) = \min_{0 \le k \le k_0} \left\{ k \,|\; H_c\left(k\right) - H_c\left(K_0\right) \le \varepsilon_n \right\} \tag{3.14}$$

where $\mathbf{x}$ is one of $(k+1)$ sequences of length k, $H_c\left(\cdot\right)$ is the *Conditional Entropy* defined by (1), K_0 is an upper bound order assumed as reference (we set K_0=19 because maintaining the history for 20 states yields a reasonable level of implementation and processing complexity), whereas ε_n is a threshold given by [56]:

$$\varepsilon_n = \left[\left(K_0 + 1\right) + \delta\right] \cdot \frac{\log_2 N_{samples}}{N_{samples}} \tag{3.15}$$

where $N_{samples}$ is the number of samples of the trace and δ is a constant. In this work, we set $N_{samples}$=10000 and, as suggested in [56], δ=2.

Now, combining (3.13) and (3.14), we obtain the order k to use for our channel modeling:

$$\hat{k}'\left(\mathbf{x}\right) = \min_{0 \le k \le k_0} \left\{ k \;\middle|\; \begin{array}{l} \left[H_c\left(k\right) - H_c\left(K_0\right) \le \varepsilon_n\right] \;\vee \\ \left[\begin{array}{l} \exists\; i \;\in A \;\text{ so that } SU_i = 0, \text{ where } I \\ \text{is the state set of the } (k+1) \text{ order model} \end{array}\right] \end{array} \right\} \tag{3.16}$$

Starting from (3.16), the procedure, to model a DL-DTMC, is provided. Before proceeding with the algorithm, the stationarity property of the process should be evaluated. The stationarity property was verified using the Reverse Arrangements Test previously described [44]. If the trace passes the stationarity test, proceed with the following steps:

If the trace passes the stationarity test, proceed with the following steps:

- Set $w = 0$;
- Set $\boldsymbol{P}$=[ ]; ([ ] denotes the null matrix)
- Repeat
  - $w = w$+1;
  - $\boldsymbol{P}_{prev} = \boldsymbol{P}$;(it is intended as a matrix assignment)
  - $|S| = w + 1$;
  - Create a windowed trace with size of time window set to w applying (3.10);

– Compute the $p_{i,j}$, probability of $\boldsymbol{P}$ applying the following formulas:

$$p_{i,j} = \frac{T_{i,j}}{N_i} \quad j = 0, 1, \ldots, w \quad i \neq j \tag{3.17}$$

where $T_{i,j}$ is the number of transitions from i state to a generic j state, while N_i is the number of i state;

– From the stochastic property of matrix $\boldsymbol{P}$, we compute

$$p_{i,i} = 1 - \sum_{\substack{j=0 \\ j \neq i}}^{w} p_{i,j} \tag{3.18}$$

– Verify the distribution of the state sojourn time using the *Kolmogorov-Smirnov* (K-S) test and set *B=false* if at least one test fails;

- Until (3.16) is verified or *B=false;*
- Set $\boldsymbol{P}$=$\boldsymbol{P}_{prev}$;(it is intended as a matrix assignment).

The modeling procedure is now completed because the Markov chain can be completely determined by matrix $\boldsymbol{P}$ and by distributions of state sojourn time. Owing to lack of space, in this treatment our Markov chain modeling is shown only for some specific configuration and it is compared with the G-E model, MTA and 3^{rd} order Markov model [49],[50] in order to show that this approach better describes the real channel dynamic, that is, it better approximates the original traces obtained by empirical data.

3.3 A Case Study: the UWB Channel Modeling

This channel modeling focuses on the DS-UWB physical layer. In order to collect simulation data to carry out a trace analysis a physical simulator based on Matlab has been developed. In the following, we show some examples of modeling and a comparative analysis between our model and some models known in the literature.

3.3.1 Examples of DL-DTMC modeling for UWB system

In the following some examples will be shown for different data rates, levels of noise and scenarios described in [30] in order to better explain the procedure for creating a DTMC model based on the degradation level concept. However, the soundness of our approach is general and independent of considered specific data rate, scenario or noise level as an extensive analysis, carried out for this work but not shown due to limited space, shows.

In the first example, the data rate is set to 28 Mbps and the CM4 scenario is considered with an average power level of -30 dB. The goal is to show how the DTMC characteristics vary by increasing the length of the observation

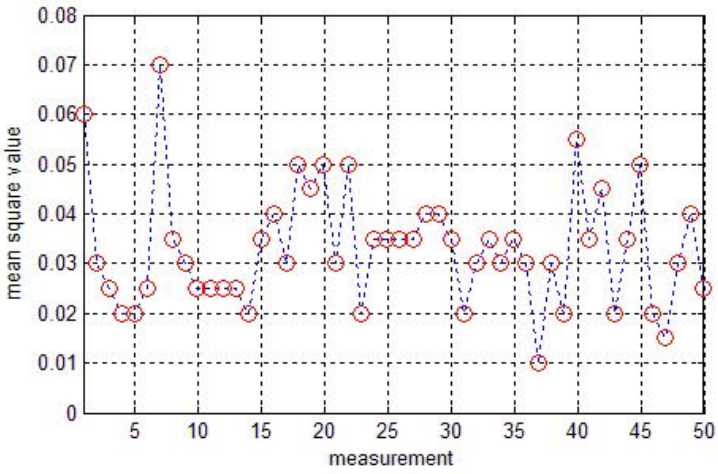

Fig. 3.4. Mean square values computed for each time interval for 28 Mbps data rate in CM4 scenario with a mean power noise of -30 dB.

window (and so the number of states), in particular it can be observed that it is convenient to add further states to the chain, until the SU is not null for all states of the chain: generally this condition is verified until the new added state satisfies the transient property for all remaining states. Remember that it means that this state is a state never reachable in the chain, so the transition probabilities from each state of the chain to this state are null. Naturally, in accordance with (3.16) the second step condition is verified when (3.14) is satisfied or the K_0 DL-DMTC order upper bound is reached. The first step is to evaluate the stationarity property of the original trace using the Reverse Arrangements Test. The mean square value does not present any underlying trend, as is also confirmed by total reverse arrangement values falling in the interval expected (see Figure 3.4). Hence, after having verified the stationarity property, one can proceed to create the windowed trace and to compute state transition probabilities for different lengths. The degenerate case (that is w=1) is omitted, because it is equivalent to the G-E model (two states model), so the analysis starts from three states model (in which the length of the window is set to 2). w_2 denotes this case and in particular is obtained:

$$\mathbf{P}_{\mathbf{w}_2} = \begin{bmatrix} 0.9743 & 0.0234 & 0.0023 \\ 0.8 & 0.2 & 0 \\ 0.6 & 0.4 & 0 \end{bmatrix} \tag{3.19}$$

while for the four states model, with w=3, (indicated with w_3) we have:

$$\mathbf{P}_{\mathbf{w}_3} = \begin{bmatrix} 0.9088 & 0.0846 & 0.0063 & 0.0003 \\ 0.9018 & 0.0947 & 0.0035 & 0 \\ 0.8571 & 0.0952 & 0.0476 & 0 \\ 1 & 0 & 0 & 0 \end{bmatrix} \tag{3.20}$$

Finally w is fixed to 4 and the five states DTMC (denoted with w_4) are modeled obtaining the following matrix:

$$\mathbf{P}_{\mathbf{w}_4} = \begin{bmatrix} 0.8823 & 0.1068 & 0.01 & 0.0009 & 0 \\ 0.8571 & 0.1319 & 0.0073 & 0.0037 & 0 \\ 0.9167 & 0.0833 & 0 & 0 & 0 \\ 1 & 0 & 0 & 0 & 0 \\ 1 & 0 & 0 & 0 & 0 \end{bmatrix} \tag{3.21}$$

It can be seen how, in the w_4 model, for the "4" state, the transient property is verified for each considered state, because it is impossible to reach it from the other states: in fact, all probabilities $p_{i,4}$ are null and therefore the state utility SU is zero for the state "4". This means that the new state added to the chain does not improve the efficiency of the model (no further potential information is "produced"), so in this case the best model is the four-state DTMC. This trend is graphically confirmed by Figure 3.5, where the occurrences of correctly received packets in the original trace and in the artificial traces (for further details on the generation of artificial trace see the next section) are compared: it can be seen how the efficiency of the models rises with the increase in the number of states until the new added state has an utility of zero. In this last case the efficiency of the model degrades with respect to the w_3 model, so it can be stated that for this configuration the best model is the four-state DTMC.

This trend is also confirmed by standard error committed by the 4 states model with respect to the correct packet distribution of empirical data (0.4648), which is less than the standard errors committed by 3 and 5 states model respectively of 0.4986 and 0.8978. Chosen the w_3 model, the next test is to analyze the states sojourn time. Applying the K-S test, it is verified that all states sojourn time are effectively exponentially distributed. In particular, for the "0" state in the case of w_3 model it is obtained that the exponential distribution better fitting experimental data distribution, that is, the distribution minimizing standard error [12], is an exponential with μ=11.1821 introducing a standard error of 0.2149. Figure 3.6 shows the "0" states sojourn time distributions and its approximation exponential distributions for w_3.

Finally, Figure 3.7 shows the conditional entropy as a function of entropy order for the traditional approach and for this approach: it can be seen how for the chosen entropy order, that is, 4 for this configuration, this model gives an entropy value of 0.0139, contrarily to the traditional model giving a value of 0.0137. Therefore this model presents a worsening of entropy of 1.44% with respect to the traditional approach, but on the other hand, the degradation level approach improves the complexity of the model: in fact, if the entropy

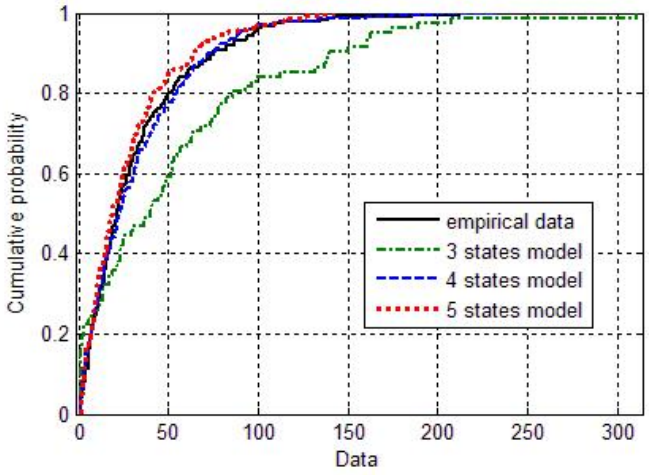

Fig. 3.5. Occurrences of correct packets in original trace and in the artificial traces for data rate 28 Mbps in CM4 scenario, mean power noise of -30 dB.

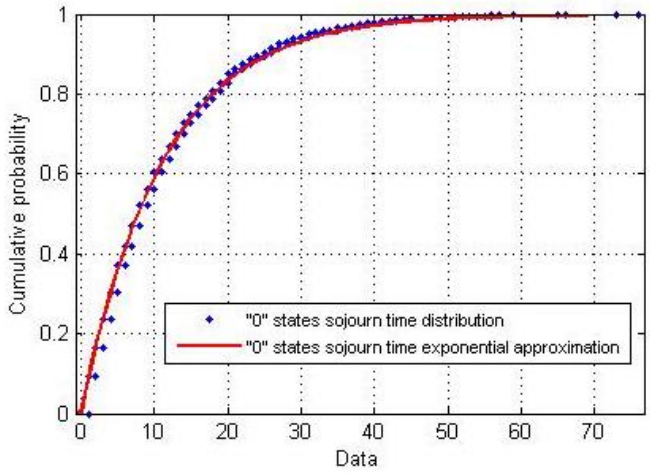

Fig. 3.6. "0" state sojourn time distributions and its approximation exponential distribution for 28 Mbps data rate in CM4 scenario, mean noise power of -30 dB.

order is set to 4, this approach requires 5 states while the traditional approach requires 16 states, so in this case a complexity reduction of 68.75% is obtained.

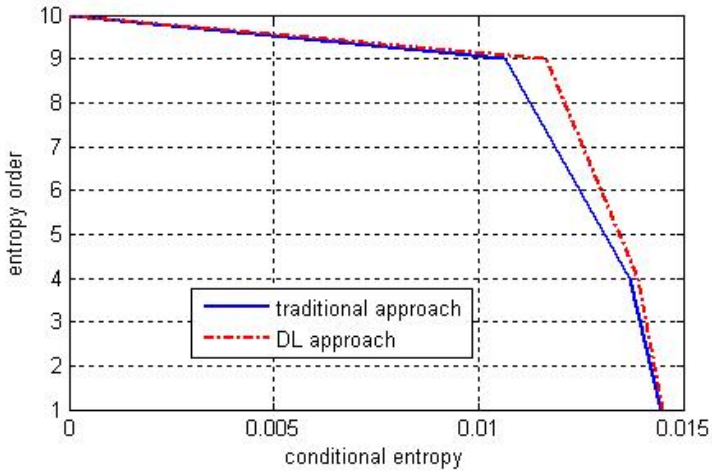

Fig. 3.7. Conditional entropy vs. order of entropy for our approach and traditional approach for the rate 28 Mbps in the CM4 scenario, mean noise power of -30 dB.

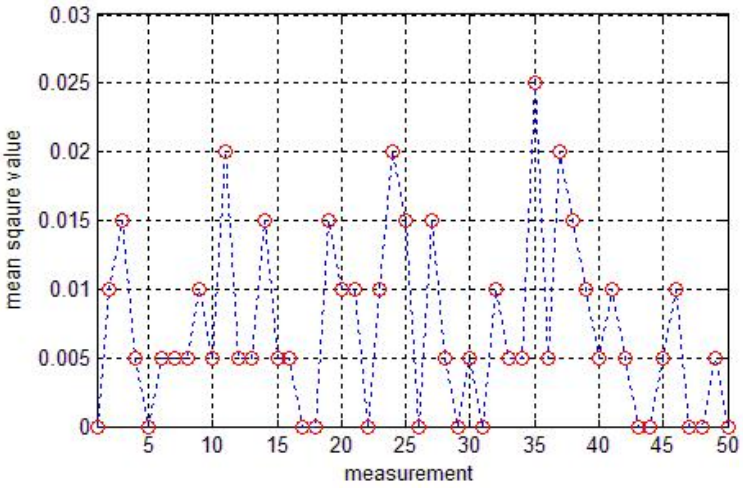

Fig. 3.8. Mean square values computed for each time interval for 55 Mbps data rate in CM1 scenario with a mean power noise of -30 dB.

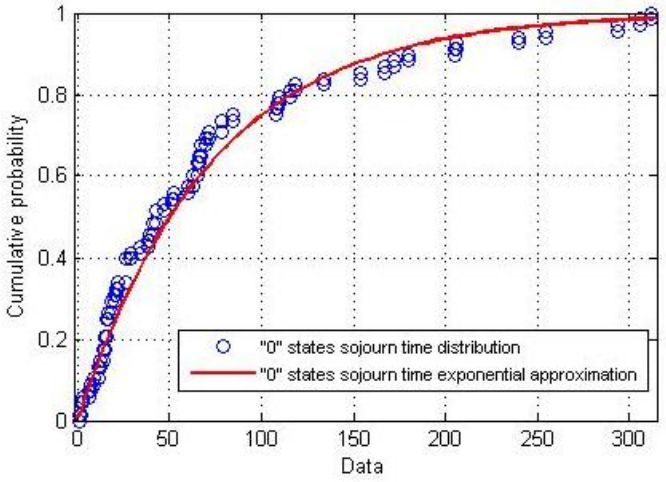

Fig. 3.9. "0" state sojourn time distributions and its approximation exponential distribution for 55 Mbps data rate in CM1 scenario, mean noise power of -30 dB.

In the second considered configuration, a 55 Mbps data rate was employed for the transmission. Furthermore, a mean noise power of -30 dB and the CM1 multipath scenario were assumed. Applying the stationarity test described in the previous section, it was effectively verified that also the trace of this configuration is stationary. This is also confirmed by Figure 3.8, where the mean square values do not show any particular trend. Also in this case, G-E statistics were omitted, while a 3 degradation levels model (that is a window length of 2) was considered denoted with w_2, because it better fits the original trace. The positive results of Runs Test permit one to proceed with the computing of states transition probability.

In particular, is obtained:

$$\mathbf{P}_{\mathbf{w_2}} = \begin{bmatrix} 0.9864 & 0.0132 & 0.0004 \\ 0.9701 & 0.0299 & 0 \\ 1 & 0 & 0 \end{bmatrix} \tag{3.22}$$

Finally, through the K-S test, it is verified that also for this configuration all the states sojourn times are effectively exponentially distributed. In particular, for the "0" state the exponential distribution minimizing standard error is an exponential with μ=72.5147 introducing a standard error of 0.72. In Figure 3.9 the "0" states sojourn time distributions of w_2 and its approximation exponential distribution for the second considered configuration are shown.

The third example analyzes 110 Mbps data rate in the CM2 scenario with an average noise power level of -45 dB. Also in this case, the algorithm proposed in section 4.3 is applied in order to compute the best model fitting

the channel dynamic. As the first step, the random propriety of the trace was tested through Reverse Arrangements test, and only after a positive result, proved also by the mean square values plotted in Figure 3.10, then the analysis was undertaken. It can be observed that, for this configuration, the best fitting model is again the three states model described by the following transition probabilities matrix:

$$\mathbf{P}_{\mathbf{w}_2} = \begin{bmatrix} 0.9964 & 0.0034 & 0.0002 \\ 1 & 0 & 0 \\ 1 & 0 & 0 \end{bmatrix} \tag{3.23}$$

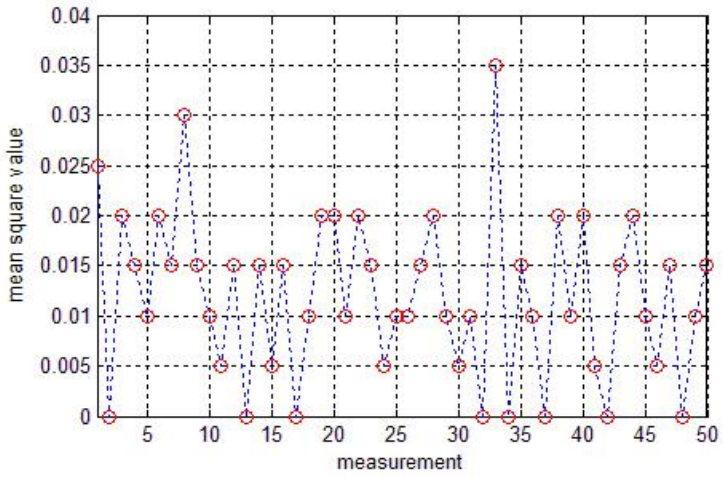

Fig. 3.10. Mean square values computed for each time interval for 110 Mbps data rate in CM2 scenario with a mean power noise of -45 dB.

In order to complete the analysis, through K-S test, it was verified that all the states sojourn times are effectively exponentially distributed. For example, for the "0" state, the exponential distribution minimizing standard error is an exponential with μ=262.211 committing a standard error of 0.6646. Figure 3.11 shows the "0" states sojourn time distributions for the three states model and its approximation exponential distribution.

Considering a 220 Mbps data rate in CM4 scenario with an average noise power level of -35 dB, it can be observed how the stationarity test returns a positive result (this is also confirmed by mean square values shown in Figure 3.12) and the best fitting model is a three states model whose transition probabilities matrix is the following:

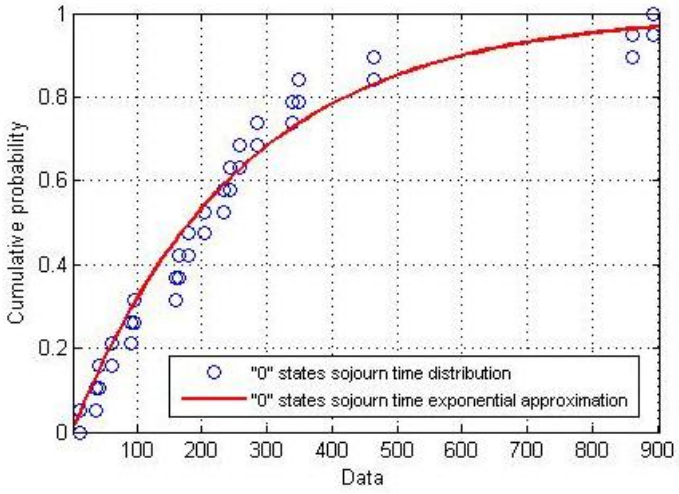

Fig. 3.11. "0" state sojourn time distributions and its approximation exponential distribution for 110 Mbps data rate in CM2 scenario, mean noise power of -45 dB.

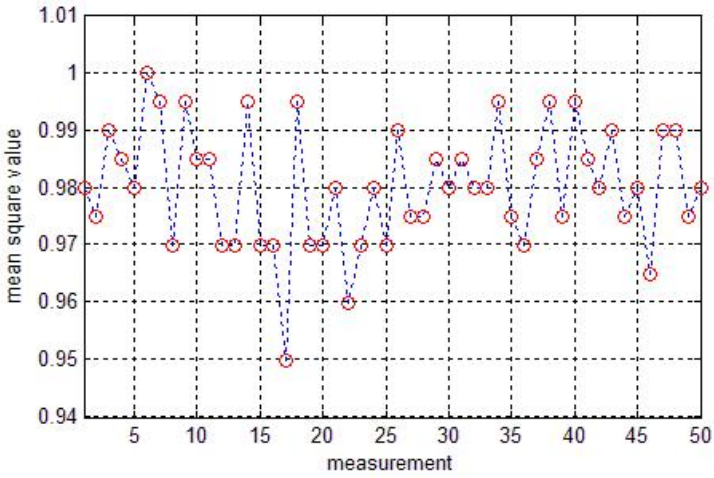

Fig. 3.12. Mean square values computed for each time interval for 220 Mbps data rate in CM4 scenario with a mean power noise of -35 dB.

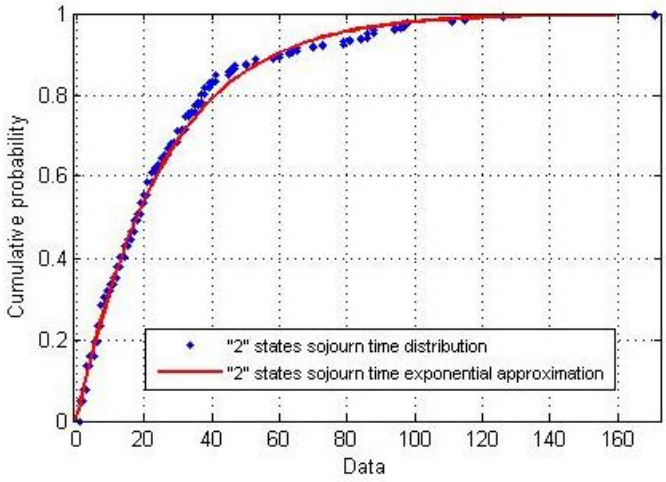

Fig. 3.13. "2" state sojourn time distributions and its approximation exponential distribution for 220 Mbps data rate in CM4 scenario, mean noise power of -35 dB.

$$\mathbf{P}_{\mathbf{w}_2} = \begin{bmatrix} 0 & 0 & 1 \\ 0 & 0.0464 & 0.9536 \\ 0.0004 & 0.0383 & 0.9613 \end{bmatrix} \tag{3.24}$$

The K-S test, applied to all the states sojourn times, confirms their exponential distribution: in particular, in Figure 3.13 the distribution of "2" state sojourn time and its exponential approximation can be seen. In this case the best fitting exponential distribution is characterized by a μ=25.6898 with a standard error of 0.4697.

The fifth example regards 500 Mbps data rate in CM2 scenario with a mean noise power of -50 dB. After to have stationarity propriety verified, the best model is a six states model is characterized by the following probabilities:

$$\mathbf{P}_{\mathbf{w}_5} = \begin{bmatrix} 0 & 0 & 0 & 0 & 1 & 0 \\ 0 & 0 & 0.05 & 0.15 & 0.3 & 0.5 \\ 0 & 0.027 & 0.0721 & 0.1802 & 0.2613 & 0.4595 \\ 0.0033 & 0.0065 & 0.0489 & 0.1694 & 0.3648 & 0.4072 \\ 0 & 0.01 & 0.0601 & 0.1402 & 0.3834 & 0.4063 \\ 0 & 0.0093 & 0.0522 & 0.1555 & 0.3283 & 0.4548 \end{bmatrix} \tag{3.25}$$

All the states sojourn times are exponentially distributed as K-S test confirms. In particular, the best fitting distribution for "5" state sojourn time is an exponential with μ=1.834 committing a standard error of 0.0846. In Figure 3.14 the curves of "5" state sojourn time distributions and its exponential distribution are plotted.

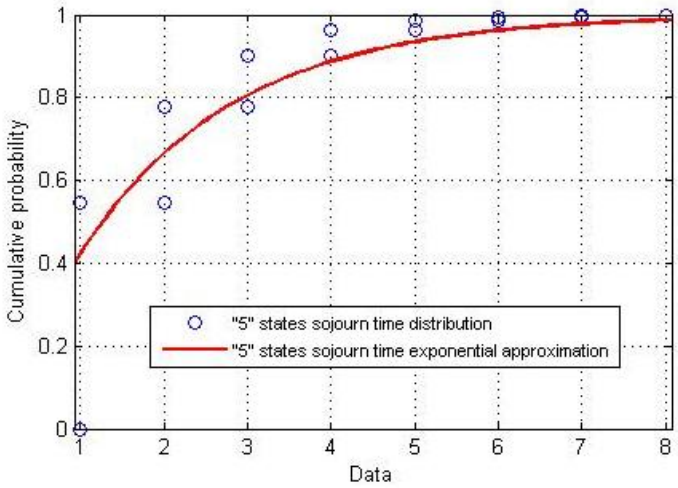

Fig. 3.14. "5" state sojourn time distributions and its approximation exponential distribution for 500 Mbps data rate in CM2 scenario, mean noise power of -50 dB.

In the sixth considered configuration, a 660 Mbps data rate was employed for the transmission. Moreover, a mean noise power of -45 dB and the CM3 multipath scenario were assumed. As for the previous examples, also for this case the G-E statistics were omitted and a four states DL-DTMC model was considered, because it is the best fitting model (in fact, in the five states model there is a transient state). The transition probabilities matrix is given by:

$$\mathbf{P}_{\mathbf{w}_3} = \begin{bmatrix} 0 & 0 & 1 & 0 \\ 0 & 0 & 0.1304 & 0.8696 \\ 0 & 0.0043 & 0.1223 & 0.8734 \\ 0.0004 & 0.0074 & 0.1421 & 0.8502 \end{bmatrix} \tag{3.26}$$

Finally, through the K-S test, it was verified that also for this configuration all states sojourn time are effectively exponentially distributed. In particular, for the "3" state the exponential distribution minimizing standard error is an exponential with μ=6.65808 committing a standard error of 0.3222. Figure 3.15, depicts the "3" states sojourn time distributions and its approximation exponential distribution for this configuration.

The second to last configuration considers a data rate of 1000 Mbps, an average level noise power of -60 dB and a CM2 multipath fading scenario. The passing of Reverse Arrangements tests allow the computation of the transition probabilities: in particular, it was found that, for this case, the model best fitting channel dynamic is a three states DL-DTMC model characterized by:

$$\mathbf{P}_{\mathbf{w}_2} = \begin{bmatrix} 0 & 0.2222 & 0.7778 \\ 0 & 0.2424 & 0.7576 \\ 0.0356 & 0.2133 & 0.7511 \end{bmatrix} \tag{3.27}$$

Statistics regarding the G-E model and other models are omitted and sojourn time distribution of model described by (3.27) was next directly analyzed. The K-S tests confirm that all the sojourn time distributions follow an exponential law. Specifically, for "2" state sojourn time the exponential distribution minimizing standard error is a law with μ=3.94737 introducing an error of 0.52842. This last exponential distribution and "2" state sojourn time distribution are shown in Figure 3.16.

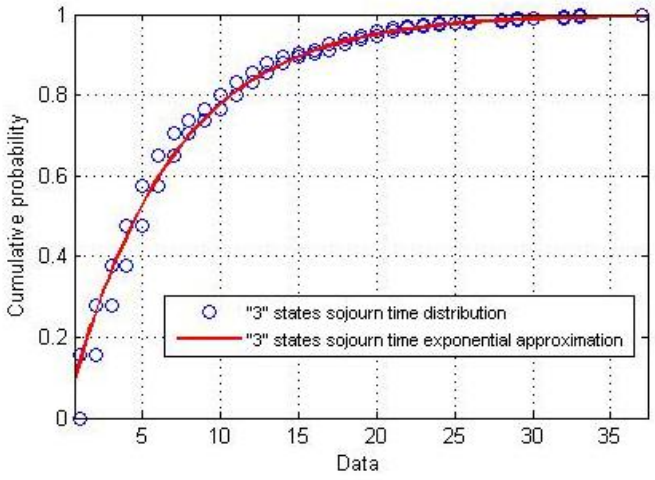

Fig. 3.15. "3" state sojourn time distributions and its approximation exponential distribution for 660 Mbps data rate in CM3 scenario, mean noise power of -45 dB.

Finally, the last considered scenario regards 1320 Mbps data rate in the CM3 scenario with a level of mean noise power set to -50 dB. In this specific case, it can be noted how the DL-DTMC approach is not recommended because the three states model already introduces a transient state: in fact, the noise power level is such that it is not in the DL-DTMC applicability region, that is, the trace is mainly composed of wrong packets (PER>98%) and so only two states can be sufficient to described the dynamics of the channel. In the following respectively the transition probabilities matrixes for the three states DL-DTMC model and G-E model are shown:

$$\mathbf{P}_{\mathbf{w}_2} = \begin{bmatrix} 0 & 0 & 1 \\ 0 & 0.3125 & 0.6875 \\ 0 & 0.0061 & 0.9939 \end{bmatrix} \tag{3.28}$$

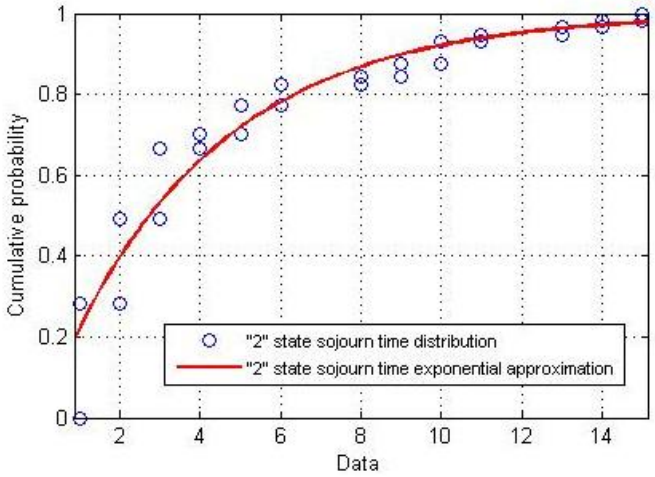

Fig. 3.16. "2" state sojourn time distributions and its approximation exponential distribution for 1000 Mbps data rate in CM2 scenario, mean noise power of -60 dB.

$$\mathbf{P}_{G-E} = \begin{bmatrix} 0.3125 & 0.6875 \\ 0.003 & 0.997 \end{bmatrix} \tag{3.29}$$

For both models, all the states sojourn time distributions are effectively exponentially distributed, except "0" state sojourn time of three states DL-DTMC model: in fact, this state is never visited.

The parameters for the others configurations were computed in the same way.

3.3.2 Artificial Trace Generation Algorithm

The algorithm for trace generation from a DTMC model based on the concept of degradation level is composed of the following steps:

- Set N, the number of packet to generate;
- Assume that the starting state is the no degradation state;
- Repeat the next steps until N packets are generated:
  - If current state is "i" then choice the $(i+1)$-th row of matrix transition $\boldsymbol{P}$;
  - On the basis of these probabilities choose the next state;
  - Add a window of w packets to the trace. The number of wrong packets depends on the degradation level associated with the current state. Distribute the wrong packets in the window in a random way;
  - Leave the current state and move on to new chosen state.

Note the assumption of choosing always "0" as the initial state is not restrictive for the this model: in fact, independently of this, the model dynamically evolves following transition probabilities. Methods to generate the artificial traces with the G-E, the 3^{rd} order Markov and the MTA model can be found respectively in [49] and [50].

3.3.3 Trace Comparative Analysis

Starting from the first configuration, an artificial trace is generated following the previous steps. In particular the artificial trace was generated using the best fitting degradation level DTMC model, the G-E model, the MTA model and 3^{rd} order Markov model proving that this model better approximates the experimental trace trend.

Figure 3.17 compares the occurrences of correctly received packets in this trace with that of the trace obtained via simulation from the G.E, the 3^{rd} order Markov, the MTA and this model. It can be seen how s the distribution of the correct packet in the artificial trace obtained by this model is similar to the distribution of the experimental trace.

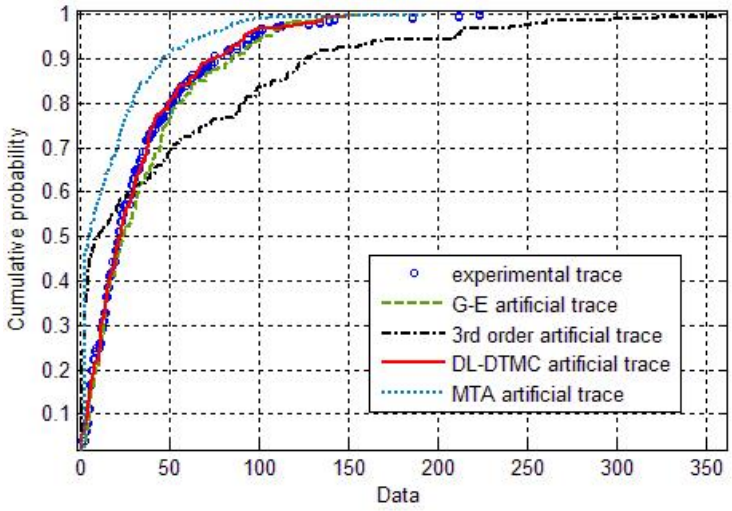

Fig. 3.17. Correct packets distribution for artificial and experimental traces, first configuration.

This trend is also confirmed by the error distribution (see Figure 3.18): in fact, the wrong packets distribution of the artificial trace obtained from the four states model represents the good approximation of the original trace errors. In particular, errors trace statistics are summarized in Table 3.1: it can be observed how μ and standard deviation value of these distribution are very

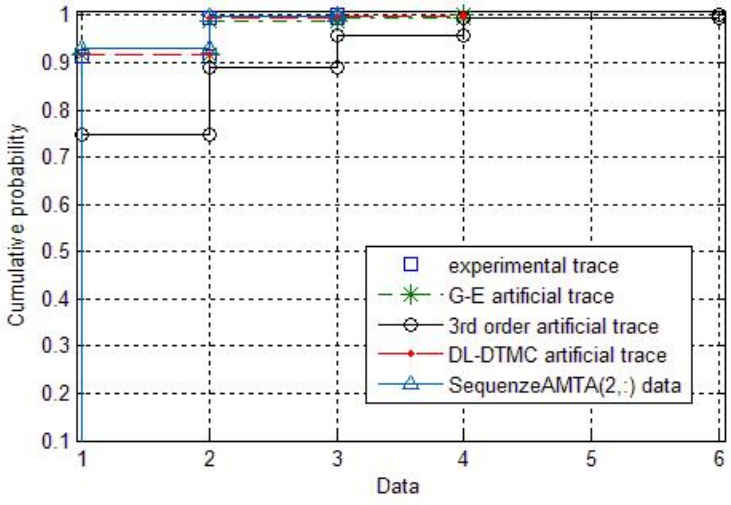

Fig. 3.18. Wrong packets distribution for artificial and experimental traces, first configuration.

Trace type	μ	σ
experimental	1.09272	0.3126
G-E model	1.09712	0.3523
3^{rd} order Markov	1.41429	0.8385
MTA model	1.07257	1.1504
4 States DL-DTMC	1.09446	0.3346

Table 3.1. Error Trace Statistics for first configuration.

similar; this is also confirmed by the standard error committed by this model (0.0152), which is less than the standard error committed by the G-E model (0.0159), the MTA model (0.0405) and the 3^{rd} order Markov model (0.0218). For error standards, see also Table 3.9.

Trace type	μ	σ
experimental	1.02899	0.1690
G-E model	1.0339	0.1825
3^{rd} order Markov	1.2963	0.6028
MTA model	1.02198	1.0444
3 States DL-DTMC	1.03125	0.1754

Table 3.2. Error Trace Statistics for second configuration.

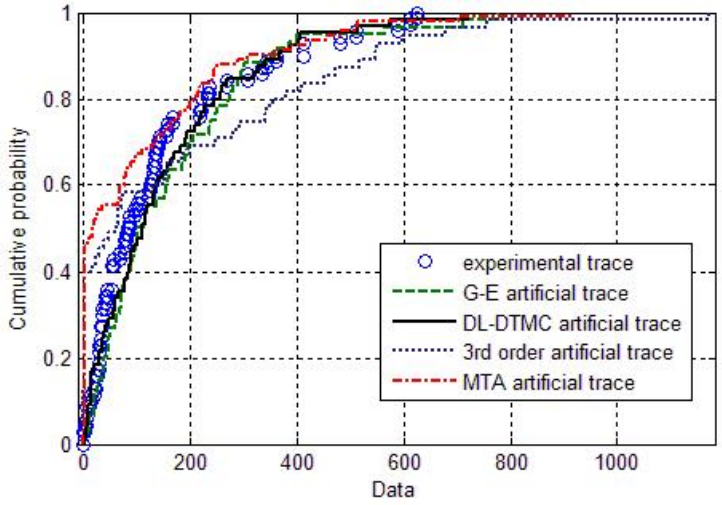

Fig. 3.19. Correct packets distribution for artificial and experimental traces, second configuration.

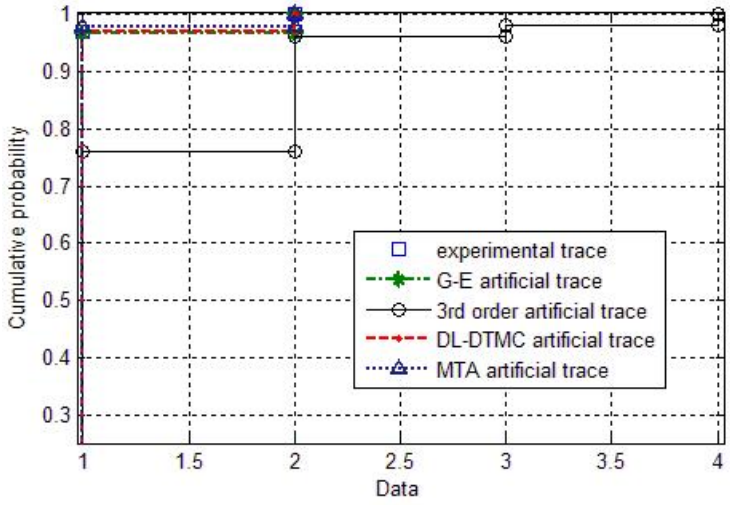

Fig. 3.20. Wrong packets distribution for artificial and experimental traces, second configuration.

In the second considered configuration, another data rate is analyzed: 55 Mbps in the CM1 scenario with a mean noise power of -30 db. Also in this case the artificial trace obtained by the degradation level based model (a three states model for this scenario) provides the better approximation of the experimental trace. Figure 3.19 and Figure 3.20 show respectively the correct received packet distribution and the wrong packet distribution obtained from the artificial traces (the G-E model, the 3^{rd} order Markov model, the MTA model and our model) and from the experimental trace that proves the goodness of this approach. This trend is confirmed by error trace statistics shown in Table 3.2: μ and standard deviation values of the experimental and degradation level model match as a standard error of 0.0145 confirms. For the other three models (the G-E, the MTA and the 3^{rd} order Markov) is obtained respectively a standard error of 0.0149, 0.0729 and 0.0196 (see Table 3.9).

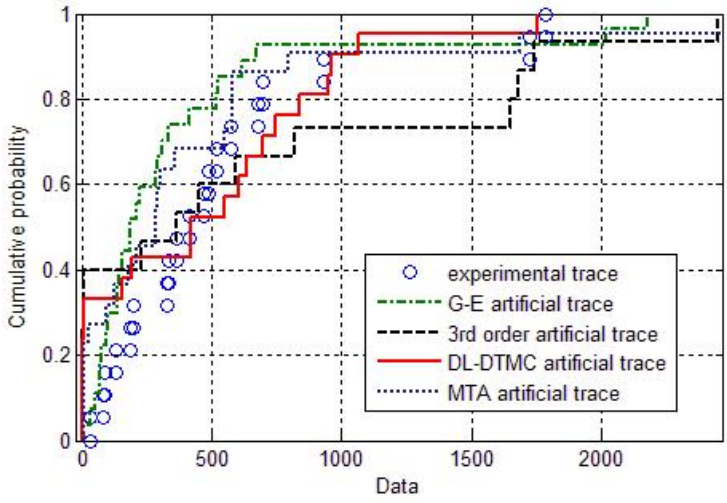

Fig. 3.21. Correct packets distribution for artificial and experimental traces, third configuration.

The third configuration analyzes 110 Mbps data rate in a CM2 multipath scenario and with an average noise power of –45 dB. In this case the best fitting DL-DTMC model is composed of three states and it is described by the transition probabilities matrix given in (3.23). The distribution of the occurrences of correctly received and wrong received packet are shown respectively in Figure 3.21 and Figure 3.22. Both figures prove how this approach approximates the original trace better than traditional methods and MTA: this is also confirmed by wrong received packets statistics summarized in Table 3.3 and by standard error that DL-DTMC commits (0.0148) which is less than the G-E (0.0165), the MTA (0.1914) and the 3^{rd} order Markov model (0.0181).

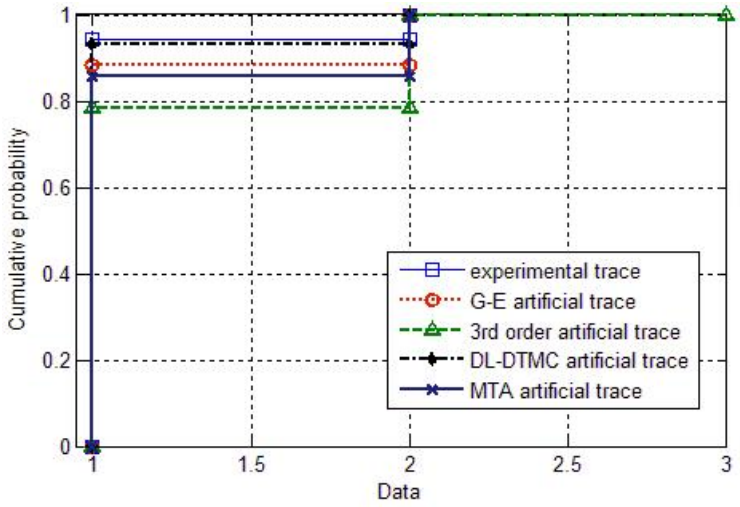

Fig. 3.22. Wrong packets distribution for artificial and experimental traces, third configuration.

Trace type	μ	σ
experimental	1.05556	0.2357
G-E model	1.11538	0.3258
3^{rd} order Markov	1.21429	1.2307
MTA model	1.14286	1.30612
3 States DL-DTMC	1.066675	0.2236

Table 3.3. Error Trace Statistics for the third configuration.

For the 220 Mbps data rate in a CM4 scenario and with an average noise power of –35 dB (fourth considered configuration), the results depicted in Figure 3.23(occurrences of correctly received packets) and Figure 3.24 (occurrences of wrong received packets) were obtained. Observing these curves, it can be seen how for both cases this model is better closed to distribution obtained from the original trace. Error trace statistics, shown in Table 3.4, confirm this trend: in fact, the error standard for this model is 0.1587, for the G-E model is 0.2133, for the MTA model is 0.91 whereas for the 3rd order Markov model it is 0.3464 (these values are summarized in Table 3.9).

The fifth configuration concerning the 500 mbps data rate in a CM2 scenario with an average noise power threshold of –50 dB. For this configuration the best fitting DL-DTMC model is the six states model characterized by (3.25). Analyzing the occurrences of correctly received packets (see Figure 3.25), it can be observed how this model closed perfectly to a distribution of correctly received packets extrapolated by trace obtained via simulation, contrarily to the 3^{rd} order Markov model and the G-E model that show a worse

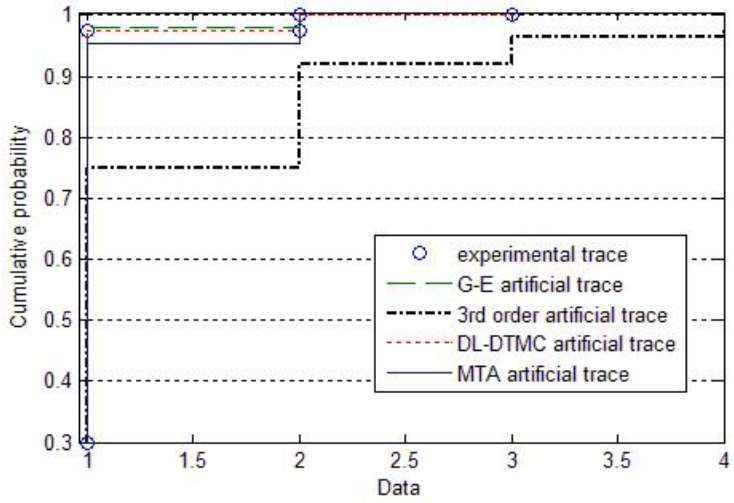

Fig. 3.23. Correct packets distribution for artificial and experimental traces, the fourth configuration.

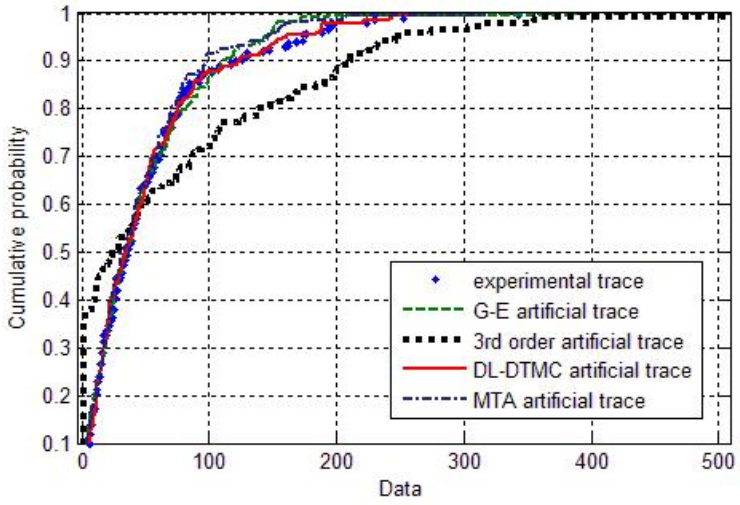

Fig. 3.24. Wrong packets distribution for artificial and experimental traces, the fourth configuration.

Trace type	μ	σ
experimental	50.7927	54.1513
G-E model	48.7413	48.6796
3^{rd} order Markov	70.0214	94.4140
MTA model	45.4866	102.2147
3 States DL-DTMC	50.2615	51.2940

Table 3.4. Error Trace Statistics for fourth configuration.

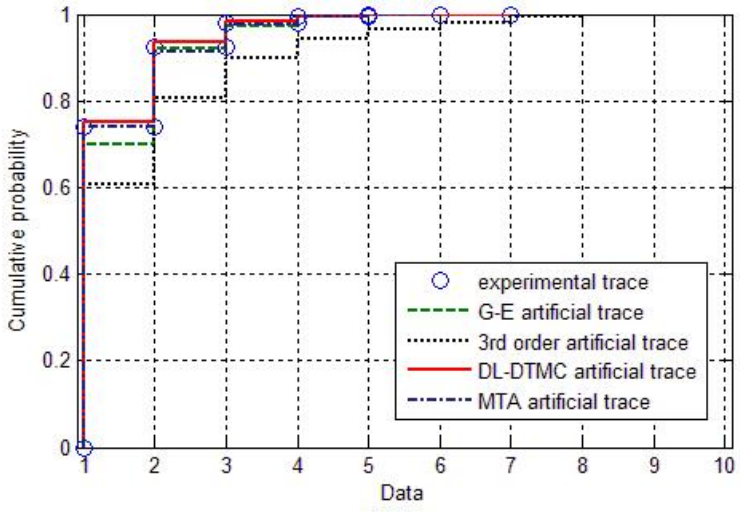

Fig. 3.25. Correct packets distribution for artificial and experimental traces, the fifth configuration.

fitting. Instead, the MTA model shows , in this case, performance similar to the DL-DTMC model: in fact, also occurrences of good received packets in trace obtained by MTA model closes to experimental distribution. In Figure 3.26, the occurrences of a wrongly received packet are plotted. For the distribution of the errors in the trace, it can be noted that the model better approximating channel behaviour is the DL-DTMC model as statistics summarized in Table 3.5 shows. In particular, this model introduces a standard error of 0.0291 contrarily to the G-E, the MTA and the 3^{rd} order Markov models introducing respectively an error of 0.0298, 0.1916 and 0.041.

In Figure 3.27, the occurrences are compared of correctly recieved packet in the original trace with that of the trace obtained via simulation from the G.E, the MTA, the 3^{rd} order Markov and this model for the sixth considered configuration (660 Mbps data rate in CM3 scenario with an average noise of -45 dB). It can be seen how the distribution of the correct packet in the artificial trace obtained by this model is similar to the distribution of the experimental trace. This trend is confirmed by the distribution of wrong packets depicted

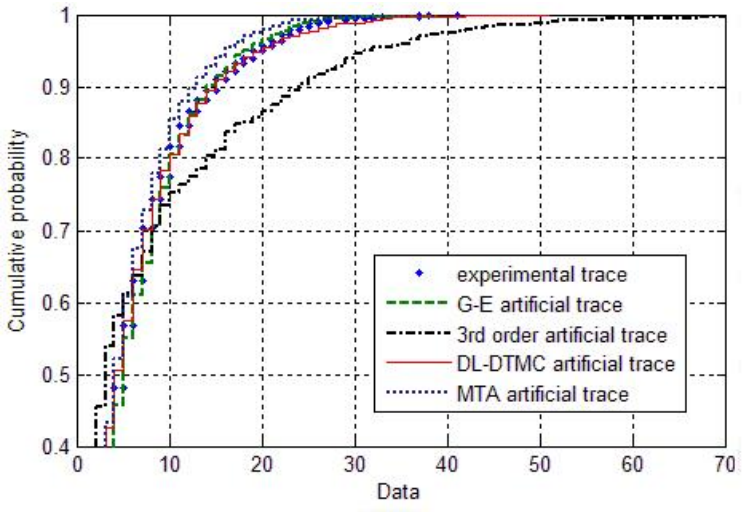

Fig. 3.26. Wrong packets distribution for artificial and experimental traces, fifth configuration.

Trace type	μ	σ
experimental	6.54272	5.9723
G-E model	6.68204	5.7333
3^{rd} order Markov	8.38776	11.6815
MTA model	5.79619	33.5958
6 States DL-DTMC	6.52574	6.4929

Table 3.5. Error Trace Statistics for fifth configuration.

in Figure 3.28 and their relative statistics quoted in Table 3.6. Observing the standard error on error statistics, it can be noted that this model commits an error of 0.0831 that is less than 0.0935, 0.9867 and 0.1283 being the standard error introduced respectively by the G-E, the MTA and the 3^{rd} order Markov models (see Table 3.9).

Trace type	μ	σ
experimental	19.5185	18.7016
G-E model	20.5292	19.4078
3^{rd} order Markov	26.0055	39.0870
MTA model	18.875	55.284
3 States DL-DTMC	18.988	16.9947

Table 3.6. Error Trace Statistics for sixth configuration.

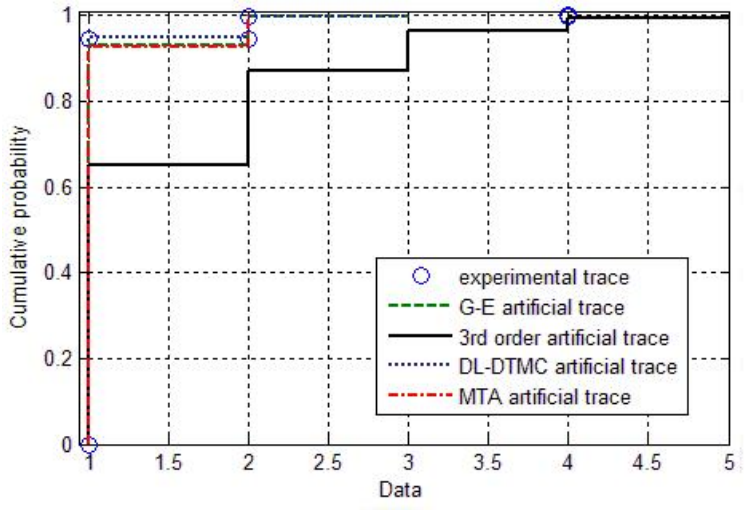

Fig. 3.27. Correct packets distribution for artificial and experimental traces, sixth configuration.

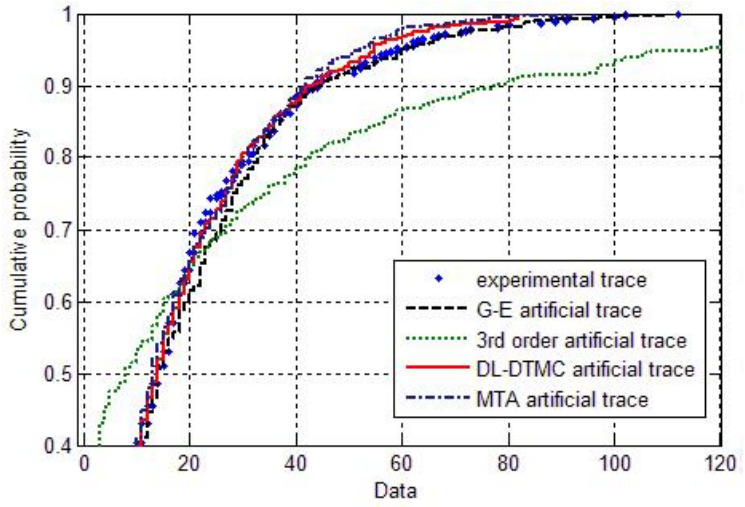

Fig. 3.28. Wrong packets distribution for artificial and experimental traces, sixth configuration.

The seventh configuration, that is 1000 Mbps data rate in the CM2 scenario with an average noise power level of -60 dB, is analyzed in Figure 3.29 and Figure 3.30. In particular, Figure 3.30 shows the occurrences of correctly received packets for this model and for other traditional models, whereas in Figure 31, the occurrences of wrong received packets are depicted for all models. Both figures prove how also for this configuration this model is the model closest to the distribution extrapolated by the original trace. This trend is confirmed by error statistics summarized in Table 3.7: the DL-DTMC model, if compared with the original trace, introduces a standard error of 0.0756, while the G-E model commits an error of 0.0766, the MTA model introduces an error of 0.994 and the 3rd order Markov model introduces a standard error of 0.1384 (see also Table 3.9).

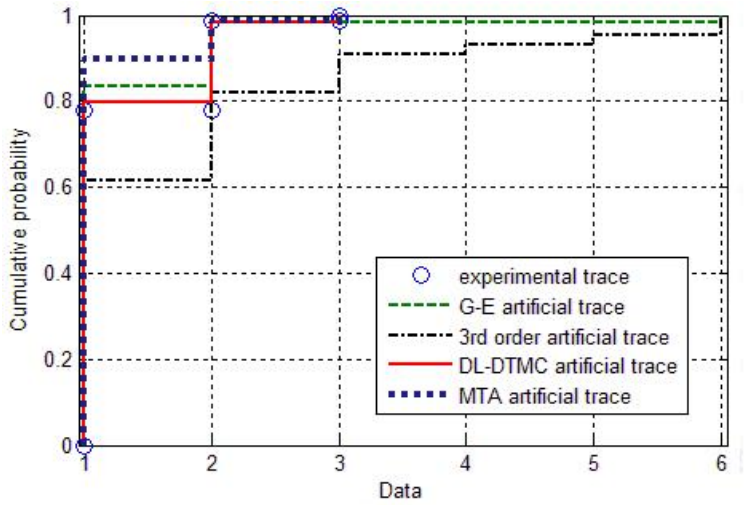

Fig. 3.29. Correct packets distribution for artificial and experimental traces, seventh configuration.

Trace type	μ	σ
experimental	7.60294	7.1615
G-E model	7.63235	6.8848
3^{rd} order Markov	11.4889	15.9753
MTA model	7.20253	51.8765
3 States DL-DTMC	7.62319	6.7717

Table 3.7. Error Trace Statistics for seventh configuration.

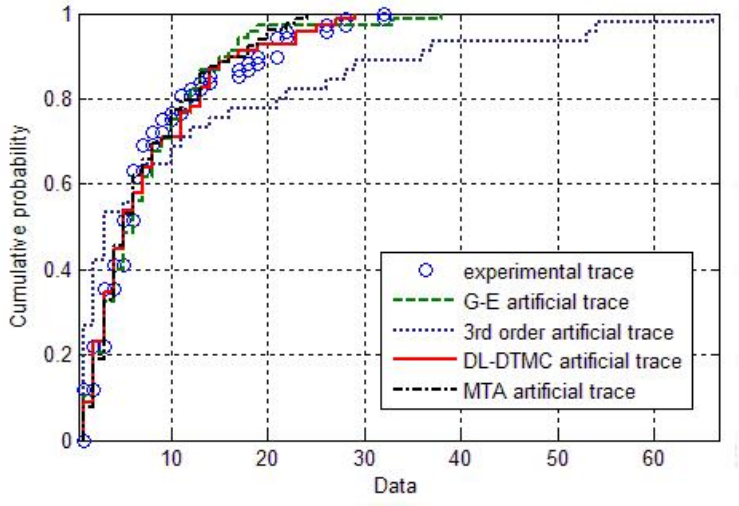

Fig. 3.30. Wrong packets distribution for artificial and experimental traces, seventh configuration.

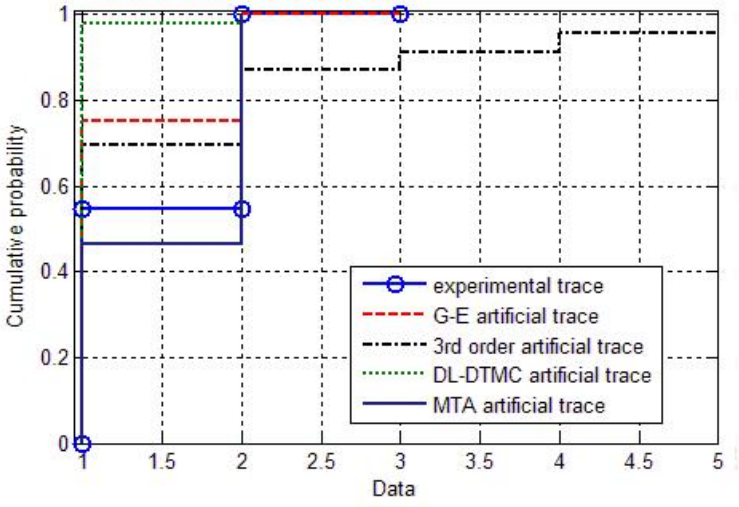

Fig. 3.31. Correct packets distribution for artificial and experimental traces, eighth configuration.

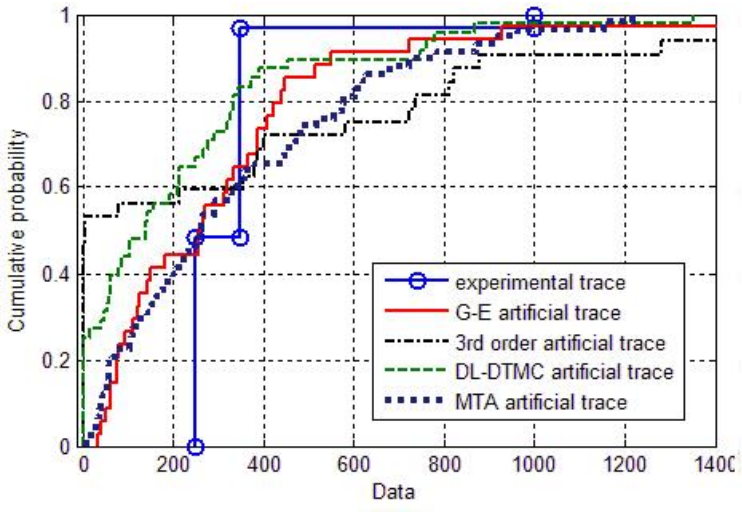

Fig. 3.32. Wrong packets distribution for artificial and experimental traces, eighth configuration.

Trace type	μ	σ
experimental	320.727	131.6053
G-E model	311.924	310.0886
3^{rd} order Markov	330.426	458.2588
MTA model	344.138	410.6513
3 States DL-DTMC	220.479	278.2281

Table 3.8. Error Trace Statistics for eighth configuration.

Finally, in the last configuration 1320 Mbps data rate is analyzed in a CM3 scenario with a mean power noise of -50 dB. In Figure 3.31 and 3.32 are plotted respectively correctly received packet distribution and wrong packet distribution obtaining from artificial (always the G-E model, the 3^{rd} order Markov, the MTA model and this model) and from experimental traces. It can be seen how, in this particular case, the model that better fits the original trace is the G-E model as error trace statistics shown in Table 3.8 prove: μ and standard deviation values of the experimental and the G-E model match as a standard error of 0.6165 demonstrates, contrarily to the 3^{rd} order Markov, the MTA model and the DL-DTMC that show respectively a standard error of 0.673, 0.697 and 0.7321. This configuration shows a different trend with respect to the others, because for this noise power level the system is not in the applicable region of the degradation concept: it means that as a consequence of such a degraded link there is a total PER $> 98\%$ and therefore our original trace is composed almost totally of wrong packets, so only two states can be sufficient to describe the channel dynamics.

In Table 3.9 the standard errors relative to the occurrences of wrong received packets are summarized for all considered configurations.

Standard Error				
Configuration	**G-E**	**3^{rd} ord. Markov**	**MTA**	**DL-DTMC**
1^{st}	0.0159	0.0218	0.0405	0.0152
2^{nd}	0.0149	0.0196	0.0729	0.0145
3^{rd}	0.0165	0.0181	0.1914	0.0148
4^{th}	0.2133	0.3464	0.91	0.1587
5^{th}	0.0298	0.041	0.1916	0.0291
6^{th}	0.0935	0.1283	0.9867	0.0831
7^{th}	0.0766	0.1384	0.994	0.0756
8^{th}	0.6165	0.673	0.697	0.7321

Table 3.9. Standard Errors for all configurations.

3.4 Conclusions on Chapter 3

In this Chapter, a high level wireless channel model is provided based on the concept of degradation level DTMC modelling, useful in every simulation requiring work at the packet level. For this purpose, packet error trace analysis is used to model multi-state channel models. The models obtained are therefore tested by generating artificial traces and comparing them with the trace obtained by experimental simulation and with the artificial trace obtained by the classic G-E Markov chain model, the MTA model and the 3^{rd} order Markov model. The new approach is applied to the UWB channel modeling. Performance evaluation showed that this model better fits the experimental trace than the MTA model, the G-E model and the 3^{rd} order Markov model, when the combination of data rate, multipath scenario and average AWGN power level lead the system into the applicable region of the degradation concept. This region is a particular condition in which only two states are not sufficient to describe the evolution of the channel: typically this region coincides with a noise threshold whereby the trace is far enough from the degenerative cases (which are a totally correct or wrong trace). Furthermore, the soundness of this approach (for the applicability region) is confirmed by error trace statistics and in particular by a lower standard error committed with respect to the traditional approach and MTA approach. Finally, note that the number of additional states needed to improve accuracy depends on the specific operating conditions and so on the scenario (CM1, CM2, CM3 or CM4), data rate, noise power level and naturally on the specific wireless system.

4

IA-AODV routing protocol for UWB Networks

In the literature, many works have approached problems related to physical and MAC layers of UWB system, but, at the best of our knowledge, few studies are dealt with the UWB routing issues. However, traditional ad-hoc network approaches, based for example on minimum hop count or geometric criterions, can be inadequate for these network because UWB system are strongly affected by the mutual interference between nodes. The interference is the most undesired problem in UWB wireless network and it can cause an irretrievable degradation of communications [57]. Therefore, a routing protocol, that does not take into account directly interference "between the nodes could lead to choose a path wrong in terms of degradation of the signal: the distance between the source and destination can be minimized, but the level of interference may be too high if new metric are not defined in the routing protocols For this reason a new protocol based on the concept of interference is proposed in this work. The proposed routing protocol employs as physical and MAC layers the Dynamic Channel Coding - MAC (DCC-MAC) model ([58],[59]). This MAC protocol allows devices to perform multiple parallel transmissions, adapting communications on the basis of interference perceived by the same devices. Furthermore, DCC-MAC employs an UWB impulse radio physical layer based on TH-UWB IR as in ([60],[28]). Our protocol, called Interference Aware-based Ad-hoc On Demand Distance Vector (IA-AODV), lays its foundation in the classic Ad-hoc On Demand Distance Vector (AODV) protocol [61], of which inherits part of working operation and control packets. The novelty of the proposal is in the two distinct metrics adopted for the choice of the optimal route from the source to the destination: they are not based on the hop number, as the classic AODV, but on the global interference perceived by nodes, called Node Interference (NI) metric, and on the interference affecting the links involved in the transmission, called Link Interference (LI) metric. In order to verify the IA-AODV protocol goodness, a Network Simulator 2 (ns-2) simulator was realized and a comparison with AODV is carried out.

4.1 State of Art

Generally, the classic ad-hoc network routing protocols employ metrics such as minimum hop count [61] or geometric criterions ([62],[63][64]). Therefore, ad-hoc routing algorithms must provide the optimum route adapting themselves, simultaneously, to the frequent and unpredictable network topology variation. Also some UWB routing algorithms make use of the high precision localization capability of UWB network ([65],[66],[67]) to choose the optimum route: using location information, nodes can choose to send packets to neighbors that are closer to the destinations [68]; moreover, in order to improve these mechanisms, cluster structures can be formed, and can lead to a routing algorithm described by [69].

All these approaches can be useful in those architectures that are not affected by neighbor interference, but they are not valid for the UWB networks. The traditional routing protocols used in ad-hoc networks, such as the AODV [61], Dynamic Source Routing (DSR) [70], and others ([71],[72]), do not take into account directly interference "between the nodes". In this way, the choice of a path, on which the packets must travel from the source to destination, may be wrong in terms of degradation of the signal: the distance between the source and destination can be minimized, but the level of interference may be too high if new metric are not defined in the routing protocols.

Transmission interference is the most difficult problem for wireless communications. In the last few years, many new techniques have been proposed to reduce the effects of interference, defining interference-aware metrics and routing protocols. The reciprocal interference between system nodes considerably affects the path-delay and, so, the data-rate. The older interference-aware metrics tried to optimize these parameters: the DIAR ([73],[74]) is one of the interference-aware routing protocols for IEEE 802.11 networks and it is based on the Network Allocator Vector Count (NAVC). Thanks to the simulation results obtained in ([73],[74]), it has been discovered that the NAVC is not dependent on the total number of nodes in the system. If the path with the lower NAVC is chosen, then it corresponds to the one with a lower delay and a lower interference ([10],[71]). A similar approach is made in [72], where the employed metric chooses the path with the lowest path delay, defined as the interval between the Route REQuest (RREQ) dispatch and the related Route REPly (RREP) reception. In [75], the chosen interference-aware metric is different from the previous one: the authors make the assumption that if there is a higher number of neighbour nodes, a higher probability of interference for a node will be observed; for this reason, through the adopted metric, called blocking metric $B(k)$, the routing protocol selects a certain number of paths, verifying that the sum of the coverage values of the nodes belonging to the single path is the lowest. It must be remembered that the coverage value of a node is the number of nodes that are directly covered from it. Starting from classic AODV protocol [61] two new metrics, based on the concept of global interference perceived by a node, for the NI metric, or on the interference

perceived along the paths of a route, for the *LI* metric, have been proposed in this work. AODV is a reactive routing protocol based on distance vector algorithm. A key feature of this protocol is the use of "*sequence numbers*" , which provides a method for a node to establish if a particular route is updated.

In the following are the main novelties of our protocol:

- Our protocol introduces the concept of interference in the choice of optimum route in this way improving the general system performance: in fact, in a UWB network, the minimum hop route, such as for example in AODV, could not be an optimum choice because it could be affected by a high amount of interference that could make the communication substantially impracticable;
- Two distinct metrics are proposed: the first one, called *NI*, is based on the global interference perceived by nodes involved in the communication; instead, the second one, called *LI*, is based on the interference perceived on only the links belonging to the route from the source to the destination;
- Links refresh, provided by standard AODV, occurs only in the presence of breakage of links and not when there is a substantial variation in interference. However, in the presence of scenarios with mobility, having the routing tables updated on the basis of important variation in the perceived interference, could lead to a better use of the minimum interference routes. For this purpose, we introduced a further refresh mechanism taking into account the interference variation.

4.2 Reference Scenario

In this section, some considerations about reference physical and MAC layers are made. In this work, we adopt as MAC layer the DCC-MAC model ([58],[59]). This protocol allows devices to perform multiple parallel transmissions, adapting communications on the basis of interference perceived by the same devices. To realize this, an opportune coding mechanism is used. DCC-MAC employs an UWB impulse radio physical layer based on TH-UWB IR as in ([28],[60]). In the *time-hopping* based system, the transmission time is divided in short chips of T_c duration aggregated into frames (whose duration is T_f) in order to transmit one pulse in one chip per frame. Multi-user access is provided by pseudo-random Time Hopping Sequences (THS) that determine in which chip each user should transmit. Besides, due to the nonzero cross-correlation between time-hopping sequences, time-asynchronicity between sources and a multipath channel environment, TH-UWB is sensitive to strong interferers. Further details on this physical layer model can be found in ([28],[60]).

A specific analysis of UWB network optimum planning is described in [76] where DCC-MAC is also discussed. Interference at the receiver is more harmful when the impulses of a neighbor collide with those of the source. Instead

of inhibiting the sources into exclusion region, DCC-MAC uses a different strategy called *interference mitigation*.

Interference mitigation allows the detection and erasure of interfering impulses having an energy higher than the signal received from the source: this scheme cancels the samples resulting from a collision with pulses of a strong interferer and replaces them by erasures (for example skipping them in the decoding process). In contrast to other schemes such as power control or exclusion mechanisms, interference mitigation does not require any coordination between nodes ([58],[59]): when a source must communicate, it transmits at the maximum power without considering other ingoing transmissions. In particular, the communication uses either public (receiver-based) or private THSs. The public THS of user with MAC address A, called THS(A), is the THS produced by the Pseudo-Random Generator (PRG) with seed = A. The private THS of users A and B, called THS(AB) is the THS produced by the PRG with a seed equal to the number whose binary representation is the concatenation of A and B. Note that a node can always compute the THS used by a potential source. In order to take more advantage of the channel, transmission needed to be constantly adapted to the higher code rate allowing a correct decoding at the receiver. Dynamic coding is performed through a hybrid *Automatic Retransmission request* (ARQ) protocol: if channel conditions degrade and the coding fails additional information is sent until the packet is correctly decoded; if no further information is available, the transmission failed. Another issue regards the possibility of more nodes in transmission toward the same destination: the goal of the private MAC protocol is to ensure that several senders cannot communicate simultaneously with one destination; the private MAC solves this problem by a combination of receiver-based and invitation-based selection of THSs. Moreover, the mechanisms provided by DCC-MAC, based on the management of THS, allow us to estimate the interference perceived on the reception of a packet. Further details of this protocol can be found in ([58],[59]).

Besides, some considerations must be given to the channel model employed in our simulations. As in ([58],[59]), we used the propagation indoor model described in ([58]): in particular, the power attenuation in decibels, due to distance, is at a given distance d:

$$\overline{PL(d)} = [PLo + 10\mu_\gamma \log d] + [10n_1\sigma_\gamma \log d + n_2\mu_\sigma + n_2n_3\sigma_\sigma] \qquad (4.1)$$

where the intercept point PLo is the path loss at $d_0 = 1$ m whereas μ_γ and σ_γ are respectively the normal distribution media and the standard deviation of the decaying path loss exponent γ. The shadowing effects, in accordance with ([58]), are modelled through a zero-mean Gaussian distribution with standard deviation σ, normally distributed and characterized by average value μ_σ and standard deviation σ_σ. n_1, n_2 and n_3 are zero-mean Gaussian variables with unit standard deviation $N[0, 1]$. More specifically, the first term of

(4.1) represents the median path loss, whereas the second term is the random variation around median value. Further details are available in ([58]).

Finally, we recall that the concept of interference taken into account in this treatment is that one expressed in the work of Le Boudec et al. that is also the basis of the DCC-MAC protocol [77].

4.3 IA-AODV Protocol

The proposed protocol has as basis the classic AODV protocol [61], from which inherits part of its working operation and control packets. The novelty of the proposal is in two metrics adopted for the choice of the optimal route from the source to the destination and in the route maintenance procedure: proposed metrics are not based on the minimum hop number, as with the classic AODV, but on the global interference perceived by nodes, for the *NI* metric, and on the interference affecting the link involved in the transmission, for the *LI* metric. In order to realize these metrics, it has been necessary to modify some control packets: in particular, the *Interference* field is added to the RREP and RREQ packets. The modified structures of the packets are respectively shown in Figure 4.1.a and Figure 4.1.b. The modification was also made at the entry of the routing tables: the field *HopCount* was added to the *Interference* field, in which the interference from the node to the destination is stored, and *IsCorrect* field, a Boolean variable that indicates the validity or not of links (see Figure 4.1.c). This last variable is needed because the interference on the link A-B could be different from that on the link B-A therefore we need to know if the value stored in the entry refers to an interference perceived or transmitted by the node (this concept is better explained in the following). Other parameters needed by our protocol are given in the next subsection.

4.3.1 Analytical Formulation

In this subsection, the analytical formulation of our metrics is described. Before starting our analysis, some definitions must be given:

- P_{BA} is the data packet that node B is sending to the node A;
- P_l is a generic data packet received in a certain observation window by a given node;
- PI (*Packet Interference*) is the interference contribution, expressed in Watts, generated by a packet that is interfering on the currently received packet;
- n is the number of packets that are interfering with the reception of a specific packet;
- CTC_i (*Collision Time Coefficient*) is the time fraction of the receiving time for P_{BA} that is affected by the interference of the packet p_i;

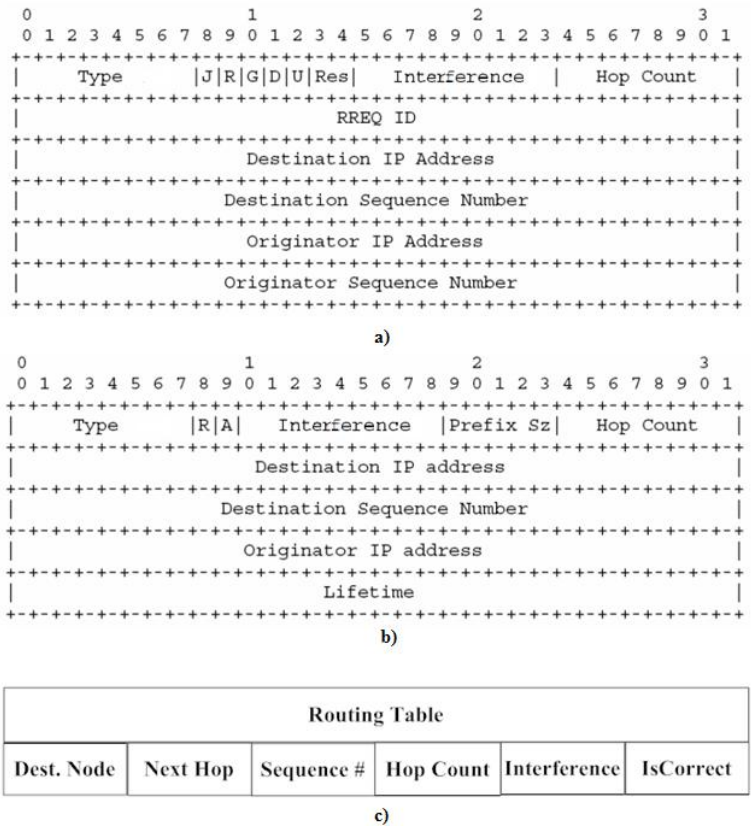

Fig. 4.1. a) RREQ packet structure. b) RREP packet structure. c) Routing table entry.

- *WI* (*Window of Interference*) is the interval during which the interfering packet impacts on the reception of P_{BA};
- $I_{P_{BA}}$ is the total perceived interference for P_{BA};
- *OW (Observation Window)* is a fixed observation window in which we collect the information needed to compute the interference;
- OW_k is the k-th observation window;
- I_{P_l} is the total perceived interference for P_l;
- SPI_k (*Set of Packet Interference)* is defined as the set of I_{P_l} values observed during the k-th period OW_k;
- GI_k is the global interference perceived by a node during the k-th observation window OW_k;
- *NSW (Number of Stored OW)* is the number of OW that must be taken into account for the metric NI;
- GI is the global node interference employed in the NI metric for a generic node;

- $I_{P_{BA_j}}$ is the interference perceived by A at the reception of j-th packet from node B;
- m is the number of packets received by a node on a specific link during the observation window *OW;*
- $\overset{\wedge}{ij}$ link is a generic link belonging to the route from the source to the destination in the LI metric;
- $I_{\overset{\wedge}{ij}}$ is the interference perceived on the generic link $\overset{\wedge}{ij}$ in LI metric;
- *Path(S,D)* is the set of nodes belonging to the route from *Source* to *Destination*;
- NI is the *Node Interference*-based metric;
- LI is the *Link Interference*-based metric;
- I_{NI} is the interference computed by the NI metric;
- I_{LI} is the interference computed by the LI metric;
- α is a threshold that influences the occurrences of the interference information refresh;
- SI(*Stored Interference*) is the interference (global or on a link) stored by a node.

We suppose that a generic node A is receiving a packet, denoted by P_{BA}, from node B. During the reception of this packet, the node A detects an amount of interference (intended as interfering power in Watts) due to some packets transmitted by the nodes in its coverage range (and different from the node B). We indicate with PI the interference due to a generic packet interfering in the packetP_{BA}. This amount of interference is given by:

$$PI = P_{RX} \cdot CTC \tag{4.2}$$

where P_{RX} is the received interfering power, while CTC is the *Collision Time Coefficient*, that is the fraction of the time needed to receive P_{BA} on which the interfering packet impacts. In particular, CTC is defined as [58], [59]:

$$CTC = \frac{WI}{TE_{P_{BA}} - TS_{P_{BA}}} \tag{4.3}$$

where TE_{PBA} and TS_{PBA} are, respectively, the start and end reception time for the P_{BA} packet, while *WI,* the interval during which the interfering packet impacts on the reception P_{BA}, is given by:

$$WI = \min(TE_{P_{BA}}, TE_{PI}) - \max(TS_{P_{BA}}, TS_{PI}) \tag{4.4}$$

where TS_{PI} and TE_{PI} are, respectively, the start and end reception time for the interfering packet. If we denote with PI_i the interference, perceived for the reception of the P_{BA} packet, due to the specific interfering packet i, then the total perceived interference for P_{BA}can be expressed as:

$$I_{P_{BA}} = \sum_{i=1}^{n} PI_i = \sum_{i=1}^{n} P_{RX_i} \cdot CTC_i \tag{4.5}$$

This *NI* metric can be defined by subdividing the temporal axis in *OW* in which a node receives a certain number of packets. We indicate with P_l a generic packet received during a *OW*, with I_{Pl} the perceived interference relative to P_l reception computed applying the (4.5) and with TS_{Pl} and TE_{Pl} respectively the start and end reception time for the generic packet P_l. From this, we can express SPI_k as:

$$SPI_k = \{I_{P_l} | TS_{P_l} \in OW_k \wedge TE_{P_l} \in OW_k \} \tag{4.6}$$

The *GI* that belongs to OW_k is:

$$GI_k = \sum_{j}^{|SPI_k|} SPI_k(j) \Big/ |SPI_k| \tag{4.7}$$

where $SPI_k(j)$ and $|SPI_k|$ are, respectively, the j-th element and the cardinality of the SPI_k set.

From the definition of *PI*, the *NI* metric can be derived as a parameter for evaluating the interference observed by a certain node. The global interference *GI*, employed in the *NI* metric, for a generic node is expressed as:

$$GI = \left(\sum_{l=1}^{NSW} GI_l \right) \Big/ NSW \tag{4.8}$$

where *NSW* is the number of *GI* that must be taken into account.

The *NI* metric is based on the global node interference calculated as the ratio between the sum of the interference *GI* of each node belonging to the route and the number of hops composing the route:

$$I_{NI}(S, D) = \sum_{j \in Path(S,D)} GI_j \Big/ HopCount_{Path(S,D)} \tag{4.9}$$

where j and *HopCount* are, respectively, the node indexes and the number of hops of the considered route. S and D is the source-destination pair.

After having introduced the global interference metric, now we proceed with the description of the link interference metric *LI*.

The node A monitors the wireless link condition for each neighbor computing the interference perceived on every link. Regarding its neighbor B, the node A will estimate the average interference perceived for the reception of each packet from B in a specific observation time window *OW*. At the end of this observation, the node A computes the average interference perceived on the link as:

$$I_{BA} = \frac{\sum_{j=1}^{m} I_{P_{BA_j}}}{m} \tag{4.10}$$

where $I_{P_{BA_j}}$ is the interference perceived by A at the reception of the $j-$th packet from node B, while m is the number of packets received by node A during *OW.*

The proposed metric employs the link interference values to find the minimum interference route on which to forward the packets. In particular, the interference from a source S to a destination D for the LI metric is simply given by:

$$I_{LI}(S, D) = \sum_{\hat{ij} \in Path(S,D)} I_{\hat{ij}} \tag{4.11}$$

where the $\hat{ij}$ link is a generic link belonging to the route from the source to the destination and $I_{\hat{ij}}$ is the interference perceived on it computed according to (4.10). The source will choose the freshest route toward destination (managed with *sequence number* as in standard AODV) and with the lowest interference value, computed applying the (4.11).

4.3.2 Refresh Procedure

Every node will store the average interference perceived on each path, linking it to its neighbors applying the (4.10), and the global value of interference computed applying the (4.8). However, this information can vary quickly in the network and therefore a refresh mechanism is necessary in order to avoid the propagation and the use of false interference information. Furthermore, if the interference perceived by a node significantly increases, it is necessary to invalidate all routes using that node to reach a generic destination.

We solve this problem by introducing an interference variation control in each node. The interference values are updated only if the interference variation, with respect to the stored values, is greater than a prefixed threshold α. Analytically, this can be expressed as:

$$\begin{cases} SI_k = SI_{k-1} & if \quad \frac{I - SI_{k-1}}{LI_{k-1}} < \alpha \\ SI_k = I & if \quad \frac{I - SI_{k-1}}{SI_{k-1}} \geq \alpha \end{cases} \tag{4.12}$$

In (4.12), SI_{k-1} is the value stored at the end of the $(k-1)$-th iteration, while I is the interference computed in the k-th iteration applying, on the basis of the adopted metric, (4.8) or (4.10). The procedure for the LI metric is shown clearly in Figure 4.2. If the updating of the value stored in SI is required, then the node performing the computing, informs its neighbor about interference variation (for example, referring to (4.12) the node j informs node

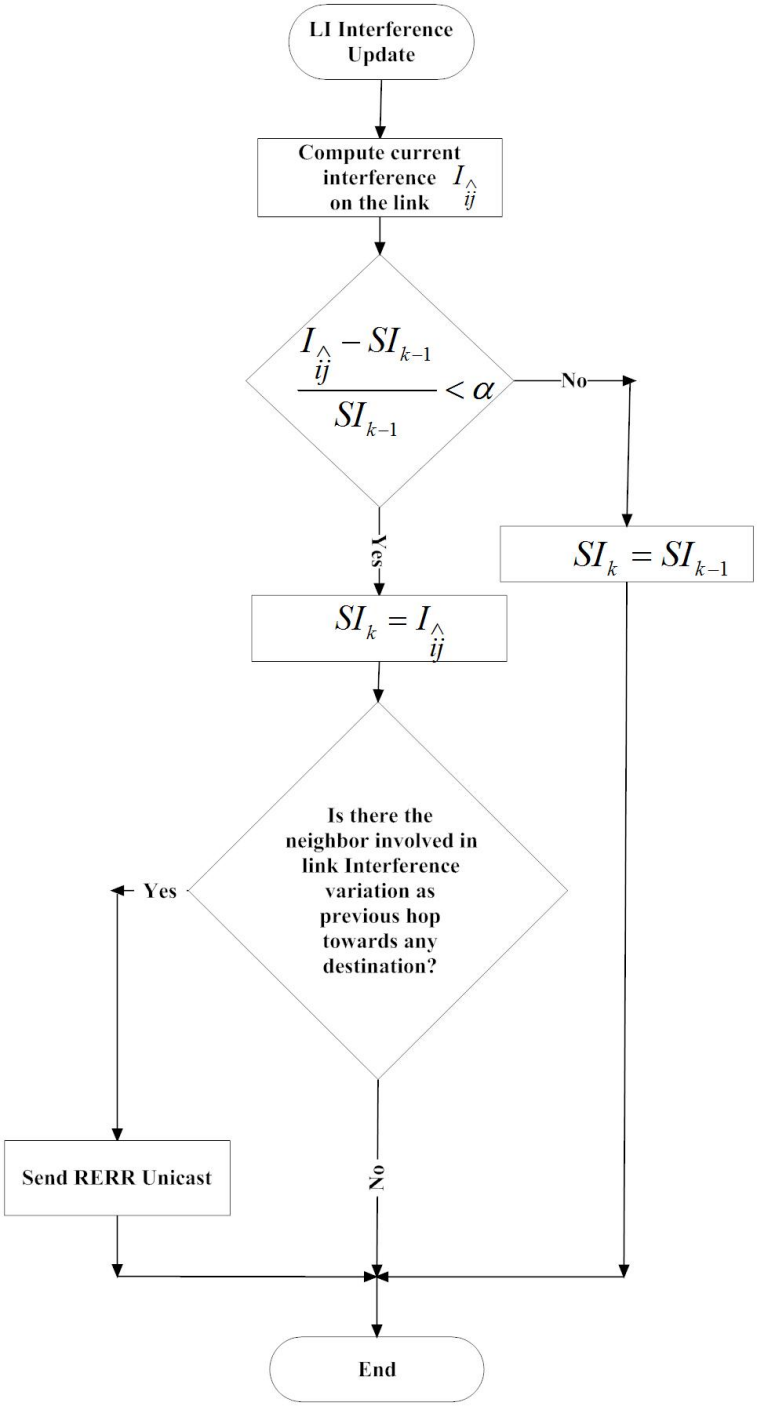

Fig. 4.2. Interference Control on a generic link for the LI metric.

i about link interference variation) using the unicast RRER mechanism of AODV protocol: this message is propagated to every node of the path toward destination D preceding the node discovering interference variation.

4.3.3 Route Discovery and Maintenance

When a source must communicate with another node of the network (called destination), it checks in its routing table if a valid *entry* toward that destination is present. In this case, the packets are sent toward the node indicated as *next hop* in the *entry* (likewise AODV standard). An *entry* is valid if it is fresh (this is provided by standard AODV procedure) and the *IsCorrect field* is set to true. Otherwise, if an *entry* is not present or it is invalid, the sender starts the route discovery procedure: a RREQ packet, in which the *Interference* field is set to zero (other fields are set following standard AODV procedure), are sent in flooding. When a node receives a RREQ, it adds the stored value of interference (this value is stored in *SI)* to the *Interference* field; therefore, if it does not have an *entry* toward the sender, it creates a new *entry* inserting in the *Interference* field the new value stored in the RREQ and setting to false the *IsCorrect* field. This last step is needed because the interference stored in the RREQ is computed from the source toward this node and it could be different from the interference on the backward route: we must avoid that other RREQs use this wrong information about interference to reach the sender from the current node. If the *entry* is already present and its *IsCorrect* field is set to false, then the *Interference* field is updated only if the interference value stored in the RREQ is less than that one in the *entry* (*IsCorrect* field is not updated). In this way, the nodes, locally, already make a choice about the minimum interference route: if information updating about interference is available, the RREP will find fresh value of interference and it will be forwarded automatically on the minimum interference route available until now. If the *IsCorrect* field is set to true, the *entry* is not modified in order to not mistakenly change the information refering to the correct direction toward sender.

After these operations, the node must verify if it is the destination or if it has a valid route toward destination (recall that the *IsCorrect* field must be set to true). If neither condition is satisfied, the node must forward the RREQ packet with the updated *Interference* field. Otherwise, the node must generate a RREP packet toward the sender through the nodes belonging to the route crossed by the RREQ (as in classic AODV). In particular, if the node is the destination, in the *Interference* field of the RREP the interference value *SI* stored by the node is moved; otherwise, it must insert the value stored in the *Interference* field of the routing table *entry* relative to the considered destination in the RREP. After these operations, the RREP (with the remaining fields set according to standard AODV) is forwarded to the previous hop of the route. When a generic node receives a RREP packet, it must apply the procedures described in Figure 4.3.

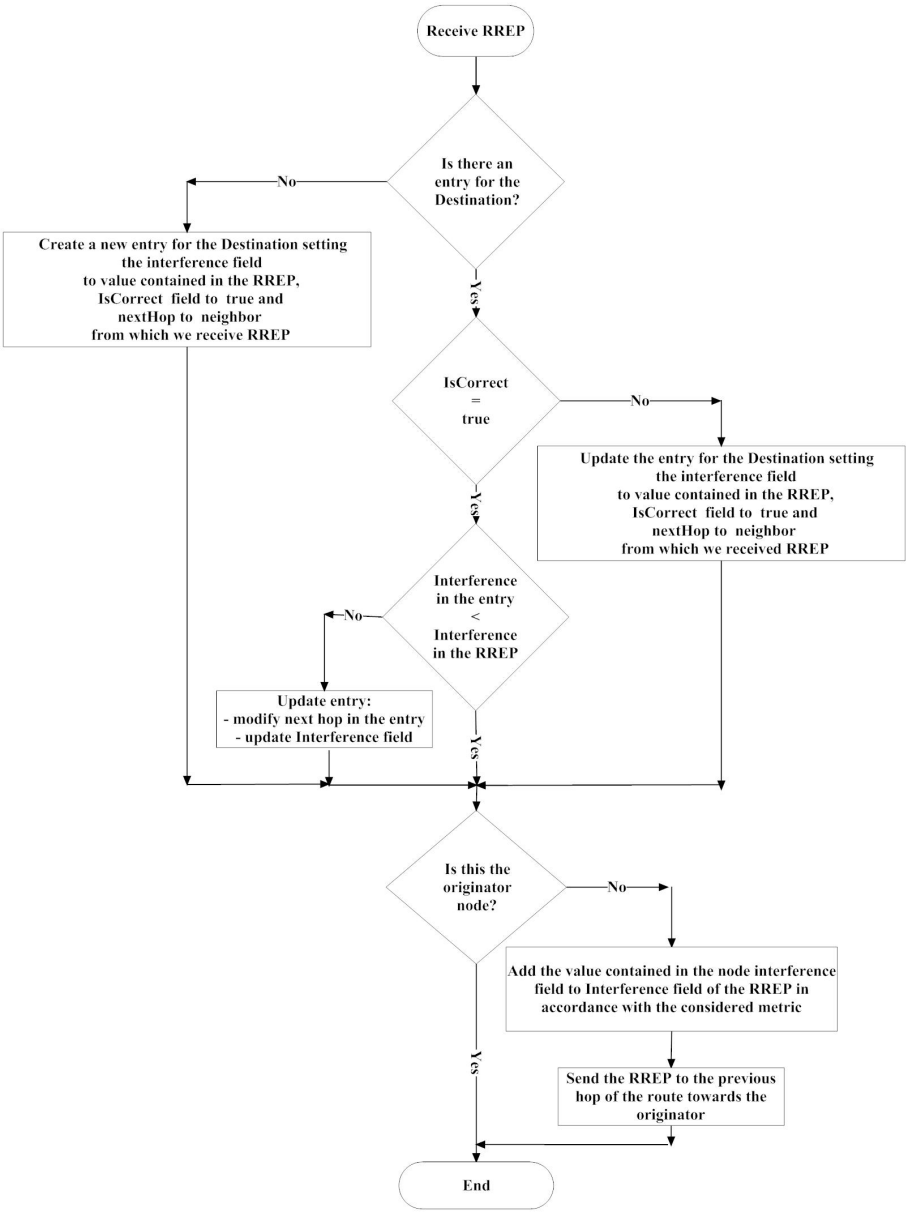

Fig. 4.3. Procedures performed by a node at the reception of a RREP packet.

Regarding the route maintenance, the proposed protocol maintains the AODV procedures based on the route freshness, on the link breakage and on the sending of the RERR message. In addition to these procedures, a further mechanism was introduced to take into account of significant variation in interference. For example, considering the *LI* metric, the node A computes, at each observation window, the average interference perceived on the path linking it to the node B applying the (4.10): if this interference is significantly different with respect to the previously stored value, i.e. an updating of *SI* is required according to (4.12), then the node A sends a particular unicast RERR to the neighbor node involved in the link variation (in this case B). When the node B receives the RERR, it drops all entries in the routing table having the node A as next hop because the interference toward the destination stored in the *Interference* field of that *entry* is no longer accurate. Then the node B informs, through the forwarding of an unicast RERR, all its precursor nodes involved in the interference variation of that route. The RERRs are forwarded backwards until all the nodes involved know the variation in the link B-A. In a similar way, in the *NI* metric, the nodes exchange information about significant interference variation. This procedure allows us to obtain the information about the interference of various links and nodes always updated in the network.

4.4 Performance Evaluation

In this section, the simulation results will verify the improvements, introduced by IA-AODV, in comparison with AODV.

The simulator, taken into account for our tests, is ns-2 [78]. Further details can be found in [78]. In particular, we have extended the ns-2 UWB implementation available on [79].

Our protocol was tested considering the same reference scenarios: the node are randomly collocated on a $200m \times 200m$ grid, on which they move according to *Random Waypoint* mobility model [80] with a speed variable in the range 1-4 m/s. Further simulation parameters are summarized in Table 4.1.

Performance evaluation has been carried out in terms of Data Packet Delivery Ratio (DPDR), Average End-To-End Delay (AED) and Normalized Routing Overhead (NRO).

In the following, some considerations on the threshold α are made and then simulation results are shown.

4.4.1 Analysis of α threshold

As previously described, when a node perceives an interference variation greater than a given threshold α on a specific link, it invalidates the route involved in this variation. Furthermore, this could also mean sending RERR

Parameter	**Symbol**	**Value**
Transmission Power	Pt	0.280 mW
Nominal Bit Rate	br	18 $Mbps$
Bandwidth	Bw	5 GHz
Max speed	V_{MAX}	4 m/s
Packet Size	P_{size}	512 $Byte$
Interval between Packets	t_P	0.012 s
Node number	N	120, 140, 160,200
Max concurrent connection number.	Cmc	4, 8, 12, 20
Observation Time Window	OW	10 s
Number of WO to consider for NI metric	NSW	5

Table 4.1. Simulation Parameters.

messages in that network portion and starting a serach for a new route (discovery procedure). Therefore, we can deduce as the choice of parameter α is a very important issue because it can affect link refresh mechanisms: a too small α could lead to frequent updating of the interference information that can cause a network traffic increment; on the other hand, too high α would mean rare updating and so the information concerning interference could become obsolete.

In order to find, in an experimental way, the value of α maximizing DPDR (this performance parameter is preferred to others because our main goal is to reduce interference and so the packet loss) many simulations were carried out.

Simulation results show that the optimum value for α is around 5% independently of the number of the nodes and maximum concurrent connections. In particular, in Figure 4.4.a, the PDR vs. α trend is shown for a scenario with four maximum concurrent connections and 120 nodes: in this case, we can see as the DPDR increases until α =5%, it remains approximately constant and then it decreases for α>8%. In order to verify our choice, the number of nodes and the maximum number of concurrent connections were increased respectively to 140 and 8. Even in this case the value of α, maximizing DPDR, is around 5%. Figure 4.4.b shows DPDR vs. α trend: we can see how, for this scenario, the advantages of making α=5% is even clearer.

On the basis of these results, the protocol performance evaluation, shown in the following, is made setting the α parameter to 5%.

4.4.2 Simulation Results Analysis

We start our analysis evaluating the performance indexes as a function of node number with a fixed number of maximum concurrent connections, that is 12.

In Figure 4.5, the DPDR is depicted: we can see how the data packet delivery ratio decreases for higher node numbers. In fact, a greater number

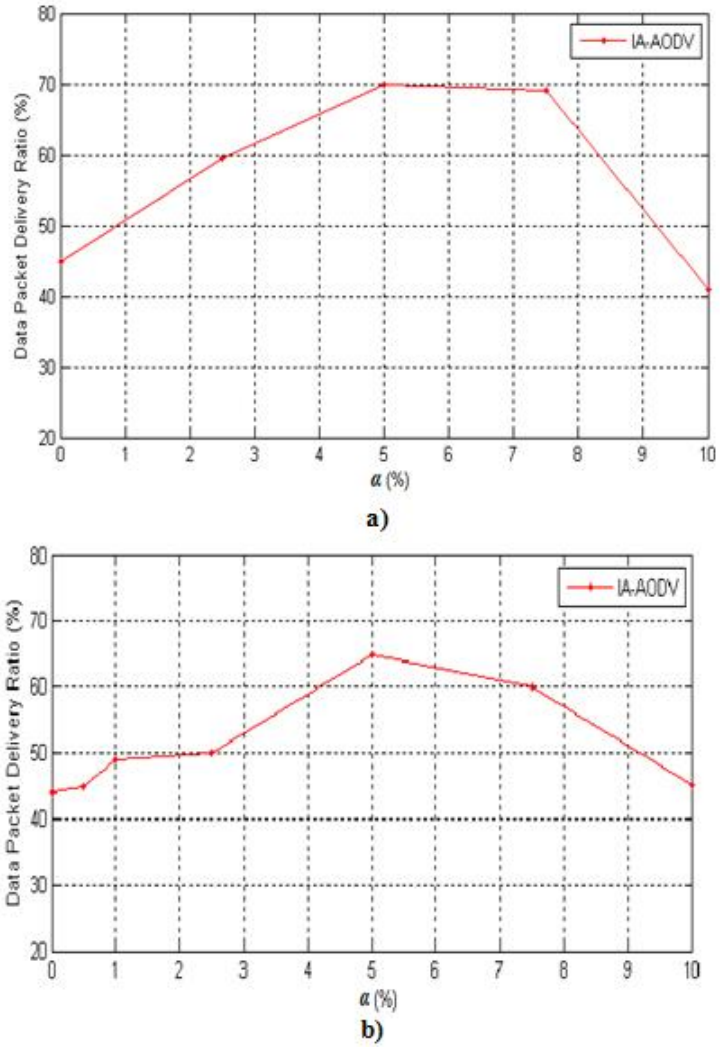

Fig. 4.4. a) PDR vs. α, 4 maximum concurrent connections, 120 nodes. b) PDR vs. α, 8 maximum concurrent connections, 140 nodes.

of nodes in the network means a greater device density in a specific area and so a higher interference. This causes a regular performance degradation. Furthermore, we can note how our metrics (specifically the *LI* metric), in the absence of the refresh mechanism performs comparably with the AODV protocol because, if the interference variation information is not propagated in the network, the nodes continue to transmit on corrupted links and this leads to the loss of many packets. If the refresh mechanism is introduced, the IA-AODV performance improves significantly; in particular, we can see how the *LI* metric performs better than the others: we have an improvement of 10% with respect to the refresh-based *NI* metric, 15% compared with no refresh *NI* and 20% in comparison with AODV protocol and *LI* without refresh in terms of DPDR.

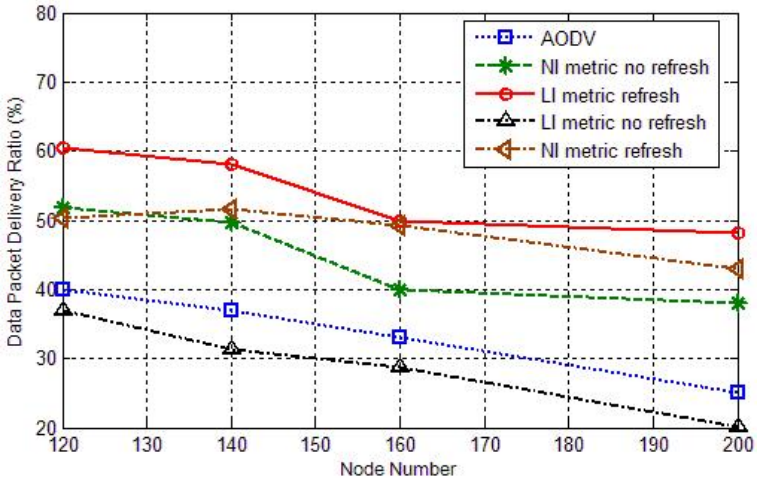

Fig. 4.5. PDR vs. number node in presence of 12 maximum concurrent connections.

The best performance of the *LI* metric with refresh is even more evident from the analysis of AED in Figure 4.6. With the increase in the network node number, the average delay for the *NI* metric (both with and without the refresh mechanism), the no refresh *LI* metric and AODV protocols increases significantly, reaching values which are very high in relation to the proposed protocol. The increase in delay is very influenced by the route selection because the path at minimum interference reduces the number of lost packet retransmissions owing to interference and therefore it leads to a lower processing time for each node belonging to the same route.

This behavior of the DPDR and AED is confirmed by the analysis of NRO shown in Figure 4.7. In fact, the increase in the interference, due to a greater number of nodes, leads to an increase in the NRO. However, in this case, the two protocols perform comparably: IA-AODV (independently of the refresh

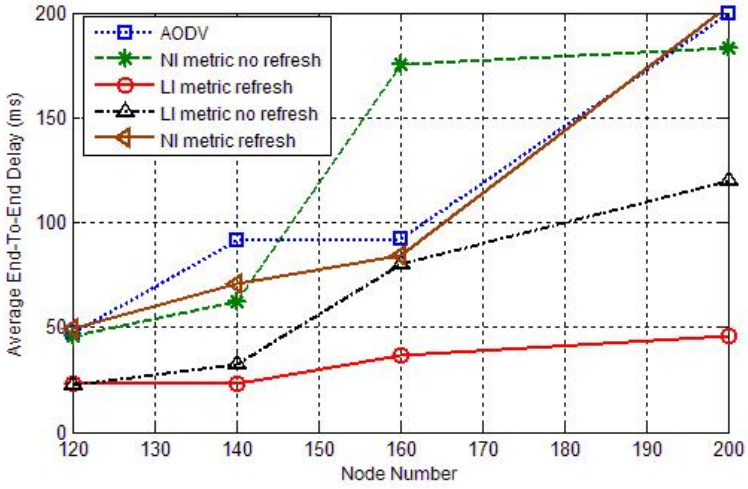

Fig. 4.6. AED vs. number node in presence of 12 maximum concurrent connections

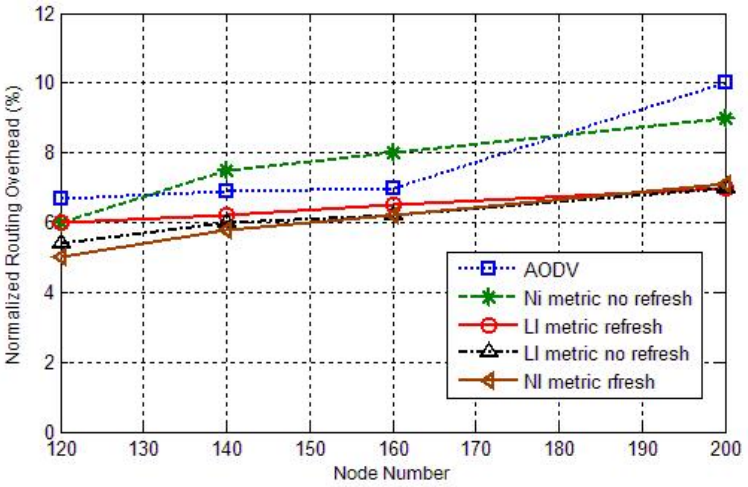

Fig. 4.7. NRO vs. number node in presence of 12 maximum concurrent connections.

mechanism) shows an overhead of 6%-8% on the basis of adopted metric, whereas the AODV protocol shows an overhead assuming values around 8% with a peak of 10% in the presence of 200 nodes (in fact the links are less stable due to interference and so they break easily).

We now evaluate the performance of the proposed protocol varying the maximum number of concurrent connections fixing the total number of nodes in the network. We consider a scenario in which 120 nodes move on a grid with a maximum speed of 4 m/s.

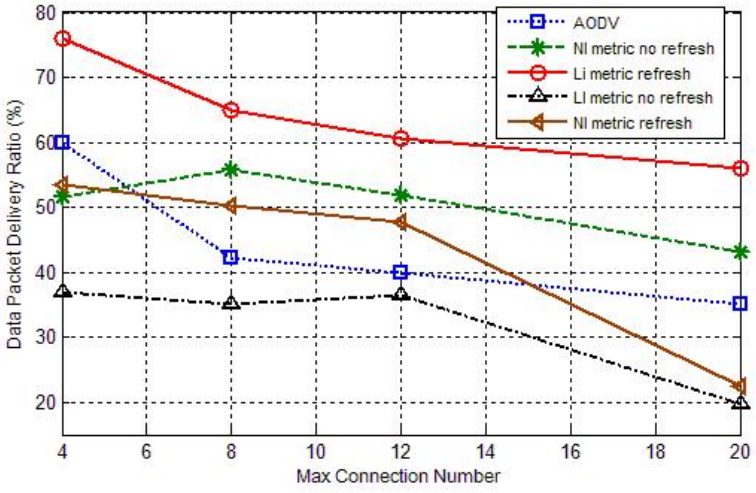

Fig. 4.8. PDR vs. concurrent connection maximum number with 120 nodes.

Observing the PDR curves depicted in Figure 4.8, we immediately note how the *LI* metric with refresh mechanism shows a constant improvement with respect to AODV regardless of the number of connections. This improvement for the *LI* metric with refresh, although decreasing, remains however around 10%. On the other hand, the *NI* metric shows, in this case, a contrary trend: the refresh mechanism leads to a decline in performance because the increase in the connections number causes the increase in the total interference perceived by the nodes. Therefore, the greater amount of interference makes the links more unstable due to the increase in interference information update requests (considering the total interference perceived by a node, *NI* metric, a variation in a single link could cause an updating of all links involving the node).

Figure 4.9 shows the curves relative to AED. We can see how, for the *LI* metric with refresh, the end to end delay is little influenced by the number of concurrent connections, at least in the presence of 120 nodes. These considerations can be partially made also for AODV and *LI* without refresh, while they cannot be made for the *NI* metric (independently of the refresh mechanism) because it shows an exponential increase in the delays.

In Figure 4.10, the trend of NRO vs. maximum number of concurrent connections is shown for all considered protocols. In this case, our protocol costs slightly in terms of NRO: IA-AODV shows a NRO greater than 1-2 percentage points compared to AODV which increase with an increasing number of connections. We have this trend because the presence of a lower node number (that is 120) leads to a less global interference, meaning also less link breakage and so lesser exchange of control messages for AODV. However, our protocol shows a NRO always less than 8%.

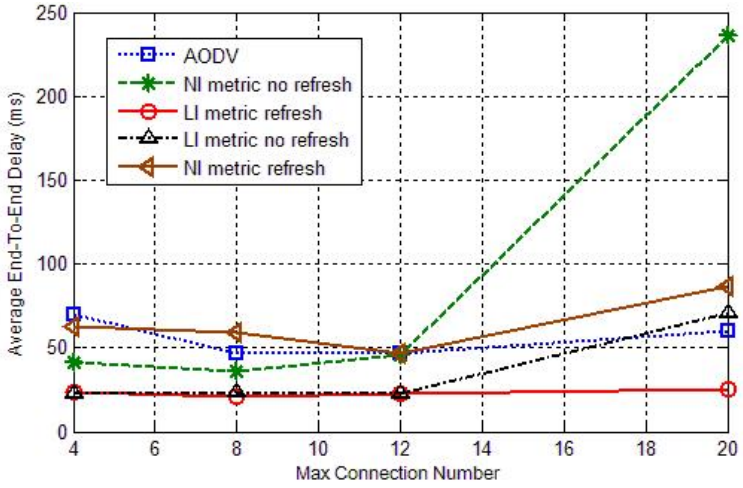

Fig. 4.9. AED vs. concurrent connection maximum number with 120 nodes.

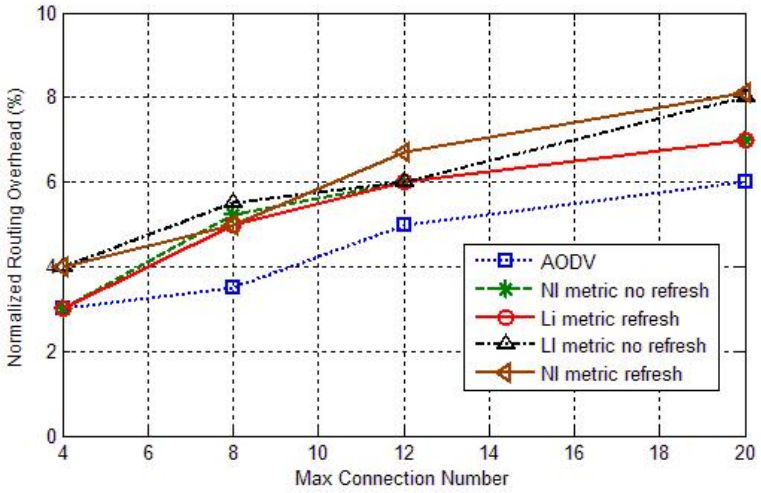

Fig. 4.10. NRO vs. concurrent connection maximum number with 120 nodes.

4.5 Conclusions on Chapter 4

Generally, the classic ad-hoc network routing protocols employ metrics as minimum hop counting or geometric approaches. These is useful in those architectures that are not affected by neighbor interference, but they are not valid in the the UWB ad-hoc networks, in which the mutual interference between nodes can cause serious problems also to routing operations. For this purpose, in this PhD Thesis , a new routing protocol for UWB network, IA-AODV,

based on the concept of interference, has been proposed. In particular, two metrics were proposed: the first one based on the global interference perceived by nodes, called the *NI* metric, and the other based on the interference affecting the link involved in the transmission, called the *LI* metric. Moreover, a refresh mechanism was also introduced in order to quickly propagate the interference variation information in the network. Our protocol is compared with the AODV protocol in terms of DPDR, AED and NRO: for this purpose a ns-2 simulator has been designed. Simulation results show as IA-AODV performs better than others protocol both in terms of DPDR and AED: e.g. for the DPDR, we obtain an average improvement of 15% with respect to AODV especially for the *LI* metric. Generally, also NRO trend of IA-AODV is comparable (or better) to other protocols. Furthermore, we note that in presence of less dense scenarios (and so with a less global interference), IA-AODV has an overhead slightly higher than AODV protocol: however this gap is around 1-2 % and so it is negligible with respect the improvement obtained in terms of DPDR and AED. Furthermore, we note that in the absence of the refresh mechanism our protocol performs comparably with AODV protocol because, if the interference variation information is not propagated in the network, the nodes continue to transmit on corrupted links and this leads to the loss of many packets.

Conclusions

In this Phd Thesis, we discussed some aspects of physical and network layers of UWB sytems. These systems are defined by FCC as any communication system occupying a fractional bandwidth larger than 20% of center frequency or an absolute bandwidth larger than 500 MHz. This last characteristic made the physical phenomena involving UWB communications different from the phenomena affecting the classic narrowband system, so our goal was to investigate UWB physical layer (from the performance analysis to channel modeling) and analyzed how they can influenced also the higher layer of ISO/OSI protocol stack.

In the first Chapter, an overview on UWB system is given. In particular, we described the UWB history from the origin of this technology to nowadays when the increase of commercial interest leads to the standardization phase. Moreover, we give a a mathematical description of the most important baseband impulses typically employed in the UWB transmission. Finally, we described the three high rate alternative physical layer standards: in particular, the main characteristics of DS-UWB, MB-OFDM and TH-PPM systems are given.

In the second Chapter, we analyzed the performance of the DS-UWB physical layer in terms of BER and FER. Our analysys show how the performance degrades for increasing distance (1-15m) even if 28Mbps and 55Mbps rates (and in general the lower rates) are slightly influenced by transmitter-receiver distance, especially for the CM1 scenario with low noise power level. On the other hand, higher data rates (mostly rate $\geq 220 Mbps$) are more sensitive to the transmitter-receiver distance and they can be supported for a shorter distance (in particular this distance decreases for the CM2 scenario and with very high noise power level). In this Chapter we also provided BER analytic formulas (thanks to polynomial regression analysis) for each scenario expressing it as a function of the data rate, noise PSD and distance between transmitter and receiver. Moreover, we provided an analysis on the performance of an ideal MMSE receiver: this treatment allows us to obtained a closed formula for the BER. Finally, we introduced the user mobility in the UWB network

giving in this way BER average limits vs. user speed for the most common user applications (that is voice, data, audio and video applications) in order to provide valid operative range useful to design UWB network taking into account the mobility effects on the applications performance.

The third Chapter treated of a high level wireless channel model based on the concept of degradation level DTMC modelling, useful in every simulation requiring work at the packet level. For this purpose, packet error trace analysis is used to model multi-state channel models. The models obtained are therefore tested by generating artificial traces and comparing them with the trace obtained by experimental simulation and with the artificial trace obtained by the classic G-E Markov chain model, the MTA model and the 3^{rd} order Markov model. Performance evaluation showed that this model better, applied to UWB case, fits the experimental trace than the MTA model, the G-E model and the 3^{rd} order Markov model.

Finally, in the last Chapter, a new routing protocol for UWB network (called IA-AODV) based on the concept of interference, was proposed. In particular, two metrics were proposed: the first one based on the global interference perceived by nodes, called *NI* metric, and the other based on the interference affecting the link involved in the transmission, called the *LI* metric. In addition, a refresh mechanism was also introduced in order to quickly propagate the interference variation information in the network. Our protocol is compared with the AODV protocol in terms of DPDR, AED and NRO: simulation results show as IA-AODV performs better than others protocol both in terms of DPDR and AED especially for the *LI* metric. Generally, also NRO trend of IA-AODV is comparable (or better) to others protocols. Furthermore, we note that in presence of less dense scenarios (and so with a lesser global interference), IA-AODV has an overhead slightly higher than AODV protocol but it is negligible respect the improvement obtained in terms of DPDR and AED. Furthermore, we note that in absence of refresh mechanism our protocol shows performance comparable with AODV protocol because, if the interference variation information are not propagated in the network, the nodes continue to transmit on corrupted links and this leads to lose many packets.

References

1. William A. Kissick, Robert J. Matheson, "UWB technology and regulatory issues", Institute for Telecommunication Sciences, National Telecommunications and Information Administration, U.S. Department of Commerce.
2. Terence W. Barrett, "History of Ultra WideBand Radar and Communication: Pioneers and Innovators", Progress in electromagnetics Symposium 2000, Cambridge, MA, July, 2000.
3. Robert J. Fontana, "A Brief History of UWB Communications", available at www.multispectral.com.
4. Information available at http://www.ieee802.org/15/pub/TG3a.html .
5. Information available at http://www.ieee802.org/15/pub/TG4a.html .
6. Information available at http://www.wimedia.org/ .
7. Standard ECMA-368, "High Rate Ultra Wideband PHY and MAC", Standard 1st Edition, December 2005.
8. Information available at http://www.uwbforum.org/ .
9. Reed R. Fisher et al., "DS-UWB physical layer submission to 802.15 taskgroup 3a", IEEE P802.15-04/0137r4, January 2005.
10. IEEE Std 802.15.4a-2007 (Amendment to IEEE Std 802.15.4-2006), "Part 15.4: Wireless Medium Access Control (MAC) and Physical Layer (PHY) Specifications for Low-Rate Wireless Personal Area Networks (WPANs). Amendment 1: Add Alternate PHYs", January 2007.
11. A. F. Molisch, "Ultrawideband Propagation Channels-Theory, Measurement, and Modeling", IEEE Transaction on Vehicular Technology, VOL. 54, NO. 5, September 2005.
12. Walter Hirt, Domenico Porcino, "Pervasive Ultra-wideband Low Spectral Energy Radio System (PULSERS)", Contribution to 7th WWRF Meeting, Eindhoven, Netherlands, December 3-4, 2002.
13. "FCC notice of proposed rule making, revision of part 15 of the commission's rules regarding ultra-wideband transmission system", Federal Communications Commission, Washington, DC., ET-Docket 98-153.

14. Dajana Cassioli, "Standardizzazione e Regolamentazione di Dispositivi UWB", RadioLabs' Internal Report.
15. Aki Silvennoinen, "Unlicensed reuse of licensed spectrum: case UWB", Communications Laboratory, Helsinki University of Technology.
16. I.Kovacs, G. Pedersen, P. Eggers, and K. Olesen, "Ultra wideband radio propagation in body area network scenarios" in Proc. IEEE ISSSTA 04, 2004.
17. S. SGezici, Zhi Tian, G.B. Giannakis, H. Kobayashi, A.F. Molisch, H.V. Poor, Z. Sahinoglu, "Localization via ultra-wideband radios: a look at positioning aspects for future sensor networks", IEEE Signal Processing Magazine, VOL. 22, Issue 4 pp. 70-84, July 2005.
18. R. J. Fontana, "Recent system applications of short-pulse ultra-wideband (UWB) technology", IEEE Trans. Microwave Theory Techn., pp. 2087-2104, 2004.
19. Weihua Zhuang, Xuemin (Sherman) Shen, Qi Bi, "Ultra-wideband wireless communications", Wireless Communications and Mobile Computing, cap.3 pp. 663-685.
20. Burlacu Mihai, "Ultra Wide Band Technologies", Telecommunications Software and Multimedia Laboratory, Helsinki University.
21. Technical Paper, "UWB and Mesh Networks", White Paper, Artimi Ltd., August 2003.
22. Mikko Leimio, Kari Nokkala, "IEEE 802.15.3a Ultra Wideband techniques (UWB)", TUT:83180 Wireless LAN, 11-08-2005.
23. A. J. Viterbi, "Convolutional Codes and Their Performance in Communication System", IEEE Transaction on Communication Technology, October 1971.
24. J. Hagenauer, "Rate-Compatible Punctured Convolutional Codes (RCPC Codes) and their Applications", IEEE TRANSACTIONS ON COMMUNICATIONS, VOL. 36, NO. 4, April 1988.
25. Pal K. Frenger, Pal Orten, Tony Ottosson, Arne B. Svensson, "zRate-Compatible Convolutional Codes for Multirate DS-CDMA Systems", IEEE TRANSACTIONS ON COMMUNICATIONS, VOL. 47, NO. 6, June 1999.
26. A. Batra et al., "Multi-band OFDM physical layer proposal," Document IEEE P802.15-03/268r3, marzo2004.
27. A. F. Molisch, et al., "Mitsubishi Electric's Time-Hopping Impulse Radio standards proposal", document IEEE P802.15-03112, May 2003.
28. M. Z. Win, R. A. Scholtz, "Ultra-wide bandwidth time-hopping spread-spectrum impulse radio for wireless multiple-access communications", IEEE Trans. Communications, 48, Issue: 4 , pp. 679 -689, April 2000.
29. Javier Ramos, Michael D. Zoltowski, Hui Liu, "A Low-Complexity Space-Time RAKE Receiver for DS-CDMA Communications", IEEE SIGNAL PROCESSING LETTERS, VOL. 4, NO. 9, settembre 1997.
30. J. Foerster, "Channel modeling sub-committee report final", IEEE P802.15-02/490rl, Feb. 2003.

31. Oh-Soon Shin, Saeed S. Ghassemzadeh, Larry J. Greenstain and Vahid Tarokh, "Performance Evaluation of MB-OFDM and DS-UWB System for Wireless Personal Area Networks", IEEE International Conference on Ultra-Wideband, pp. 214-219, September 2005.
32. S. Ghassemzadeh, R. Jana, C. Rice, W. Turin, and V. Tarokh, "Measurement and modeling of an ultra-wide bandwidth indoor channel," IEEETransaction on Commun., pp. 1786-1796, 2004.
33. A. Saleh and R. Valenzuela, "A statistical model for indoor multipath propagation", IEEE J. Select. Areas Commun., vol. 5, pp. 128-137, Feb. 1987.
34. H. Sugahara, Y.Watanabe, T. Ono, K. Okanoue, and S. Yarnazaki, "Development and experimental evaluations of "rs-2000" - a propagation simulator for uwb systems," in Proc. IEEE UWBST 04, pp. 76-80, 2004.
35. B. Uguen, E. Plouhinec, Y. Lostanlen, and G. Chassay, "A deterministic ultra wideband channel modeling," in IEEE Conference on Ultra Wideband Systems and Technologies Digest of Technical Papers, pp. 1-5, 2002.
36. A. M. Attiya and A. Safaai-Jazi, "Simlation of ultra-wideband indoor propagation," Microwvae and optical technology letters, pp. 103-107, 2004.
37. G. A. Schiavone, P. Vahid, R. Palaniappan, J. Trace, and T. Dere, "Analysis of ultra-wide band signal propagation in an indoor environment," Microwave and Optical Technology Letters, vol. 36, pp. 13-15, 2003.
38. A. Domazetovic, L. J. Greenstein, N. B. Mandayam, and I. Seskar, "A new modeling approach for wireless channels with predictable path geometries," in Proc. VTC 2003 fall, pp. 454-458, 2003.
39. J. Kunisch and J. Pamp, "Measurement results and modeling aspects for the UWB radio channel," in IEEE Conference on Ultra Wideband Systems and Technologies Digest of Technical Papers, pp. 19-23, 2002.
40. Wong Tat Tung, Jiangzhou Wang, "MMSE Receiver for Multicarrier CDMA Overlay in Ultra-Wide-Band Communications", IEEE TRANSACTIONS ON VEHICULAR TECHNOLOGY, VOL. 54, NO. 2, marzo 2005.
41. Qinghua Li, Member, IEEE, and Leslie A. Rusch, Senior Member, IEEE, "Multiuser Detection for DS-CDMA UWB in the Home Environment", IEEE Journal on Selected Areas in Communications, vol. 20, NO. 9, December 2002.
42. A. Parihar, L. Lampe, R. Schober and C. Leung, "Analysis of Equalization for DS-UWB System", IEEE International Conference on Ultra-Wideband, pp. 170-175, September 2005.
43. Ramin Khalili, Kav Salamatian, "Evaluation of Packet Error Rate in Wireless Networks", MSWIM - Symposium on Modeling, Analysis and Simulation of Wireless and Mobile Systems,Venice, Italy - October, 2004.
44. C. Montgomery, "Applied Statistics and Probability for Engineers", Third Edition, Wiley, 2003.
45. Tai Suk Kim, Dan Keun Sung and Masakazu Sengoku, "Mobility Modeling and Traffic Analysis in Three-Dimensional Indoor Environments", IEEE Transaction on Vehicular Technology, VOL. 47, NO. 2, May 1998.

46. Tai Suk Kim, Jae Kyun Kwon and Dan Keun Sung,, " Mobility Modeling and Traffic Analysis in Three-Dimensional High-Rise Building Environments", IEEE Transaction on Vehicular Technology, VOL. 49, NO. 5, September 2000.

47. S. Bhattacharya, G. Mishra, S. Kar and H. M. Gupta, "Mobility Modeling and Traffic Analysis in an Indoor Environment using Handoff Traffic with General distribution", M2USIC TS08-6, 2005.

48. S. M. Ross, "Stochastic Processes", John Wiley and Sons, 1996.

49. H. S. Wang and N. Moayeri, "Finite-State Markov Channel - A Useful Model for Radio Communication Channels", IEEE Transaction on Vehicular Technology, vol. 44, N I, February 1995.

50. A. Konrad, B. Y. Zhao, A. D. Joseph and R. Ludwig, "A Markov-Based Channel Model Algorithm for Wireless Networks", Wireless Networks, vol. 9 , issue 3 , pp. 189 - 199, May 2003.

51. P. Ji, B. Liu, D. Towsley and J. Kurose, "Modeling Frame-level Errors in GSM Wireless channels" Perfomance Evaluation, vol. 55, N 1-2, January 2004.

52. G. Boggia, D. Buccarella, P. Camarda, Dapos and A. Alconzo, "A simple ON/OFF logarithmic model for frame-level errors in wireless channels applied to GSM", IEEE 60th Vehicular Technology Conference (VTC2004-Fall), vol. 6, pp. 4491 - 4495, Los Angeles, CA, USA, 26-29 Sept. 2004.

53. C. Jiao, L. Schwiebert and B. Xu, "On modeling the packet error statitics in bursty channels," 27th Annual IEEE Conference on Local Computer Networks (LCN 2002), Tampa, Florida, November 2002.

54. A. Willing, "A new class of packet and bit-level models for wireless channels," IEEE PIMRC 2002, Lisbon, Portugal, September 2002.

55. S. A. Khayam and H. Radha, "Markov-based Modeling of Wireless Local Area Networks", 6th ACM international workshop on Modeling analysis and simulation of wireless and mobile systems, pp. 100 - 107, San Diego, CA, USA, 19 Sept. 2003.

56. M. Yajnik, J. Kurose and D. Towsley, "Packet loss correlation in the MBone multicast network: Experimental measurements and Markov chain models", UMASS COMPSCI Technical Report 95-115, 1996.

57. M.-G. Di Benedetto and G. Giancola, "Understanding Ultra Wide Band Radio Fundamentals," Prentice Hall Pearson Education Inc, New Jersey, 2004.

58. J.Y. Le Boudec, R. Merz, B. Radunovic and J. Widmer, "A MAC protocol for UWB Very Low Power Mobile Ad-hoc Networks based on Dynamic Channel Coding with Interference Mitigation", EPFL Technical Report ID: IC/2004/02, 01-26-2004.

59. J. Y. Le Boudec, R. Merz, B. Radunovic, and J. Widmer. "DCC-MAC: A decentralized mac protocol for 802.15.4a-like uwb mobile ad-hoc networks based on dynamic channel coding". In Proceedings of Broadnets, San Jose, October 2004.

60. B. Hu and N. Beaulieu. Accurate evaluation of multiple-access performance in th-ppm and th-bpsk uwb systems. IEEE Transactions on Communications, 52(10):1758-1766, October 2004.

61. C. E. Perkins, E. M. Belding-Royer, and S. Das. "Ad Hoc On Demand Distance Vector (AODV) Routing." IETF RFC 3561.

62. F. De Rango, M.Gerla, K.Biao Zhou, S.Marano, "GeO-LANMAR Routing Protocol: Asymptotic Analysis in Large and Dense Ad Hoc Networks," 2nd Int. Conf. On Broadband Networks (Broadnet 2005), 3-7 Oct., Boston, Massachusetts, USA, 2005.

63. I. Stojmenovic, Position based routing in ad hoc networks, IEEE Communications Magazine, Vol. 40, No. 7, July 2002, 128-134.

64. B.Karp, H.T.Kung, "GPSR: Greedy Perimeter Stateless Routing for Wireless Networks," in ACM/IEEE Proc. of of Int. Conf. on Mobile Computing and Networking (MobiCom'00), Boston, Massachusetts, United States, pp.243-254, 2000.

65. S. Gezici, Z. Tian, G. B. Giannakis, H. Kobayashi, A. F. Molisch, H. V. Poor and Z. Sahinoglu, "Localization via UWB Radios," IEEE Signal Processing Magazine, vol. 22, no. 4, pp. 70-84, July 2005.

66. J-Y. Lee and R. A. Scholtz, "Ranging in a dense multipath environment using an UWB radio link," IEEE Transactions on Selected Areas in Communications, vol. 20, no. 9, pp. 1677-1683, Dec. 2002.

67. W. C. Chung and D. S. Ha, "An accurate ultra wideband (UWB) ranging for precision asset location," Proc. IEEE Conference on Ultra Wideband Systems and Technologies (UWBST'03), pp. 389-393, Reston, VA, Nov. 2003.

68. W. Horie and Y. Sanada, "Novel Routing Schemes Based on Location Information for UWB Ad-Hoc Networks," Wiley Periodicals, Electronic and Comm. in Japan, part 3, pp. 22-30, vol.88. no.2, 2005.

69. L. De Nardis, P. Baldi and M.-G. Di Benedetto, "UWB Ad-Hoc Networks," Proc. of IEEE Conference on Ultra Wideband Systems and Technologies, pp.219-224, 2002.

70. D. Johnson, Y. Hu, D. Maltz, "The Dynamic Source Routing Protocol (DSR) for Mobile Ad Hoc Networks for IPv4", Internet experimental RFC 4728, February 2007.

71. E. M. Royer, C.-K. Toh, "A review of current routing protocols for ad hoc mobile wireless networks", IEEE Personal Communications, no. 2, April 1999 pp. 46-55.

72. P. Johansson, T. Larsson, N. Hedman, B. Mielczarek, and M. Degermark, "Routing protocols for mobile ad-hoc networks - a comparative performance analysis", Proc. ACM/IEEE Mobicom, '99.

73. L. Mal, Q. Zhang, F. An, and X. Cheng, "DIAR: A Dynamic Interference Aware Routing Protocol for IEEE 802.11-based Mobile Ad Hoc Networks" in MSN 2005, pp.508-517.

74. L. Ma, Q. Zhang, Y. Xiong, and W. Zhu, "Interference aware metric for dense multi-hop wireless networks" in IEEE International Conference on Communications (ICC'05), Vol.2, 16-20 May 2005 pp.1261 - 1265.

75. H.-Y. Wei, S. Ganguly, R. Izmailov, Z. J. Haas, "Interference-Aware IEEE 802.16 WiMax Mesh Networks". In Proceedings of 61st IEEE Vehicular Tech-

nology Conference (VTC 2005 Spring), Stockholm, Sweden, May 29-June 1, 2005.

76. B. Radunovic and J. Y. Le Boudec, "Optimal power control, scheduling and routing in UWB networks". IEEE Journal on Selected Areas in Communications, 22(7):1252-1270, September 2004.
77. Ruben Merz, Jorg Widmer, J. Y. Le Boudec and B. Radunovic. "A Joint PHY/MAC Architecture for Low-Radiated Power TH-UWB Wireless Ad-Hoc Networks". Wireless Communications and Mobile Computing archive, Vol. 5 , Issue 5, pp. 567 - 580, August 2005.
78. Information available on http://www.isi.edu/nsnam/ns/.
79. R. Merz, J. Widmer, J.-Y. Le Boudec, B. Radunovic, "Ultra-wideband MAC and PHY layer implementation for ns-2", 2004. Available on http://icawww1.epfl.ch/uwb/ .
80. C. Bettstetter and C. Wagner, "The spatial node distribution of the random waypoint mobility model", In Proceedings of German Workshop on Mobile Ad Hoc networks (WMAN), Ulm, Germany, March 2002.

List of Publications

Fiore Veltri graduated in computer engineering at the University of Calabria, Italy, in 2005. Since 2005 he has been with the telecommunications research group of D.E.I.S. in the University of Calabria. Since 2006 he has been a Ph.D student in Electronics and Communications Engineering at the University of Calabria. His research interests include: wireless network physical layer, UWB networks, channel and mobility models.

International Journal

J1. De Rango F., Veltri F., Tropea M., Santamaria A.F., Fazio P., Malfitani A., Marano S., "Interdisciplinary issues for the management of next generation autonomic wireless systems: nature-inspired techniques and organic computing". "International Journal of Mobile Network Design and Innovation", Vol. 2, N.3/4, pp. 141 - 152, 2007.

J2. De Rango F., Tropea M., Veltri F., Marano S., "GS Burst Loss Percentage Analysis over an IntServ Satellite System with a Mixed GS-CLS Traffic". "IETE Journal of Research", Vol. 54, N1, January-April 2008.

J3. F. De Rango, F. Veltri, P. Fazio, S. Marano,"Local and Global Trajectory-Based Routing Protocol for Vehicular Ad Hoc Networks in Freeway and Manhattan Environments,", Journal of Networks S08-113, in publication.

International Conference

C1. De Rango F., Fazio P., Veltri F., Marano S., "Performance Evaluation of the Packet Error Rate of DS-SS Physical layer in UWB Networks". Atti del

convegno "Canadian Conference on Electrical and Computer Engineering (CCECE 2006)", Ottawa, Canada, May 7-10, 2006.

C2. De Rango F., Fazio P., Veltri F., Marano S., "Distance-Dependent BER Evaluation of DS-SS IEEE 802.15.3a Physical Layer under Multiple User Data-Rates and Multi-User Interference". Atti del convegno "13rd International Conference on Telecommunications (ICT 2006)", Madeira (Portugal), May 9-12, 2006.

C3. De Rango F., Fazio P., Veltri F., Marano S., "Time and Distance Dependent UWB Channel Modelling: BER and PER Evaluation for DS-SS Modulation". Atti del convegno "63rd Vehicular Technology Conference (VTC Fall 2006)", Montreal, Canada, Sept. 25-28, 2006.

C4. De Rango F., Fazio P., Veltri F., Marano S., "DS-SS UWB Wireless Personal Area Network: BER and PER Evaluation under a MMSE Receiver". Atti del convegno "9th International Symposium on Performance Evaluation of Computer and Telecommunication Systems (SPECTS 2006)", Calgary, Canada, July 31 - August 2, 2006.

C5. De Rango F., Veltri F., Santamaria A., Tropea M., Fazio P., Marano S., "Software Defined Radio based Multi-Mode Satellite Terminal over DVB-RCS Platform". Atti del convegno "12th Ka and Broadband Communications Conference (KaBand 2006)", Naples, Italy, Sept. 27-29, 2006.

C6. De Rango F., Tropea M., Santamaria A., Veltri F., Fazio P., Marano S., "Multi-Mode DVB-RCS Satellite Terminal with Software Defined Radio". Atti del convegno "IEEE Wireless Communication and Networking Conference (WCNC 2007)", Hong Kong, China, March 11-15, 2007.

C7. De Rango F., Veltri F., Fazio P., Marano S., "BER Regression Analysis of DS-UWB based WPAN". Atti del convegno "64th IEEE Vehicular Technology Conference (VTC Spring 2007)", Dublin, Ireland, Apr. 22-25, 2007.

C8. De Rango F., Veltri F., Fazio P., Santamaria A., Tropea M., Marano S., "FER Regression Analysis of DS-UWB-based WPAN". Atti del convegno "Wireless Telecommunication Symposium (WTS 2007)", Pomona, CA, USA, Apr. 27-29, 2007.

C9. De Rango F., Santamaria A., Veltri F., Tropea M., Fazio P., Marano S., "Multi-Satellite DVB-RCS System with RCST based on Software Defined Radio". Atti del convegno "65th IEEE Vehicular Technology Conference (VTC Fall 2007)", Baltimore, USA, Oct. 22-25, 2007.

C10. De Rango F., Veltri F., Gentile A. F., Marano S., "Degradation Level based DTMC Channel Model for DVB-RCS Satellite System". Atti del convegno "13th Ka and Broadband Communication Conference (KaBand 2007)", Turin, Italy, Sept. 24-26, 2007.

C11. De Rango F., Veltri F., Fazio P., Marano S., "Markov Chain Channel Modeling based on Degradation Level Concept for Ultra Wideband WPAN". Atti del convegno "10th International Symposium on Performance Evauation Of Computer and Telecommunication Systems (SPECTS 2007)", San Diego, CA, USA, July 16-18, 2007.

C12. De Rango F., Fazio P., Veltri F., Marano S., "Interference Aware Routing Protocols over Ad Hoc UWB Networks". Atti del convegno "4th International Symposium on Wireless Communication Systems (ISWCS 2007)", Trondheim, Norway, Oct. 17-19, 2007.

C13. De Rango F., Veltri F., Santamaria A., Tropea M., Marano S., "Software Defined Radio-based Multi-Mode DVB-RCS Terminals". Atti del convegno "2007 Military Communications Conference (MILCOM 2007)", Orlando, Florida, USA, Oct. 29-31, 2007.

C14. De Rango F., Veltri F., Marano S., "The Impact of Mobility USERS on DS-UWB System Performance". Atti del convegno "21st Canadian Conference on Electrical and Computer Engineering (CCECE 2008)", Niagara Falls, Ontario, Canada, May 4-7, 2008.

C15. De Rango F., Fazio P., Veltri F., Marano S., "Impact of Interference Aware Metrics over UWB based MANET". Atti del convegno "2008 Wireless Telecommunications Symposium (WTS 2008)", Pomona, CA USA, April 24-26, 2008.

C16. De Rango F., Veltri F., Marano S., "Hierarchical Trajectory-Based Routing Protocol for Vehicular Ad Hoc Networks". Atti del convegno "11th International Symposium on Performance Evauation Of Computer and Telecommunication Systems (SPECTS 2008)", Edinburgh, UK, June 16-18, 2008.

C17. Pignieri F., De Rango F., Veltri F., Marano S., "Markovian Approach to Model Underwater Acoustic Channel: Techniques Comparison". Atti del convegno "2008 Military Communications Conference (MILCOM 2008)", San Diego, CA, USA, November 17-19, 2008.

C18. De Rango F., Veltri F., Marano S., "UWB Channel Modeling: a Markovian Formulation based on Degradation Level Concept". Atti del convegno "69th IEEE Vehicular Technology Conference (VTC Spring 2009)", Barcelona, Spain, April 26-29, 2009.

C19. De Rango F., Veltri F., Fazio P., Critelli D., Giacco S., Marano S.,"An Interference Aware Approach for Routing in UWB Networks". Atti del convegno "70th IEEE Vehicular Technology Conference (VTC Fall 2009)", Anchorage, Alaska, USA, Sept. 2009.

C20. De Rango F., Veltri F., Critelli D., Fazio P., Marano S.," Interference-Aware Ad-hoc on Demand Distance Vector (IA-AODV) Protocol ". Atti del convegno "12th International Symposium on Performance Evauation Of Computer and Telecommunication Systems (SPECTS 2009)", 2009.

C21. Floriano De Rango, Amilcare-Francesco Santamaria, Mauro Tropea, Fiore Veltri, Loris Belcastro, Salvatore Marano, "An enhanced two-stages packet scheduler for dvb-s2 satellite system based on adaptive strategies". Atti del convegno "2009 Military Communications Conference, 2009.

DEIS- DIPARTIMENTO DI ELETTRONICA, INFORMATICA E SISTEMISTICA
Novembre 2009

Settore Scientifico Disciplinare: ING-INF/03